HARNESSING COMPLIANCE IN THE DESIGN AND CONTROL OF RUNNING ROBOTS

by

Xin Liu

A dissertation submitted to the Faculty of the University of Delaware in partial fulfillment of the requirements for the degree of Doctor of Philosophy in Mechanical Engineering

Spring 2017

HARNESSING COMPLIANCE IN THE DESIGN AND CONTROL OF RUNNING ROBOTS

by

Xin Liu

Approved: _____
Suresh G. Advani, Ph.D.
Chair of the Department of Mechanical Engineering

Approved: _____
Babatunde A. Ogunnaike, Ph.D.
Dean of the College of Engineering

Approved: _____
Ann L. Ardis, Ph.D.
Senior Vice Provost for Graduate and Professional Education

I certify that I have read this dissertation and that in my opinion it meets the academic and professional standard required by the University as a dissertation for the degree of Doctor of Philosophy.

Signed: _____

Ioannis Poulakakis, Ph.D.
Professor in charge of dissertation

I certify that I have read this dissertation and that in my opinion it meets the academic and professional standard required by the University as a dissertation for the degree of Doctor of Philosophy.

Signed: _____

Herbert G. Tanner, Ph.D.
Member of dissertation committee

I certify that I have read this dissertation and that in my opinion it meets the academic and professional standard required by the University as a dissertation for the degree of Doctor of Philosophy.

Signed: _____

Ryan Zurakowski, Ph.D.
Member of dissertation committee

I certify that I have read this dissertation and that in my opinion it meets the academic and professional standard required by the University as a dissertation for the degree of Doctor of Philosophy.

Signed: _____

Christopher Rasmussen, Ph.D.
Member of dissertation committee

ACKNOWLEDGEMENTS

First of all, I would like to thank my advisor Dr. Ioannis Poulakakis for supporting and guiding me during the doctoral study. I am constantly encouraged by his enthusiasm in the fields of control theory and legged locomotion and enlightened by his superb knowledge in these fields. Although this thesis bears only my name, the idea is shaped and improved through the numerous discussions with him. I would also like to thank my committee members Dr. Herbert Tanner, Dr. Christopher Rasmussen and Dr. Ryan Zurakowski for their instrumental advice. In terms of funding, the research for this dissertation is supported by the NSF grants CMMI-1130372NSF and IIS-135072, as well as ARO contract W911NF-12-1-0117.

This work benefits a lot from the great colleagues that I met during the past several years. I would like to thank Dr. Claudio Semini from IIT for providing the parameters of HyQ. I would like to thank Anthony Rossi, Alexander Revell and Austin Crouse for their help in the design and setup of the robotic leg – the hundreds of hours we spent at Pearson Hall to build SPEAR from scratch would always be a memorable time during my study at UD. I would like to thank Dr. Qu Cao and Dr. Jianxin Sun for lending me their ears when I need to discuss the research. I would also like to thank my lab mates Mohamad Shafiee Motahar, Sushant Veer, Duanyi Wei and Jian Huang. It is a great pleasure to work with you guys in the Robotic Locomotion Lab.

Last, I would like to thank my parents and my sister for their unconditional support and love during this endeavor.

TABLE OF CONTENTS

LIST OF TABLES

LIST OF FIGURES

ABSTRACT

Legged robots have the potential to extend our reach to terrains that challenge the traversal capabilities of traditional wheeled platforms. To realize this potential, diverse legged robot designs have been proposed, and a number of these robots achieved impressive indoor and outdoor terrain mobility. However, combining mobility with energy efficiency is still a challenging task due to the inherently dissipative nature of legged locomotion. Furthermore, legged robots typically operate in regimes where the natural dynamics of the mechanical system imposes strict limitations on the capability of the actuators to regulate its motion. This is especially the case for running, during which the magnitude of the ground reaction force is several times of the body weight due to the prominent dynamic effects of the motion.

Biological systems demonstrate the great potential of utilizing compliant elements in legged locomotion. During running, part of the mechanical energy is recovered by the elastic deformation of muscles and tendons and returned back to the system when it is needed. In addition, by storing muscle work slowly and releasing it rapidly, compliance alleviates the requirement for powerful actuators. Introducing compliance into legged robots, however, is not a straightforward task. Compliance might lead to high frequency oscillations or impede the free motion of the joints. In addition, due to the relatively large stiffness, the behavior of the system is largely governed by the natural dynamics of the spring-mass system. Careful analysis of the natural dynamics is necessary to fully exploit the benefits of compliant elements.

With the objective to close the gap between mobility and efficiency, this thesis explores the applications of both active and passive compliant elements in the design and control of running robots. The thesis begins with reduced-order running models

with massless springy legs before delving into higher-dimensional models that constitute more faithful representation of robotic systems. Although these models do not incorporate energy losses due to impacts or damping effects, they can predict important aspects of running, including ground reaction force profiles, center of mass trajectories, and the change of stance duration with respect to speed. Using time-reversal symmetries of the underlying dynamics of these reduced-order models, this thesis states analytic conclusions on the stability of periodic running gaits, which can be used to facilitate controller design. Next, a detailed model with segmented leg and inelastic impact is adopted to study the periodic bounding of quadrupedal robot HyQ. Mimicking the reduced-order models, the controller introduces active compliance into the robot. Stable periodic bounding gaits emerge as the interaction results between the robot and its environment.

Inspired by the complementary benefits of passive and active compliance in energy efficiency and control authority, respectively, we propose in this thesis a novel actuation concept: the switchable parallel elastic actuator (Sw-PEA). This concept relies on adding compliance in parallel with the actuator to reduce both the energy consumption as well as the torque requirement related to running robots. In addition, a mechanical switch is used to disengage the spring when it is not needed to facilitate control of joint movement. The effectiveness of the concept is demonstrated experimentally by monopedal robot SPEAR which is actuated by a Sw-PEA.

Overall, this thesis explores the application of active and passive compliant elements in the control and design of running robots, using both numerical simulations as well as experimental evaluations. The result of this thesis points out a promising direction on how to use passive compliant elements in combination with actuators for the development of running robots with both good mobility and energy efficiency.

Chapter 1

INTRODUCTION

1.1 Motivation and Objective

Compared with wheeled vehicles, animals that use legs have advantages in mobility. With the ability to use isolated supporting surfaces, animals can reach a much larger portion of the earth than common off-road wheeled vehicles. What is more, animals can step or jump over obstacles much larger than the length of their legs. In contrast, wheeled vehicles are unable to actively jump and the size of the wheel usually determines the size of the obstacle that can be negotiated. A legged robot with mobility capabilities similar to those of legged animals can be helpful in disaster response situations, in performing search and rescue missions, or in everyday life just to deliver a mail package.

Aside from mobility, energy efficiency is another important consideration when it comes to robots—particularly legged robots—that operate outside of the lab. The task of designing energy efficient legged robots is challenging due to the nature of the motion. In more detail, during walking and running, the gravitational potential energy and kinetic energy of the center of mass (COM) as well as the kinetic energy of the limbs fluctuate within a stride. Without mechanisms to store and release energy, the efficiency drops dramatically since the actuators need to inject energy to sustain locomotion. The lack of actuators which can efficiently satisfy the strict limitations imposed by the natural dynamics of the mechanical system further complicates the task. Due to the dynamic nature of the motion—which is prominent in running gaits—the magnitude of the ground reaction force is usually two to three times the body weight. As a result, the leg joints, especially the knee joints, are required to provide

large torques and forces to support the motion. Moreover, the efficiency of a motor drops with the increase of the output torque/force due to the increase of joule heating. These reasons contribute to the challenge of designing legged robots that combine energy efficiency and control authority, and are capable of realizing dynamic locomotion behaviors.

Inspired by the fact that animals and humans use compliant elements–such as tendons and muscle fibers–to store and release energy, springs have been incorporated into robots. By storing part of the energy in a spring and releasing it later, the cyclic motion can be sustained without excessive actuator effort. In addition, the specifications of the actuators in peak power or peak torque/force can be reduced, thereby reducing the size of the actuators and, consequently, the weight of the robot. With a lighter robot, the motors activating the joints need to provide smaller torques. Since motors have high efficiency in transforming electrical energy to mechanical energy when the output torque is small, the efficiency of locomotion is further improved.

The importance of compliance to legged locomotion goes beyond energy efficiency. In fact, it has been suggested by biologists that the energy exchange between strain energy, which is stored in compliant elements, and other forms of energy, such as kinetic energy and gravitational potential energy, is essentially what distinguishes walking from running. As a result, in contrast to the rigid-leg models that are used for walking, reduced-order models with springy legs have been widely used to study running. The fact that *passively-stable periodic running gaits* have been found in these simplified springy models suggests that compliance can also help in stabilizing locomotion; by coordinating the legs and joints, highly dynamic motions such as running, can emerge as a natural interaction between a robot and its environment. Moreover, compliant legs can reduce the interaction forces between the robot's torso and the ground, therefore preventing damage of the robot and its environment.

However, introducing compliance into running robots is not a straightforward task. To store sufficient energy, the springs that are employed are usually very big. Thus the intrinsic passive dynamics of the open-loop robot plant plays an important

role in the dynamic behavior of the closed-loop system. Thus, the effect of compliance must be analyzed carefully and respected during the controller design. In addition, due to the hybrid nature of the running motion, there are different requirements of compliance at different phases of the gait. In more detail, when the foot is on the ground, compliance is beneficial as it stores energy and it improves interaction with the environment; the requirement is different when the leg is in the air, where precise control of the leg touchdown configuration is needed. Furthermore, compliant elements in the joints typically result in underactuation and high frequency oscillations, if not properly analyzed and designed.

These challenges set the stage of this dissertation, which attempts to close the gap between mobility and efficiency by developing new methods for introducing and controlling compliance in running robots. Compliance can be introduced either *actively*, where the actuators are commanded to behave like springs, or *passively*, where physical springs are employed. While active compliance can be adjusted easily, passive compliance is better for energy efficiency. This dissertation investigates both approaches—i.e., active compliance and passive compliance—by analyzing gait stability and proposing controllers for models of different complexities, as well as by developing a novel compliant actuation mechanism suitable for running robots.

1.2 Contributions

The key results of this dissertation is summarized as follows.

1.2.1 Stability Analysis of Template Models for Running

Reduced-order models which feature massless compliant legs can generate periodic running gaits. To seek insight more systematic than what numerical methods can provide, an analytical framework is proposed to study the stability of reduced order models for monopedal hopping and quadrupedal bounding. Using symmetries in the underlying vector fields, analytical conditions for stability are obtained. For

monopedal hopping, a controller is proposed with analytically provable stability properties. The performance of the controller is demonstrated by having the model run over terrains with randomly varying ground-height profiles. For quadrupedal bounding, a condition that is necessary for stability is stated analytically and used to select control parameters for a leg placement control law.

1.2.2 Controller Design for Active Compliance

This thesis proposes control laws that introduce active compliance through a combination of force and motion control to realize stable quadrupedal bounding. The controller mimics the behavior of a bounding template model. By properly coordinating the joints, stable periodic bounding gaits with velocities from 1.6 to 3.5m/s are realized for an elaborate model with segmented legs and non-conservative toe-ground impact. The model corresponds to the morphology of the hydraulically actuated quadruped HyQ. The proposed controller is robust against unexpected ground-height variations and parameter inaccuracy.

1.2.3 Robot Design Using a Switchable Parallel Elastic Actuator

This thesis proposes a novel actuation design approach to introduce passive compliant elements into legged robots, the switchable parallel elastic actuation (Sw-PEA). This actuation paradigm is then incorporated in the design of the monopedal robot SPEAR, the knee joint of which is driven by a Sw-PEA. When the foot is on the ground, a large spring works in parallel with the knee actuator to recycle energy as the leg bends and extends during stance. The spring is switched off when the leg is in the air so that the actuator can control the leg configuration without interfering with the spring. In addition, the design allows for adjustment of leg stiffness. The effectiveness of the design in reducing energy consumption without impairing mobility is demonstrated by both simulations and experiments. SPEAR realizes running in experiments at 0.5m/s with a electric cost of transport of 0.86, as well as leaping with a toe clearance of more than 45% of its leg length.

1.3 Structure of This Thesis

The rest of this thesis is organized as follows. Chapter 2 provides a brief overview of the related work on template models for running and control design approaches for legged systems, as well as robot designs that use compliance. In addition, the mathematical tools that are used in this thesis to study legged locomotion are presented.

Chapter 3 analyzes stability of reduced-order models of running by factoring the Poincaré map and exploiting the symmetries of the underlying vector fields. Monopedal hopping and quadrupedal bounding are mathematically described as hybrid systems with event-based transitions. Both models feature massless springy legs and non-trivial torsos. For the monopedal hopping model, it is shown that every point on the surface that corresponds to zero pitch oscillation can be turned into a periodic-two fixed point, and that all these motions are stable. For the bounding model, a necessary condition for stability is obtained, which is used to facilitate parameter selection for a leg placement controller.

Chapter 4 deals with the bounding controller design for a detailed quadrupedal model. The model features segmented legs with non-trivial leg mass and inertia, and corresponds to the morphology and structure of HyQ, a hydraulically actuated quadruped designed and constructed at the Italian Institute of Technology (IIT). To realize stable bounding, the controller mimics the behavior of a template: it uses (i) torque planning to create an active compliance element at the stance leg, and (ii) motion control to impose virtual holonomic constraints on the swing leg. Stable periodic bounding gaits are obtained and their properties are evaluated.

Chapter 5 proposes and develops the Sw-PEA, a novel actuation architecture suitable for running robots. A spring is inserted in parallel with the actuator to reduce the torque requirement. To satisfy the different needs of compliance for running robots, a discrete coupling element is introduced. As a result, the parallel spring is only recruited during stance to support the robot and store energy; during the swing phase the spring is switched off to allow for unobstructed joint movement. A compact and reliable design is proposed to realize the concept, which is employed to actuate the

monopedal robot SPEAR. Numerical simulations and experiments demonstrate the effectiveness of the design.

Finally, Chapter 6 concludes the thesis and provides directions for future work.

Chapter 2

LITERATURE SURVEY AND BACKGROUND

Compliant elements play an important role in the realization of animal and human running gaits. As stated in Chapter 1, compliance in animal locomotion helps reduce energy consumption related to leg and torso oscillations by capturing part of the energy and releasing it when it is needed [1]. Compliant members also help reduce the actuation requirement of biological systems during explosive motions by modulating the power required by muscles [82]. What is more, compliance is considered to be important in the stability of rapid dynamic motions, where active neural reflexes are too slow to respond on time [22].

This chapter provides an overview of the relevant literature to motivate and support the work presented in this thesis, in which the role of compliance in running robots is explored through locomotion models with increasing complexity as well as through hardware development. Section 2.1 reviews the results on reduced-order compliant models for running, which feature massless springy legs without energy dissipation. These models are used to resolve the complexity associated with the high-dimensional nature of legged locomotion systems, be they biological or engineered. Although "simple", these models possess self-stable periodic solutions corresponding to typical monopedal and quadrupedal running gaits. Yet, the dynamics of these systems are non-integrable, and the majority of the relevant work employs numerical simulation or approximation to study the existence and stability properties of the resulting gaits. This motivates the work in Chapter 3 where an analytic framework is adopted for analytically insightful results.

Section 2.2 reviews the hardware and controller development for dynamically stable robots, especially running robots. Some of the key platforms and controllers are

reviewed. While most of them use intuitive control laws, nonlinear controllers with formal stability analysis demonstrate the potential to realize highly agile, dynamic locomotion with formal guarantees of stability. This motivates the work in Chapter 4 for the development of a quadrupedal bounding controller, which mimics the behavior of the reduced-order models and creates active compliant elements in the joints.

Section 2.3 reviews a number of design approaches for introducing passive compliance into legged robots. To allow safe interaction, as well as recycling energy, compliant elements are introduced into the driving train. Actuation architectures and robots with different configurations of the actuator and the spring are discussed, with the advantages and shortcomings analyzed. This discussion motivates the work in Chapter 5 where a novel way of using compliance is designed and evaluated.

In the last section, the mathematical tools used in later chapters are introduced.

2.1 Reduced-order Models for Running

Reduced-order models—termed "templates"—have been extensively used to resolve the complexity associated with the high-dimensional, hybrid dynamics of human and animal locomotion [22]. By preserving the dominant features of the locomotion behaviors without delving into the fine details, templates are crucial in uncovering fundamental principles of locomotion and in synthesizing practical control laws. Figure 2.1 presents one such template, namely the spring-loaded inverted pendulum (SLIP), which has been used extensively to study running motions in animals and machines [7]. The SLIP has a point mass and a massless springy leg. Albeit simple, this model is able to characterize the energy exchange, ground force profile and other important aspects of monopedal and bipedal running [28]. The insight gained from this simple model has lead to controller design for more complex systems, including Raibert's three-part controller [74]. This model has also been used to guide the development of robotic platforms. Several robots, including MABEL [32] and ATRIAS [36], are deliberately designed such that their mechanical properties resemble the SLIP template.

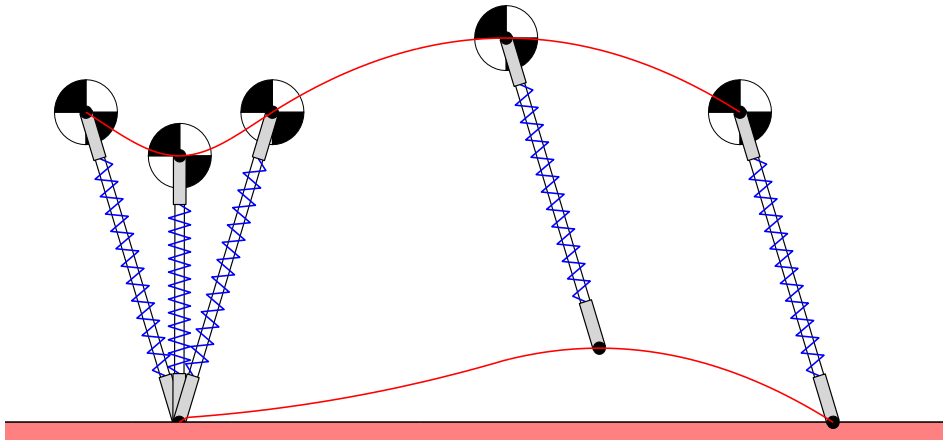

Figure 2.1: Stride-one gait of the SLIP model, composed of one stance and one flight phase.

Along the same lines, models with non-trivial torso inertia have been proposed to capture the pitch dynamics for the case where the hip does not coincide with the COM. For example, the Asymmetric Spring-Loaded Inverted Pendulum (ASLIP) is used in the simulation and controller design for the monopedal robot Thumper [70]. Note that in ASLIP, the hip and COM does not coincide, requiring active torso control. Along the same vein, reduced-order models have been proposed for quadrupedal bounding [71], pronking [12] as well as galloping [24], and have been extensively used to analyze gait stability and evaluate energetic performance.

The majority of the studies on template locomotion models focuses on determining and analyzing periodic motions; see [95], [94], [71] for a few examples using Poincaré return map method [47]. The Poincaré return map takes a state of the hybrid system at an event and maps it to the state at the next occurrence of the event, see Sec. 2.4.1 for a brief overview. This transforms the hybrid system to a discrete system, the fixed points (equilibrium points) of which correspond to the periodic gaits of interest. The stability properties of a gait can thus be examined by analyzing the stability of the discrete system at the corresponding fixed point [102].

However, due to the non-integrable dynamics of the stance phase, no analytic

solutions exist even for a model as simple as the SLIP [88]. As a result, the proposed analyses rely heavily on numerical evaluation, which is computationally intensive [11]. To seek insight more systematic than what numerical approaches can provide, approximate solutions have been proposed by different researchers. In [88], a closed form approximation of the return map for the SLIP has been obtained by iterated application of the mean value theorem. By increasing the iterations, numerical evidence suggests that the maximum and mean approximation error decreases. However, the iteration decreases mathematical tractability and how the approximation can be used in analyzing the existence and stability of periodic gait of the return map is not pursued. In [29], a stability analysis for the SLIP is carried out by neglecting the gravity during stance, proving analytically the existence of stable periodic gaits in SLIP. In [86], an approximation of SLIP is obtained by neglecting gravity during stance to retain angular momentum conservation and then re-introducing the effect of gravity during flight to computing the velocity to enforce conservation of energy. This approximation is used to analyze stability of an adaptive control law. However, a relatively large leg stiffness is usually required to justify the assumption of zero gravity, so that the effect of the elastic force dominates that of the gravitational force in stance. [27] obtains an approximation which retains the effect of gravity using linearization about mid-stance and studies the region of stability of periodic solutions for a SLIP model. However, this approximation is more effective for small leg compressions and sweep angles [29].

On the other hand, symmetry has played a key role in the control design and stability analysis for legged robots [76]. In the field of walking, [42] proposed a hierarchical controller for a compass walker, which uses time-reversal symmetries in a Hamiltonian approximation of the original system's dynamics described by neglecting impact to find symmetric periodic gaits. The gaits are then stabilized by an outer layer which controls the velocity by leg extension or torso inclination. Similarly, [32] analyzes the periodic gaits of a Symmetric Hybrid System (SHS) emerging from the physical system when imposing proper constraints. The resulting symmetric gaits can be stabilized by introducing asymmetries to the system, such as torso inclination. This

method is extended to study the walking of the bipedal robot MARLO in [80]. It can be seen that while symmetric motions can account for the coupling between the body and legs at steady state, asymmetry in the motion can generate stabilizing forces [79], or can be used to accelerate and decelerate the system as in Raibert's three-part controller [74].

Using symmetry properties of the reduced-order models, an analytical framework for studying the stability of periodic running gaits has been introduced in [2]. In that work, a class of symmetry transformations—termed *time-reversal symmetries* [49]—is used to decompose the Poincaré map associated with symmetric hopping motions of the SLIP [87]. The decomposition allows the derivation of closed-form conditions that are necessary for stability. The method was subsequently used in [3] to investigate the stability of a suitably controlled model of the hexapedal robot RHex.

At the core of [2] are point-mass models like the SLIP [2, 87] and its extensions [3]. Such models, however, cannot capture the torso pitch dynamics which is a distinguished feature of bounding gaits [71]. Chapter 3 aims at extending the analytic framework adopted in [2] to models with non-trivial torso pitch dynamics, including the Asymmetric Spring-Loaded Inverted Pendulum (ASLIP) of [70] and the quadrupedal bounding model of [71]. In chapter 3 we propose a symmetry-based control law and a synthesized torso control strategy, to stabilize stride-two periodic gaits of the ASLIP. In addition, we obtain an explicitly expressed necessary condition for stability of bounding gait.

2.2 Dynamically Stable Robots and Their Control

A variety of robots has been developed to realize the locomotion capability exhibited by humans and animals. In the realm of bipedal walkers, the majority of these robots uses the zero moment point (ZMP) as the stability criterion [101]. These robots typically feature legs with multiple joints and flat feet, where each joint is actively driven by a motor [45]. To prevent the robot from tipping over, the controller ensures that the ground projection of the COM is kept within the supporting polygon, i.e., the

convex hull of all the contact points of the foot with the ground. This criterion has been successfully used in humanoid robots, including the bipedal robot ASIMO [85] which is capable of a wide variety of different tasks. However, this criterion places constraints on how far the robot can place its foot ahead of its COM and excludes running gaits which have flight phases.

On the other hand, dynamically stable robots relax the constraints imposed by static stability requirements by allowing the COM to be outside the supporting polygon, as long as the COM is captured by the legs before falling [97]. Raibert and his colleagues developed a series of robots with one, two and four legs in the 1980s, which feature hydraulically or pneumatically actuated joints and air springs [74]. Raibert proposed an intuitive three-part controller to control his robots. The controller regulates hopping height by adjusting the thrust of the prismatic knee joint, forward velocity by adjusting the landing position of the toe, and body attitude by adjusting the hip torque. Stable running gaits have been realized with impressive speed and natural looking motions.

Following Raibert's seminal work, a number of dynamically stable robots have been developed using similar control ideas. Boston dynamics developed quadrupedal robots—BigDog [77] and LS3 [16]—which realized different running gaits with impressive capabilities in terms of negotiating rough terrain. They also developed the cheetah robot, a hydraulically-powered quadruped which can run at a speed of 45.5 km/h with a lateral support mechanism [15]. Along the same lines, the Scout II quadruped demonstrated efficient bounding gaits using only one actuator per leg located at the hip [72]. The work in [56] introduces a different paradigm, employing fuzzy controllers informed by Raibert-style heuristics to control quadrupedal galloping. In connection with this work, the quadruped KOLT has been used to investigate running in [62], and a differential leg thrust controller has been applied to regulate trotting in [19].

Alternative control approaches for dynamic running robots also exist in the literature. Inspired by the natural control of animal locomotion, control laws based on central pattern generators (CPG) for generating rhythmic locomotion behaviors,

have been employed to control legged robots [43]. The quadrupedal robot Tekken realized dynamic walking motions on different terrains using a neural oscillator network, which consists of a CPG and reflexes to alter the active phase based on sensor input [21]. A Cheetah-Cub robot has been developed at École Polytechnique Fédérale de Lausanne (EPFL) which runs 6.9 times its body length per second, or 1.42m/s [96]. It worth mentioning that this robot is open-loop, controlled by a CPG which generates the reference hip and knee joint trajectory without using sensor information. The quadrupedal robot HyQ realized a running trot gait with a velocity of 1.3m/s using a similar CPG framework [89]. A different paradigm, which adopts an optimization-based approach, has been used to realize a running trot on the quadruped StarlETH [25]. The controller employs motion control on the swing legs and torque control on the stance legs. The torques applied at the stance leg joints are obtained by solving a convex optimization problem to reduce the tracking error with respect to the desired virtual force/torque obtained by the requirement to follow a desired COM trajectory [26]. Recently, a running controller has been proposed in [64, 100] that directly plans and controls the horizontal and vertical ground reaction forces to realize a zero net impulse during a periodic cycle. This controller leads to 4m/s running on the MIT Cheetah 2 robot, a 12 degrees of freedom (DOF) electrically actuated quadruped [65].

In contrast to the aforementioned intuitive controllers, established nonlinear control methods [44], suitably extended to accommodate the hybrid dynamics of legged locomotion [102], can be effective in stabilizing highly agile, dynamic locomotion on bipeds with complex morphologies. Successful walking and running gaits have been realized on the 2D (planar) bipedal robot MABEL [98], [99] and on the 3D biped MARLO [78] using such controllers. However, the design of controllers for running quadrupeds, based on a rigorous formulation of the feedback control problem, has not received much attention in the relevant literature. The differences in morphology between the bipedal and quadrupedal robots renders the controllers developed for bipeds inapplicable to quadrupeds [99]. For example, the weight of the torso in a bipedal robot produces a relatively small torque with respect to the hip axis, which is not the

case in quadruped. Indeed, the horizontal torso configuration of quadrupedal robots produces a much larger torque with respect to the hip, and thus a direct application of the methods in [102] would require large torques to actively stabilize the torso. On the other hand, active torso stabilization may not even be necessary for quadrupedal bounding gaits due to the stabilizing effect of the front legs that capture the robot's torso before falling [74]. Chapter 4 in this thesis develops a quadrupedal bounding controller to address this problem. The controller mimics the behavior of compliant bounding templates, and it incorporates active compliant elements in the nonlinear control framework [102].

2.3 Compliance in the Design of Robots

The design of energy efficient legged robots without impairing mobility and control authority is an active research area. In the context of electrically actuated systems, one way to achieve energy efficiency is to use regenerative braking to capture some of the energy when the motor is doing negative work [92]. With this approach, the MIT cheetah realized impressive locomotion efficiency using customized high torque density motors [93] and light legs [4]; see [92] for an overview of the design. Note though that electrical energy, including the part recaptured through specially designed motor driving circuitry, needs to be converted back to mechanical energy [67]. Particularly in legged robots, this conversion occurs at low efficiency because of the large torques involved and the ensuing losses due to Joule heating; in [92], a 24% conversion efficiency is reported with optimally designed motors.

Inspired by compliant structures—such as tendons and muscle fibers—in the legs of animals [1], mechanical springs have been incorporated into legged robot designs to recycle energy [33]. Tendon efficiency in recycling energy can reach up to 90% [68], and steel springs could have an even higher number due to low hysteresis [39, p. 142]. Beyond energy recycling, suitably inserted compliant elements can reduce the peak power and torque requirements of the actuators [30]. This further improves efficiency

since the actuators operate in a low torque region and efficiency in electromagnetic motors increases as the output torque decreases [35].

One way to introduce compliance in a legged robot's structure is the Series Elastic Actuator (SEA), as is shown in Fig. 2.2(a), in which a spring is placed in series with an actuator [73]; see also [33,63] and references therein. Focusing on legged systems, an early implementation of series compliance can be found in Raibert's robots, in which air springs were placed in series with hydraulic actuators [74]. To realize spring-mass walking [98] and running [99], the bipedal robot MABEL has been designed with large leaf springs connected in series with the actuators through a transmission system so that compliance is present in the leg length direction [37, 38]. More recently, ATRIAS used a series-elastic parallelogram mechanism to achieve spring-mass 3D hopping and walking motions [36]. Along a different philosophy, the humanoid COMAN [51] is powered by intrinsically compliant knee and ankle joints while the quadrupedal robot StarlETH comprises 12 SEAs actuating all of its joints [39]. In these systems, besides passive mechanical energy storage [36–38] and torque control capabilities [39,63], SEAs offer protection of the motor and gearbox by filtering out impulsive loads at collisions. This makes SEA an attractive choice for legged robots. On the other hand, the motors in SEAs must be capable of producing forces and torques that are comparable to those developed by the springs [9], which, in the context of dynamic legged robots, translates to large motors and gear reduction ratios. Furthermore, SEAs typically increase the number of degrees of freedom (DOF) of the system, requiring special design and control considerations[1] [41, 63].

Figure 2.2(b) shows an alternative way to introduce compliance, in which the spring is inserted in parallel with the motor so that the spring and the actuator work in an additive fashion [61]. An example of using Parallel Elastic Actuators (PEA)

[1] In fact, the existence of physical compliance in series may limit the range of behaviors that can be realized by the system [89]. Being able to actively modify the stiffness of the passive component as in variable stiffness actuators (VSA), can help mitigate this restriction, although VSAs tend to increase the complexity of the system; see [33] for a review of VSAs.

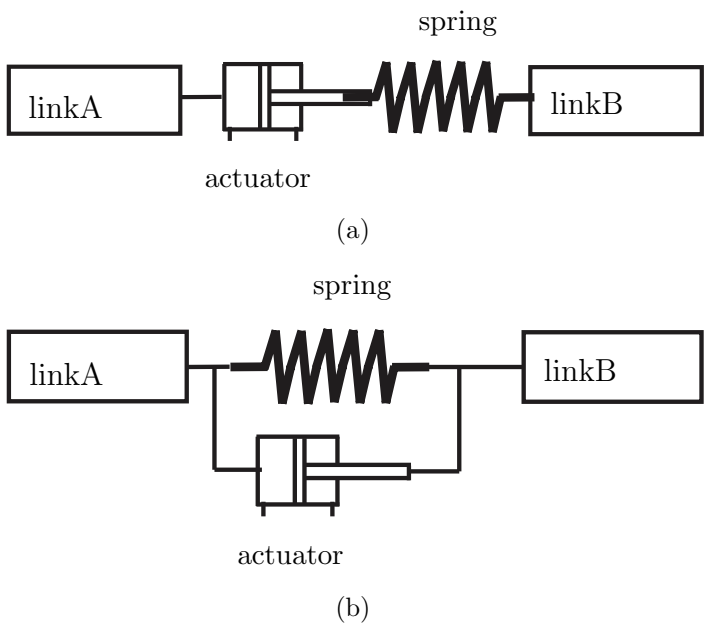

Figure 2.2: (a) Series Elastic Actuator (SEA). (b) Parallel Elastic Actuator (PEA).

can be found in [9], where springs are used to improve energy efficiency and safety of known maneuvers in passive-assist devices for active joints. In the context of legged robots, the biped ERNIE utilizes springs in parallel with its knee actuators to generate walking motions [103]. PEAs may reduce both power and torque requirements, as suggested in simulations of bipedal [18, 30] and quadrupedal [20] running. In general, introducing springs in parallel with the actuators may limit joint dexterity since the actuator needs to work against the spring [34], which would impair the mobility of the robot. Recently, numerical optimization has been employed in [104] to determine the optimal actuation configuration among different combinations of SEAs and PEAs actuating the hip and (prismatic) knee joints of a two-dimensional hopping model. It was found that the optimal actuation configuration in terms of positive electrical work—a metric of energy efficiency—is velocity dependent.

Recently, there has been an increasing number of actuator designs that incorporate discrete coupling elements—such as clutches or brakes—into the SEA paradigm [66]. These coupling elements can increase the output performance of the actuation unit.

For example, in [83], a clutchable SEA is developed, where the clutch is put in parallel with the motor. When the clutch engages, it connects one end of the spring directly to a fixture, allowing the spring to deform. The motor is bypassed and does not need to produce any torque. The design in [83] is used to power an active knee prosthetic device, and the observed energy consumption is an order of magnitude less than previous results. However, the motor is unable to provide additional energy when the clutch is active. A general purpose SEA that employs discrete coupling elements to achieve multimodal operation for versatile applications can be found in [50]. The prototype actuator is 0.67m long and weights 4.5kg, which makes it suitable for relatively large systems.

Discrete coupling elements can also be used to overcome the shortcomings associated with PEAs. Based on analyzing a planar bipedal walking model, the work in [61] advocates the use of a Switchable Parallel Elastic Actuator (Sw-PEA) with position-dependent clutch function so that the spring is engaged when a leg is in stance—that is, when it is mostly needed—but not during flight. A similar observation is made in [20] in the context of modeling high-speed quadrupedal running. The authors of [20] mention, however, that commercially available clutches are generally slow, and their size and weight make them unsuited for light-weight legs, and propose a conceptual design for realizing switchable compliance in the context of the MIT Cheetah's leg design [4].

Beyond the realm of simulation studies, only a few hardware prototypes exist that combine PEAs with switches. One such prototype, which uses a clutch to realize the switch is described in [34]. Experiments in which the actuator is constrained to mimic the torque and motion pattern of the knee extensor muscle of a human hopping task suggest that the energy consumption is reduced by 80% and the peak torque requirement decreases by about 66% compared to the case where no springs are used. A different approach is proposed in [57], which develops a prototype of an actuator that uses a single motor to recruit several parallel elastic elements in sequence with mutilated gears. This arrangement increases the maximum output torque of the

actuator, and in a more recent version [23] it also allows for stiffness adjustments, although the complexity of the current prototypes is higher compared to other actuator designs. Very recently, [67] presented a bi-directional Sw-PEA prototype, which uses a differential with two locking mechanisms to load and unload the spring in a controlled manner, thereby achieving reduction in energy consumption.

Although the aforementioned prototypes indicate that Sw-PEAs offer potential advantages in terms of energy efficiency and motor torque reduction, their use has not been evaluated in the context of dynamic legged robots, an application that would benefit from such capabilities. Only a few results are available in exoskeleton design, which employ a mechanical clutch [17] or electrostatic forces [14] to engage and disengage the parallel spring. To the best of the authors' knowledge, only [46] presents the design of a dynamic bipedal robot, which employs a Sw-PEA at its knee joint; a preliminary energy analysis is also reported in [46].

These observations set the stage of Chapter 5 of this thesis, which aims at evaluating the contribution to energy efficiency and mobility of a Sw-PEA in dynamic running motions. The proposed design of a Sw-PEA actuator takes advantage the leg's geometry to realize a reliable and compact mechanical switch at the foot that engages the energy-storing spring only when it is needed, i.e., during stance. With the switch passively operated by the ground reaction forces (GRF), this design is suitable for light legs while it can also be easily modified for larger and heavier robots.

2.4 Related Mathematical Methods

In this final section, the mathematical concepts and tools used to study the stability of periodic gaits are presented for later usage.

2.4.1 Hybrid Systems and Poincaré Return Maps

The class of models that we will encounter in this thesis can be thought of as a subset of hybrid system models. In more detail, legged robots can be modeled as systems with dynamics evolving in continuous and discrete time. As a result, the state

of such systems includes both continuous x as well as discrete q (mode) components. Starting from an initial condition x_0 with a discrete state q_0, the evolution of continuous state $x \in \mathcal{X}$ is governed by a vector field

$$\dot{x} = f_{q_0}(x) \tag{2.1}$$

while the discrete state q remains constant at q_0. When the continuous state x makes a threshold function $\mathcal{H}_{q_0}(x)$ pass through zero, the discrete state changes to a different value, say, from q_0 to q_1. The threshold function defines a surface $\mathcal{S} := \{x \mid \mathcal{H}_{q_0}(x) = 0\}$ in the state space $\mathcal{X}$. When the state enters the set $\mathcal{S}$, it is referred as an *event*. At that instance, the continuous state is reset by a map $\Delta_{q_0 \to q_1}(x)$. After the event (and reset), the continuous evolution resumes and the whole process is repeated, although the system now could be governed by a different vector field, say, $f_{q_1}(x)$. This process defines a trajectory (or solution) $\phi(x_0, t)$ of the hybrid system for $t \geq 0$.

The study of running gaits is equivalent to studying distinguished periodic solutions of a hybrid system. For example, the robot could be in one of the two discrete states, i.e., the flight or the stance phase, during which the evolution is governed by the corresponding continuous vector field as in (2.1). When the contact condition between the toe and ground changes, the system goes from one phase to the other. The transitions are captured by threshold functions corresponding to the vertical ground reaction force or the distance between the toe and the ground, defining the liftoff and touchdown events, respectively. A nontrivial periodic running gait is a hybrid trajectory of the system which satisfies $\phi(x_0, t) = \phi(x_0, t+T)$ for any $t \geq 0$ with $T > 0$. The periodic gait defines a set $\mathcal{O} := \{x \mid x = \phi(x_0, t), 0 \leq t \leq T\}$.

In legged robots, the notion of stability can be understood in different ways. In contrast to the static stability—satisfied when the projection of the COM is within the supporting polygon—formed by the feet in contact with the ground, in what follows we adopt the notion of stability in the sense of Lyapunov [102]. A periodic solution is stable if for every $\epsilon > 0$, there is an open neighborhood $\mathcal{V}$ around $\mathcal{O}$, such that for every initial state $x_0' \in \mathcal{V}$, there exists a solution $\phi(x_0', t)$ for $t \geq 0$, and the distance

between $x'_t := \phi(x'_0, t)$ and $\mathcal{O}$ is smaller than ϵ for all $t > 0$. The distance between x'_t and $\mathcal{O}$ is defined as $\text{dist}(x'_t, \mathcal{O}) := \inf_{x \in \mathcal{O}} \|x'_t - x\|$ where $\|\cdot\|$ denotes the Euclidean norm; See [102] for more details.

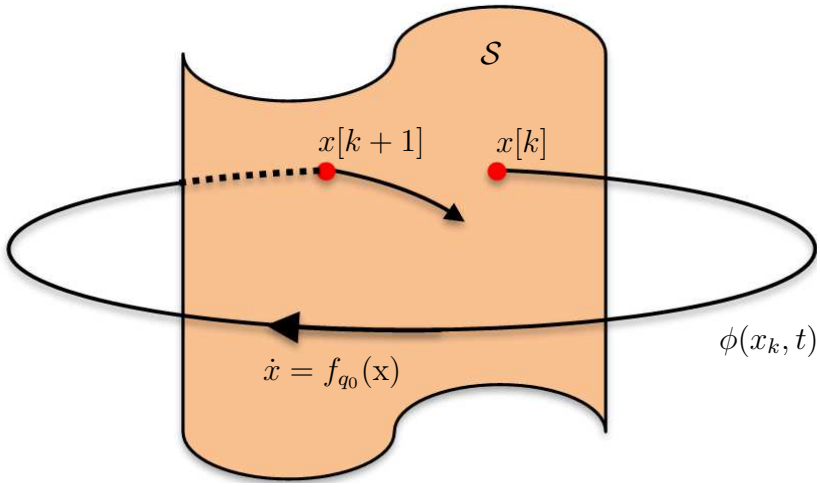

Figure 2.3: The Poincaré return map P maps the initial state $x[k]$ on the Poincaré section $\mathcal{S}$ at step k to the state at next step $x[k+1]$. Notice that the reset map Δ is not shown here for simplicity.

The method of Poincaré is discussed in [102] for hybrid systems and is used to study the stability of periodic gaits. Using the surface $\mathcal{S}$ defined by the threshold function as the Poincaré section, the Poincaré map $P : \mathcal{S} \to \mathcal{S}$ is defined as

$$x[k+1] = P(x[k]) \tag{2.2}$$

where $x[k]$ and $x[k+1]$ are the states of the system at steps k and $k+1$, see Fig. 2.3. In the case of running, $x[k]$ could be the state of the robot at touchdown or liftoff, depending on the choice of the Poincaré section. With this notion, the periodic gait corresponds to a fixed point (or, equilibrium point) of the discrete map P which satisfies

$$P(\bar{x}) - \bar{x} = 0. \tag{2.3}$$

The stability properties of a periodic gait can be captured by the stability of the corresponding fixed point. A fixed point $\bar{x}$ is locally exponentially stable if and only if

the eigenvalues of the Jacobian matrix $J = D_x P(\bar{x})$ of P at the fixed point $\bar{x}$ are all within the unit disc. Notice that local exponentially stable stability implies

$$|\det(D_x P(\bar{x}))| = |\lambda_1 ... \lambda_i ... \lambda_n| < 1, \tag{2.4}$$

i.e, (2.4) is a *necessary* condition for gait stability [2]. However, (2.4) is *not* sufficient. Nevertheless, (2.4) provides important information for selecting control parameters, due to the fact that in certain cases $\det(D_x P(\bar{x}))$ can be computed analytically in a neighborhood of a fixed point under certain conditions, as we will see in Chapter 3.

Theorem 1 ([2, Theorem 4])**.** *Let $\bar{x} \in \mathcal{S}$ be a fixed point of a map $P : \mathcal{S} \to \mathcal{S}$, where $\mathcal{S}$ contains a neighborhood of $\bar{x}$. If P is an involution, i.e., $P \circ P(x) = x$, the determinant of its Jacobian $D_x P$ evaluated at $\bar{x}$ is $|\det(D_x P(\bar{x}))| = 1$.*

The significance of Theorem 1, lies on the fact that it facilitates the computation of the determinant of the linearization of the Poincaré map at a fixed point. It will be applied on a factored Poincaré return map to obtain analytical conditions that are necessary for stability through the use of (2.4).

2.4.2 Low-Dimensional Stability Test Based on Finite-Time Convergence

To facilitate stability analysis, [102] presents a theorem which relates the stability property of the Poincaré return map P to that of a low-dimensional restricted Poincaré map $P_{\mathcal{Z}}$ under certain conditions. Before presenting the theorem, a few definitions are given here. A set $\mathcal{Z} \subset \mathcal{X}$ is *forward invariant* if there exists $t_1 > 0$ such that $\phi(x_0, t) \in \mathcal{Z}$ for initial condition $x_0 \in \mathcal{Z}$ in the time duration $t \in [0, t_1)$. The set $\mathcal{Z}$ is impact invariant if the reset map satisfies $\Delta(\mathcal{S} \cap \mathcal{Z}) \subset \mathcal{Z}$. Finally, $\mathcal{Z}$ is hybrid invariant if it is both forward invariant and impact invariant. The set $\mathcal{Z}$ is locally continuously finite-time attractive if it is forward invariant and there exists an open set $\mathcal{V}$ containing $\mathcal{Z}$ such that the settling time— the time it takes to bring a state from $\mathcal{V}$ to $\mathcal{Z}$—is finite and continuous in $\mathcal{V}$.

With these definitions, a theorem which relates the stability property of the Poincaré return map P to that of a low-dimensional system can be stated. Under the

conditions listed in [102, Theorem 4.5], if $\mathcal{Z}$ is hybrid invariant and locally continuously finite-time attractive, a fixed point of the restricted Poincaré map $P_{\mathcal{Z}}$ is also a fixed point of P. In addition, stable (resp. asymptotically stable) fixed points of $P_{\mathcal{Z}}$ are also stable fixed points of the full-dimensional Poincaré return map P. For a double integrator, controllers which satisfy the requirement of locally continuously finite-time attractive are proposed in [5, 6, 31] which will be used in chapter 3.

2.4.3 Time Reversing Symmetry

The analysis of periodic gait stability, or, equivalently, the stability of a fixed point $\bar{x}$ of Poincaré return map P, can be facilitated if the vector fields that underlies the construction of P satisfy certain symmetry properties. Let f be a vector field defined on a chart $\mathcal{X}$, and consider the dynamic system $\dot{x} = f(x)$. An invertible map $G : \mathcal{X} \to \mathcal{X}$ is a *time reversing symmetry* and the vector field f is called *reversible* if

$$D_x G \cdot f = -f \circ G \ , \tag{2.5}$$

where $D_x G$ denotes the derivative of G in x. Equivalently, in terms of the flow $\phi(x_0, t) := \phi^t$ associated with $\dot{x} = f(x)$,

$$G \circ \phi^t = \phi^{-t} \circ G \ . \tag{2.6}$$

In the Hamiltonian formulation, where the vector field f are derived from a Hamiltonian function $H(q, p)$, the time-reversing symmetry G takes the form:

$$G([q, p]) = [q, -p] \tag{2.7}$$

where q is the configuration, and p is the momentum variables of the system. The reference [49] gives a general review on time reversing symmetries in dynamical systems.

Chapter 3

STABILITY ANALYSIS OF RUNNING TEMPLATES USING FACTORED POINCARÉ RETURN MAP

This chapter examines the stability of reduced-order models—termed "templates"—for monopedal and quadrupedal running gaits. Templates with springy massless legs have been employed extensively in the study of legged locomotion to resolve the complexity associated with the high-dimensional, hybrid nature of the dynamics related to human and animal locomotion [22]. Albeit simple, these models are able to characterize the energy transformations underlying walking and running motions and can capture several aspects of it, such as ground reaction force profile [28]. Due to the non-integrable stance-phase dynamics, however, analysis of such systems is often carried out numerically. Rather than treating the hybrid nonlinear dynamics of locomotion models numerically, this section adopts an analytical framework to study stability for templates with non-trivial torso moment of inertia. Exploiting time-reversal symmetries possessed by the underlying vector fields, the corresponding Poincaré return map can be factored in a way that allows analytically expressed stability conclusions. A controller with analytically provable stability for monopedal hopping is proposed, and a necessary condition for stability of quadrupedal bounding are stated analytically. Numerical experiments demonstrate the performance of the controllers under unexpected ground height variations and other perturbations of the state. Part of this chapter is presented in [53].

This chapter is organized as follows. Section 3.1 introduces the models used for monopedal and quadrupedal running. Section 3.2 analyzes the stability of the monopedal hopping using the time-reversal symmetry possessed by the dynamics, and proposes a controller for running with provable stability. Section 3.3 examines stability

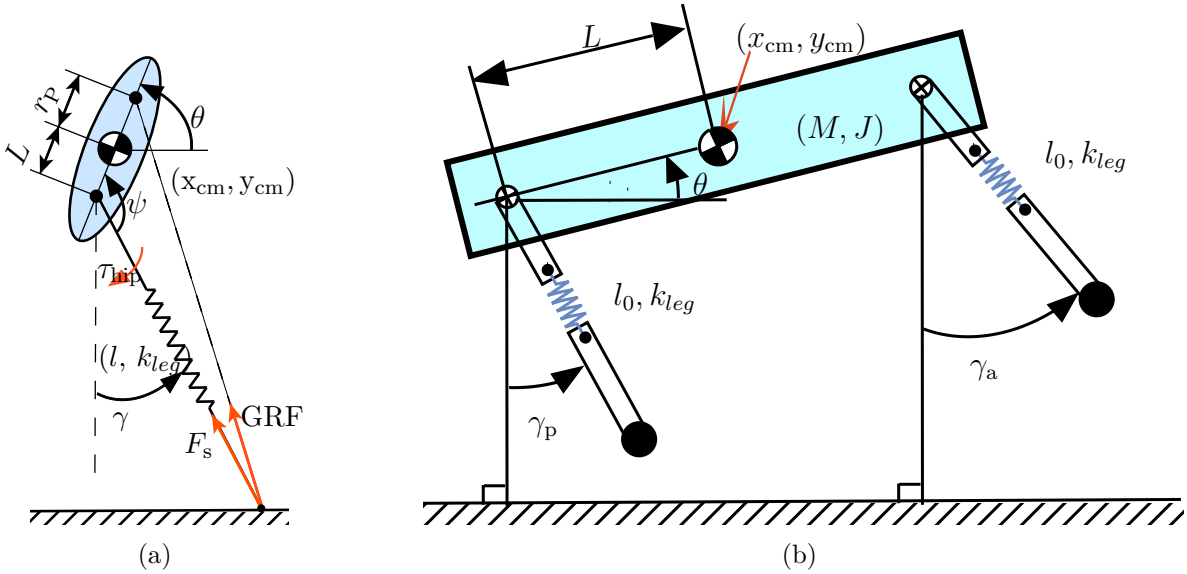

Figure 3.1: (a) The Asymmetric Spring-Loaded Inverted Pendulum (ASLIP), which is used to study the running gaits of monopod and biped. The torso has a non-trivial moment of inertia. (b) The model which is used to study quadrupedal bounding. Both models are assumed to have ideal massless springy legs.

of quadrupedal bounding using a similar approach, and a necessary condition is obtained. Section 3.4 verifies the stability analysis and controller design using numerical simulations. Section 3.5 concludes the chapter.

3.1 Modeling Running Gaits

In this section, the two models that are used to study the monopedal and quadrupedal running gaits are mathematically described for later analysis. Both models feature massless legs, modeled as ideal linear springs without damping, and torsos with non-trivial moment of inertia. Running is modeled as a hybrid system with continuous-time dynamics governing the stance and flight phases, and event-based transitions governing the transitions between the two.

3.1.1 Monopedal Running: The Asymmetric Spring Loaded Inverted Pendulum

Figure 3.1(a) presents the Asymmetric Spring-Loaded Inverted Pendulum (ASLIP) model for monopedal running. To capture nontrivial torso pitch dynamics, the torso's center of mass (COM) is assumed to be above the hip at a distance $L > 0$. A control input $u := \tau_{\text{hip}}$ is introduced at the hip joint to control the torso. The numerical values of the geometric and inertia parameters are given in Table 3.1, which are adapted from [58] and [59]; the specific values of these parameters are only used in the simulation section 3.4 to verify the analysis.

Table 3.1: Mechanical Parameters of ASLIP Model

Parameter	**Value**	**Units**
Torso Mass (M)	80	kg
Torso Inertia (J)	5	kg m^2
Leg Rest Length (l_0)	1	m
Leg Spring Stiffness (k_{leg})	30M$g l_0$=23.52	kN/m
Hip - COM distance (L)	0.1	m
Gravity constant (g)	9.8	m

The running gaits of the ASLIP are composed of stance phases and flight phases, which will be denoted as "s" and "f", respectively. Running is modeled as a hybrid system, which has continuous-time dynamics for each phase, separated by event-based transitions.

Dynamics in Continuous Time

The configuration space Q for both the stance and flight phases can be parameterized by the Cartesian coordinates x_{cm} and y_{cm} of the COM together with the torso angle θ, i.e., $q = (x_{\text{cm}}, y_{\text{cm}}, \theta)' \in Q$. Without losing generality, it will be assumed that at stance phase the origin of x_{cm} is reset to the toe to facilitate the description of the

energy stored in the leg spring. At flight, the robot undergoes a ballistic motion, and the dynamics can be written in state-space form as

$$\dot{x} = f_{\mathrm{f}}(x) = \begin{pmatrix} \dot{x}_{\mathrm{cm}} \\ \dot{y}_{\mathrm{cm}} \\ \dot{\theta} \\ 0 \\ -g \\ 0 \end{pmatrix}, \tag{3.1}$$

where $x \in \mathcal{X} := \{(q', \dot{q}')' \mid q \in Q,\ \dot{q} \in \mathbb{R}^3\}$ is the state vector. At stance, the method of Lagrange is used to derive the equation of motion. The potential and kinetic energies at stance are

$$V_{\mathrm{s}}(q) = Mgy_{\mathrm{cm}} + \frac{1}{2}k_{\mathrm{leg}}(l_0 - \sqrt{(x_{\mathrm{cm}} - L\cos\theta)^2 + (y_{\mathrm{cm}} - L\sin\theta)^2})^2 \tag{3.2}$$

and

$$T(\dot{q}) = \frac{M\dot{x}_{\mathrm{cm}}^2}{2} + \frac{M\dot{y}_{\mathrm{cm}}^2}{2} + \frac{J\dot{\theta}^2}{2}\ , \tag{3.3}$$

where l_0 is the rest length of the springy leg. The Lagrangian of the system is defined as

$$\mathcal{L}_{\mathrm{s}}(q, \dot{q}) = T(\dot{q}) - V_{\mathrm{s}}(q). \tag{3.4}$$

Using Lagrange's equation

$$\frac{d}{dt}\left(\frac{\partial \mathcal{L}}{\partial \dot{q}_j}\right) = \frac{\partial \mathcal{L}}{\partial q_j} + J_{\mathrm{Jac}}^T \tau_{\mathrm{hip}}\ , \tag{3.5}$$

the equation of motion can be determined. In (3.5), the control input τ_{hip} is mapped into the generalized coordinates by the transpose of the Jacobian J_{Jac} defined as

$$J_{\mathrm{Jac}} = \frac{\partial \psi(q)}{\partial q} = \begin{pmatrix} \dfrac{1}{(\frac{x_{\mathrm{hip}}^2}{y_{\mathrm{hip}}^2} + 1)y_{\mathrm{hip}}} \\ \dfrac{x_{\mathrm{hip}}}{(\frac{x_{\mathrm{hip}}^2}{y_{\mathrm{hip}}^2} + 1)y_{\mathrm{hip}}^2} \\ \dfrac{x_{\mathrm{cm}}^2 + y_{\mathrm{cm}}^2 - Lx_{\mathrm{cm}}\cos\theta - Ly_{\mathrm{cm}}\sin\theta}{L^2 + x_{\mathrm{cm}}^2 + y_{\mathrm{cm}}^2 - 2Lx_{\mathrm{cm}}\cos\theta - 2Ly_{\mathrm{cm}}\sin\theta} \end{pmatrix}', \tag{3.6}$$

where $x_{\text{hip}} = x_{\text{cm}} - L\cos\theta$ and $y_{\text{hip}} = y_{\text{cm}} - L\sin\theta$ are the hip coordinates; $\psi(q)$ is the relative angle between torso and leg defined in Fig. 3.1(a). Similar to flight, the stance phase dynamics can also be written in state-space form as

$$\dot{x} = f_{\text{s}}(x) + g_{\text{s}}(x)u = \begin{pmatrix} \dot{x}_{\text{cm}} \\ \dot{y}_{\text{cm}} \\ \dot{\theta} \\ -\frac{1}{M}\cdot k_{\text{leg}}(l_0 - l)\cdot\frac{-x_{\text{hip}}}{l} \\ -g - \frac{1}{M}\cdot k_{\text{leg}}(l_0 - l)\cdot\frac{-y_{\text{hip}}}{l} \\ -\frac{k_{\text{leg}}(l_0 - l)}{J}\cdot\frac{y_{\text{hip}}L\cos\theta - x_{\text{hip}}L\sin\theta}{l} \end{pmatrix} + \begin{pmatrix} 0 \\ 0 \\ 0 \\ \frac{J_{\text{Jac},1}}{M} \\ \frac{J_{\text{Jac},2}}{M} \\ \frac{J_{\text{Jac},3}}{J} \end{pmatrix}\tau_{\text{hip}} \ , \tag{3.7}$$

where $l = \sqrt{(x_{\text{cm}} - L\cos\theta)^2 + (y_{\text{cm}} - L\sin\theta)^2}$ is the length of the leg at stance phase, and $J_{\text{Jac},i}$ is the i-th element of J_{Jac} defined in (3.6).

To summarize, for each phase $i \in \{\text{f}, \text{s}\}$, the dynamics equation can be written in state-space form as

$$\dot{x} = f_i(x) + g_i(x)u, \tag{3.8}$$

where u is hip torque τ_{hip} ($u = 0$ for flight phase).

Event-based Transitions

The model enters the flight phase when the ground reaction force (GRF) becomes zero, or equivalently, when the springy leg reaches its natural length. Conversely, the model enters the stance phase when the vertical distance from the toe to the ground becomes zero. The liftoff and touchdown events are captured by the zero-crossing of the threshold functions $H_{\text{s}\to\text{f}}(x)$ and $H_{\text{f}\to\text{s}}(x)$:

$$H_{\text{s}\to\text{f}}(x) = l_0 - \sqrt{(x_{\text{cm}} - L\cos\theta)^2 + (y_{\text{cm}} - L\sin\theta)^2} \tag{3.9}$$

$$H_{\text{f}\to\text{s}}(x, \gamma) = y_{\text{cm}} - L\sin\theta - l_0\cos\gamma \ . \tag{3.10}$$

Notice that the touchdown event depends on the leg angle γ, which is set by the control policy. The angle γ can be a constant or a function of the state and/or time.

Flow, Flow Map and Poincaré Return Map

Under the influence of a state feedback control law $u = \Gamma(x)$, the closed-loop dynamics of the system becomes $\dot{x} = f_{\mathrm{cl},i}(x)$. For each phase $i \in \{\mathrm{f}, \mathrm{s}\}$, let $\phi_i(t, x_0)$ be a solution of (3.8) with initial condition $x_0 \in TQ$, that is:

$$\phi_i(t, x_0) := x_0 + \int_{t_0}^{t} f_{\mathrm{cl},i}(x) d\eta \ . \tag{3.11}$$

With a slight abuse of notation, define $\phi_i^t(x_0) := \phi_i(t, x_0)$. The system evolves according to the continuous-time dynamics until the corresponding threshold function becomes zero. The duration of the continuous-time evolution which defines the time-to-switch function $T_i(x_0) : \mathcal{X} \to \mathbb{R}$, by

$$T_{\mathrm{s}}(x_0) := \inf\{t > 0 \mid H_{\mathrm{s}\to\mathrm{f}}(\phi_{\mathrm{s}}^t(x_0)) = 0\} \tag{3.12}$$

for the stance and

$$T_{\mathrm{f}}(x_0) := \inf\{t > 0 \mid H_{\mathrm{f}\to\mathrm{s}}(\phi_{\mathrm{f}}^t(x_0)) = 0\} \tag{3.13}$$

for the flight phase. With these definitions, the flow map $\hat{F}_i(x_0) : \mathcal{X} \to \mathcal{X}$ for each phase can be defined as

$$\hat{F}_i(x_0) = \phi_i^{T_i(x_0)}(x_0), \tag{3.14}$$

which takes the initial state x_0 of a phase to the corresponding exit state.

A stride-one running gait is composed of one complete stance phase and one complete flight phase. Let $\mathcal{S} \subset \mathcal{X}$ be defined as follows

$$\mathcal{S} := \{x \in \mathcal{X} \mid H_{\mathrm{f}\to\mathrm{s}}(x) = 0,\ T_{\mathrm{s}}(x) > 0,\ T_{\mathrm{f}}(\hat{F}_{\mathrm{s}}(x)) > 0\}. \tag{3.15}$$

Intuitively, $\mathcal{S}$ comprises all the touchdown states of ASLIP which can lead to a complete running stride (not necessarily periodic) with non-trivial stance and flight durations. The stride map $\hat{F} : \mathcal{S} \to \mathcal{X}$ can be defined through the composition of the flow maps of the two phases, namely:

$$\hat{F} = \hat{F}_{\mathrm{f}} \circ \hat{F}_{\mathrm{s}} \ . \tag{3.16}$$

The method of Poincaré is used to obtain periodic gaits and evaluate their stability. Notice that the horizontal position x_{cm} of the COM is a monotonically increasing variable, and hence it is projected out in defining the Poincaré map. Define Π to be the projection of the state vector x to its non-x_{cm} component $z = (y_{\text{cm}}, \theta, \dot{x}_{\text{cm}}, \dot{y}_{\text{cm}}, \dot{\theta})'$ [1]

$$\Pi(x) := [\mathbf{0}_{5\times 1} \quad I_{5\times 5}]\, x \tag{3.17}$$

and define the map

$$\Sigma_{\text{s}}(z) := \begin{pmatrix} L\cos\theta - \sqrt{l_0^2 - (y_{\text{cm}} - L\sin\theta)^2} \\ z \end{pmatrix} \tag{3.18}$$

which basically resets the origin of x_{cm} at the toe at the beginning of the stance phase. With these definitions, the stride-one Poincaré return map $P_{\text{one}} : \Pi(\mathcal{S}) \to \Pi(\mathcal{S})$ is defined by projecting out x_{cm} from the stride map $\hat{F}$, i.e.,

$$P_{\text{one}}(z) := \Pi \circ \hat{F}_{\text{f}} \circ \hat{F}_{\text{s}} \circ \Sigma_{\text{s}} \ . \tag{3.19}$$

The stride-two Poincaré return map P_{two}, is defined accordingly by a composition of P_{one}:

$$P_{\text{two}} = \Pi \circ \hat{F}_{\text{f}_2} \circ \hat{F}_{\text{s}} \circ \Sigma \circ \Pi \circ \hat{F}_{\text{f}_1} \circ \hat{F}_{\text{s}} \circ \Sigma_{\text{s}} \ , \tag{3.20}$$

where $\hat{F}_{\text{f}_1}$ and $\hat{F}_{\text{f}_2}$ are flight phase flow maps which could have different leg control strategies γ_1 and γ_2.

Spring-Loaded Inverted Pendulum

The SLIP corresponds to the case where the rigid torso in the ASLIP is replace with a point mass located at the hip joint ($L = 0$). The state of the system can be fully described by $q = (x_{\text{cm}}, y_{\text{cm}})' \in Q$ and $x \in \mathcal{X} := \{(q', \dot{q}')' \mid q \in Q,\ \dot{q} \in \mathbb{R}^2\}$. The threshold functions, flow map and Poincaré map can be obtained accordingly. In

[1] Notation: $x \in \mathcal{X}$ denotes the complete state vector, and flow maps associated with it are signified by "ˆ". $z \in \Pi(\mathcal{X})$, denotes the states after projecting out x_{cm} and "ˆ" is removed from the corresponding quantities.

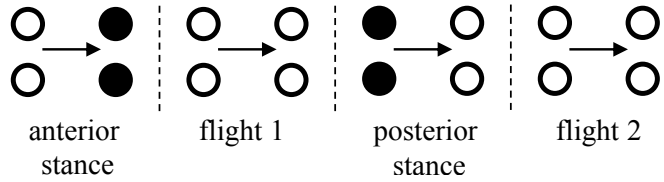

Figure 3.2: Footfall pattern of a bounding gait. Solid circles indicate legs in contact with the ground and white circles indicate legs in the air. The two flight phases "f_1" and "f_2" are distinguished by which stance phase it follows.

the following, *the notation of SLIP will be kept the same as ASLIP* when there is no ambiguity.

3.1.2 Quadrupedal Bounding

Figure 3.1(b) shows the reduced model employed to study quadrupedal bounding. Figure 3.2 describes the footfall pattern of a quadrupedal bounding gait. In bounding gait, the robot always uses its front or back legs in unison. As a result, massless *virtual legs* are used to represent the collective effects of the physical leg pairs.

In this chapter, we restrict our attention to bounding *without double stance* phase, which is composed of three different phases: the stance-anterior "sa", the stance-posterior "sp" and the flight "f" phases. The two flight phases of the quadruped are distinguished as "f_1" and "f_2", indicating the possibilities of using a different leg placement strategy. These phases are separated by touchdown and liftoff events for the back or front leg pairs, which are denoted by "td" and "lo", respectively. The geometric and inertia parameters are given in Table 3.2. They roughly correspond to the quadrupedal robot Scout II [71].

Dynamics in Continuous Time

Similar to the ASLIP, in each phase, the configuration space Q can be parameterized by $q = (x_{\text{cm}}, y_{\text{cm}}, \theta)' \in Q$. For convenience, at stance phase the origin of x_{cm} is reset to the toe in contact with ground.

Table 3.2: Mechanical Parameters of the Reduced-order Quadrupedal Model

Parameter	**Value**	**Units**
Torso Mass (M)	20.865	kg
Torso Inertia (J)	1.39	kg m^2
Hip-to-Shoulder spacing ($2L$)	0.276×2	m
Nominal Leg Length (l_0)	0.323	m
Leg Spring Constant (k_{leg})	7040	N/m

In contrast to the ASLIP model, where the hip torque is necessary to maintain the upright posture of the torso, in quadrupedal running with bounding gait, torso stabilization does not require feedback control specifically devoted to it [74]. In addition, in the context of our massless leg template, leg placement does not require an input torque at the hip, as it is achieved kinematically. Hence, in the quadrupedal model we do not introduce torques at the hip joint. The model is passive and conservative. During the flight phase the torso goes through a ballistic motion and the vector field is the same as (3.1). During the anterior stance and posterior stance phases, the potential energy is given by

$$V_{\text{sa}}(q) = Mgy_{\text{cm}} + \frac{1}{2}k(l_0 - \sqrt{(x_{\text{cm}} + L\cos\theta)^2 + (y_{\text{cm}} + L\sin\theta)^2})^2 \tag{3.21}$$

$$V_{\text{sp}}(q) = Mgy_{\text{cm}} + \frac{1}{2}k(l_0 - \sqrt{(x_{\text{cm}} - L\cos\theta)^2 + (y_{\text{cm}} - L\sin\theta)^2})^2 \ , \tag{3.22}$$

respectively. The corresponding kinetic energy during both stance phases is

$$T(\dot{q}) = \frac{M\dot{x}_{\text{cm}}^2}{2} + \frac{M\dot{y}_{\text{cm}}^2}{2} + \frac{J\dot{\theta}^2}{2} \ . \tag{3.23}$$

Using the method of Lagrangian, the equations of motion can be derived, resulting in

the following vector fields governing the dynamics of the system during stance:

$$f_{\mathrm{sa}}(x) = \begin{pmatrix} \dot{x}_{\mathrm{cm}} \\ \dot{y}_{\mathrm{cm}} \\ \dot{\theta} \\ -\frac{1}{M} \cdot k_{\mathrm{leg}}(l_0 - l_{\mathrm{sa}}) \cdot \frac{-(x_{\mathrm{cm}} + L\cos\theta)}{l_{\mathrm{sa}}} \\ -g - \frac{1}{M} \cdot k_{\mathrm{leg}}(l_0 - l_{\mathrm{sa}}) \cdot \frac{-(y_{\mathrm{cm}} + L\sin\theta)}{l_{\mathrm{sa}}} \\ -\frac{k_{\mathrm{leg}}(l_0 - l_{\mathrm{sa}})}{J} \cdot \frac{(x_{\mathrm{cm}} + L\cos\theta)L\sin\theta - (y_{\mathrm{cm}} + L\sin\theta)L\cos\theta}{l_{\mathrm{sa}}} \end{pmatrix} \tag{3.24}$$

and

$$f_{\mathrm{sp}}(x) = \begin{pmatrix} \dot{x}_{\mathrm{cm}} \\ \dot{y}_{\mathrm{cm}} \\ \dot{\theta} \\ -\frac{1}{M} \cdot k_{\mathrm{leg}}(l_0 - l_{\mathrm{sp}}) \cdot \frac{-(x_{\mathrm{cm}} - L\cos\theta)}{l_{\mathrm{sp}}} \\ -g - \frac{1}{M} \cdot k_{\mathrm{leg}}(l_0 - l_{\mathrm{sp}}) \cdot \frac{-(y_{\mathrm{cm}} - L\sin\theta)}{l_{\mathrm{sp}}} \\ -\frac{k_{\mathrm{leg}}(l_0 - l_{\mathrm{sp}})}{J} \cdot \frac{(y_{\mathrm{cm}} - L\sin\theta)L\cos\theta - (x_{\mathrm{cm}} - L\cos\theta)L\sin\theta}{l_{\mathrm{sp}}} \end{pmatrix}, \tag{3.25}$$

where $l_{\mathrm{sa}} = \sqrt{(x_{\mathrm{cm}} + L\cos\theta)^2 + (y_{\mathrm{cm}} + L\sin\theta)^2}$ is the length of the leg at anterior stance phases and $l_{\mathrm{sp}} = \sqrt{(x_{\mathrm{cm}} - L\cos\theta)^2 + (y_{\mathrm{cm}} - L\sin\theta)^2}$ is the length of the leg at posterior stance phase.

To summarize, for each $i \in \{\mathrm{sa}, \mathrm{f}_1, \mathrm{sp}, \mathrm{f}_2\}$, the vector field is of the form

$$\dot{x} = f_i(x), \tag{3.26}$$

where $x \in \mathcal{X} := \{(q', \dot{q}')' \mid q \in Q,\ \dot{q} \in \mathbb{R}^3\}$ is the state variable.

Event-based Transition

Transitions between different phases occur when certain threshold functions $H : \mathcal{X} \to \mathbb{R}$ cross their zero value. Assuming that liftoff occurs when a leg extends to

its natural length, the threshold functions that correspond to the anterior and posterior legs liftoff are, respectively,

$$H_{\mathrm{sa}\to\mathrm{f}}(x) = l_0 - \sqrt{(x_{\mathrm{cm}} + L\cos\theta)^2 + (y_{\mathrm{cm}} + L\sin\theta)^2} \tag{3.27}$$

$$H_{\mathrm{sp}\to\mathrm{f}}(x) = l_0 - \sqrt{(x_{\mathrm{cm}} - L\cos\theta)^2 + (y_{\mathrm{cm}} - L\sin\theta)^2} \ . \tag{3.28}$$

On the other hand, the threshold functions which describe touchdown events of the two legs on flat ground are defined as

$$H_{\mathrm{f}_1\to\mathrm{sp}}(x, \gamma_p) = y_{\mathrm{cm}} - L\sin\theta - l_0\cos\gamma_p \tag{3.29}$$

$$H_{\mathrm{f}_2\to\mathrm{sa}}(x, \gamma_a) = y_{\mathrm{cm}} + L\sin\theta - l_0\cos\gamma_a \tag{3.30}$$

which corresponds to the vertical height of the toes from the substrate. Notice that γ_p and γ_a depend on the leg angle control policy and they can either be constants or functions of the states and time.

Flow, Flow Maps and Poincaré Return Map

For each $i \in \{\mathrm{sa}, \mathrm{f}_1, \mathrm{sp}, \mathrm{f}_2\}$, let $\phi_i(t, x_0)$, $t \geq t_0$, be a maximal solution of (3.26) with initial condition $x_0 \in TQ$; that is, $\phi_i(t_0, x_0) = x_0$ and

$$\phi_i(t, x_0) = x_0 + \int_{t_0}^{t} f_i\left(\phi_i(\tau, x_0)\right) d\tau \ . \tag{3.31}$$

With a slight abuse of notation, define $\phi_i^t(x_0) = \phi_i(t, x_0)$. The time-to-switch function $T_i : \mathcal{X} \to \mathbb{R}$ for each phase $i \in \{\mathrm{sa}, \mathrm{f}_1, \mathrm{sp}, \mathrm{f}_2\}$ is defined by

$$T_{\mathrm{sa}}(x_0) = \inf\{t > 0 \mid H_{\mathrm{sa}\to\mathrm{f}}(\phi_{\mathrm{sa}}^t(x_0)) = 0\} \ , \tag{3.32}$$

$$T_{\mathrm{sp}}(x_0) = \inf\{t > 0 \mid H_{\mathrm{sp}\to\mathrm{f}}(\phi_{\mathrm{sp}}^t(x_0)) = 0\} \ , \tag{3.33}$$

and

$$T_{\mathrm{f}}(x_0, \gamma) = \inf\{t > 0 \mid H_{\mathrm{f}_2\to\mathrm{sa}}(\phi_{\mathrm{f}}^t(x_0), \gamma_a) = 0 \text{ or } H_{\mathrm{f}_1\to\mathrm{sp}}(\phi_{\mathrm{f}}^t(x_0), \gamma_p) = 0\}, \tag{3.34}$$

where $\gamma \in \{\gamma_{\mathrm{p}}, \gamma_{\mathrm{a}}\}$. With these definitions at hand, the flow map $F_i : \mathcal{X} \to \mathcal{X}$ for each phase $i \in \{\mathrm{sa}, \mathrm{f}_1, \mathrm{sp}, \mathrm{f}_1\}$ is

$$\hat{F}_i(x_0) = \phi_i^{T_i(x_0)}(x_0) \ . \tag{3.35}$$

In words, the flow map takes "entry" conditions to "exit" conditions for each phase. Assume, without loss of generality, that the bounding cycle begins at the touchdown of the anterior leg, and define $\mathcal{S}_{\mathrm{sa}} \subset \mathcal{X}$ to be the set of anterior leg touchdown states that can result in a complete bounding cycle (not necessarily periodic)

$$\mathcal{S}_{\mathrm{sa}} := \{x \in \mathcal{X} \mid H_{\mathrm{f}_2 \to \mathrm{sa}}(x) = 0, T_{\mathrm{f}}(\hat{F}_{\mathrm{sp}} \circ \hat{F}_{\mathrm{f}_1} \circ \hat{F}_{\mathrm{sa}}(x)) > 0\} \ . \tag{3.36}$$

The stride map $\hat{F} : \mathcal{S}_{\mathrm{sa}} \to \mathcal{X}$ can then be defined through the composition of the corresponding flow maps as

$$\hat{F} = \hat{F}_{\mathrm{f}_2} \circ \hat{F}_{\mathrm{sp}} \circ \hat{F}_{\mathrm{f}_1} \circ \hat{F}_{\mathrm{sa}} \ . \tag{3.37}$$

The method of Poincaré is used to evaluate stability of the gait. As in the ASLIP model of Sec. 3.1.1, the horizontal position x_{cm} of the COM is a cyclic variable and will be projected out from the stride map by the operator Π defined in (3.17). In addition, we define the maps

$$\Sigma_{\mathrm{sa}}(z) := \begin{pmatrix} -L\cos\theta - \sqrt{l_0^2 - (y_{\mathrm{cm}} + L\sin\theta)^2} \\ z \end{pmatrix} \tag{3.38}$$

$$\Sigma_{\mathrm{sp}}(z) := \begin{pmatrix} L\cos\theta - \sqrt{l_0^2 - (y_{\mathrm{cm}} - L\sin\theta)^2} \\ z \end{pmatrix} \tag{3.39}$$

which reset the origin of x_{cm} at the beginning of the stance anterior and the stance posterior phases; z is the non-x_{cm} component of the state vector. Then, the Poincaré return map $P : \Pi(\mathcal{S}) \to \Pi(\mathcal{S})$ can be defined through the stride map (3.37) as

$$P := \Pi \circ \hat{F}_{\mathrm{f}_2} \circ \hat{F}_{\mathrm{sp}} \circ \Sigma_{\mathrm{sp}} \circ \Pi \circ \hat{F}_{\mathrm{f}_1} \circ \hat{F}_{\mathrm{sa}} \circ \Sigma_{\mathrm{sa}} \ . \tag{3.40}$$

As in the stride map given in (3.37), at the beginning of the stance phases, the Poincaré return map utilizes $\Sigma_{\mathrm{sp}}(z)$ and $\Sigma_{\mathrm{sa}}(z)$ to reset the origin of the horizontal displacement x_{cm}; at the end of the stance phases, it projects out the x_{cm} component.

3.2 Stability Analysis of ASLIP

In this section, we first describe the proposed ASLIP controller. Then, we analyze stability property of the model under the control law. It is proved that with a symmetry-based leg angle control law and a torso balancing strategy, every point on a special subset of $\Pi(\mathcal{S})$ is a fixed point of P_{two}, and is neutrally stable.

3.2.1 Controller for ASLIP Model

Leg Angle Control Based on Symmetry

The leg touchdown angle is a powerful control input for locomotion and it has been extensively used to stabilize running gaits [74]. Leg touchdown angle control policies have been derived using symmetry arguments regarding the gait. Symmetric gaits are common idealizations of certain locomotion behaviors [76]. For example, consider human running. During the motion, the two legs are kept roughly in a symmetric configuration with respect to the frontal plane passing through the hip [75]. This type of symmetry is termed "scissor symmetry". The same phenomenon has also been observed in the context of the SLIP model in [87], and it was used in [86] to propose a leg control strategy that enlarges the basin of attraction of running motions for the model of *blaberus discoidalis*:

$$\gamma_{\text{ASLIP}}^{\text{sym}} = -\gamma_{LO} \ . \tag{3.41}$$

Basically, this control law sets the leg touchdown angle to a constant value, which equals the negative of the previous liftoff angle.

Torso Control Based on the Virtual Pivot Point (VPP) Concept

The nontrivial torso of the ASLIP model requires active balance. Based on the observation that in human locomotion the ground reaction force (GRF) intersect at a point above the COM, [58] proposed the virtual pivoting point (VPP) concept. This concept has been used in [59] to stabilize the torso of ASLIP model

$$\tau_{\text{hip}} = k_{\text{leg}}(l_0 - l)l\frac{(L + r_{\text{P}})\sin\psi}{l - (L + r_{\text{P}})\cos\psi} \ , \tag{3.42}$$

where $l = \sqrt{(x_{\text{cm}} - L\cos\theta)^2 + (y_{\text{cm}} - L\sin\theta)^2}$ is the length of the leg and r_{P} is the distance from COM to VPP point. The physical meaning of this control input is shown in Fig. 3.1(a), where the hip torque τ_{hip} at stance phase is used to redirect the GRF to pass through the VPP point which is located above the COM. Numerical simulations have proved that this concept can lead to self-stable running gaits under a constant leg touchdown angle policy [58].

In the following analysis we use a special version of the controller where $r_{\text{P}} = 0$:

$$\tau_{\text{hip}} = k_{\text{leg}}(l_0 - l)l\frac{L\sin\psi}{l - L\cos\psi} \ . \tag{3.43}$$

Equation (3.43) is a special case where the VPP coincides with the COM of the torso. This controller has originally been proposed in [70], prior to the introduction of VPP, and it effectively makes the GRF pass through the COM thereby the pitch dynamics will be governed by

$$\ddot{\theta} = 0 \ . \tag{3.44}$$

This can be derived by using the stance phase dynamics given in (3.7).

3.2.2 Hybrid Zero Dynamics of ASLIP

Similar to [70], we define output y as

$$y := \theta - \pi/2 \ , \tag{3.45}$$

which is the angle formed by the torso and the vertical line. Under the constraint $y \equiv 0$, the system evolves on the set $\mathcal{Z}$

$$\mathcal{Z} = \{x \mid y = 0, \dot{y} = 0\} \ , \tag{3.46}$$

which is referred as *zero dynamics manifold*. The dynamics of the system restricted to $\mathcal{Z}$ is the *zero dynamics*–the maximal internal dynamics compatible with the output y being identically zero [13]. Notice that the hip control input defined in (3.43) enforces

$\ddot{\theta} = 0$, as stated in (3.44). Applying the hip controller (3.43) and imposing the constrain $\theta = \pi/2$ to (3.7), the zero dynamics at stance phase is explicitly given by

$$f^{\mathcal{Z}}_{\text{cl,s}}(x) = \begin{pmatrix} \dot{x}_{\text{cm}} \\ \dot{y}_{\text{cm}} \\ 0 \\ \dfrac{x_{\text{cm}} k_{\text{leg}}(l_0 - l^{\mathcal{Z}})}{M l^{\mathcal{Z}}} \\ -g + \dfrac{y_{\text{cm}} k_{\text{leg}}(l_0 - l^{\mathcal{Z}})}{M l^{\mathcal{Z}}} \\ 0 \end{pmatrix} + \frac{k_{\text{leg}}(l_0 - l^{\mathcal{Z}})}{M} \begin{pmatrix} 0 \\ 0 \\ 0 \\ \dfrac{-x_{\text{cm}}(y_{\text{cm}} - L)L}{l^{\mathcal{Z}}(x^2_{\text{cm}} + y^2_{\text{cm}} - L y_{\text{cm}})} \\ \dfrac{-x^2_{\text{cm}} L}{l^{\mathcal{Z}}(x^2_{\text{cm}} + y^2_{\text{cm}} - L y_{\text{cm}})} \\ 0 \end{pmatrix} \tag{3.47}$$

where $l^{\mathcal{Z}} = \sqrt{x^2_{\text{cm}} + (y_{\text{cm}} - L)^2}$ is the leg length on the zero dynamics manifold.

Since ASLIP has a trivial jump map—that is, there is no discontinuity in the state vector as the system transits from flight to stance and from stance to flight—the output remains unchanged through the transitions and the zero dynamics can be extended to include both the continuous-time dynamics and the discrete-time dynamics, which is referred as the *Hybrid Zero Dynamics*. Note also that under the control law (3.43), the GRF would pass through the COM of the torso so that $\ddot{\theta} = 0$ during stance. The flight phase is also governed by $\ddot{\theta} = 0$. As a result, the system is hybrid invariant: once it is in $\mathcal{Z}$, it will stay in it.

3.2.3 Stability of Stride Two Gait on the Zero Dynamics Manifold

The following theorem shows that under the influence of the touchdown angle policy (3.41) and the controller (3.43), every point of $\Pi(\mathcal{Z})$ at which the stride-two map P_{two} is defined, is essentially a fixed point of P_{two}.

Theorem 2. *Under the leg angle control law defined in* (3.41) *and torso control law defined in* (3.43)*, every point in* $\Pi(\mathcal{Z}) \cap \Pi(\mathcal{S})$ *is a fixed point of the restricted stride-two Poincaré return map* $P^{\mathcal{Z}}_{\text{two}}$*, where* $\mathcal{Z}$ *is defined by* (3.46)*,* $\mathcal{S}$ *is defined by* (3.15)*,* Π *by* (3.17)*, and* $P^{\mathcal{Z}}_{\text{two}}$ *is the restriction of* P_{two} *on* $\Pi(\mathcal{Z})$*. In addition, they are all neutrally stable for* $P^{\mathcal{Z}}_{\text{two}}$ *on the manifold* $\Pi(\mathcal{Z})$ *in the sense of Lyapunov.*

The proof is organized in three lemmas. Before we proceed, $P^{\mathcal{Z}}_{\text{two}}$ is re-organized as follows. Define the diagonal matrix

$$\hat{G}_{\text{ASLIP}} := \text{diag}\ [-1, 1, 1, 1, -1, 1]\ , \tag{3.48}$$

and notice that $\hat{G}_{\text{ASLIP}} \circ \hat{G}_{\text{ASLIP}} = I_{6\times 6}$ so that (3.20) can be written as

$$P^{\mathcal{Z}}_{\text{two}} = \Pi \circ \hat{F}_{\text{f}_2} \circ \hat{G}_{\text{ASLIP}} \circ \hat{G}_{\text{ASLIP}} \circ \hat{F}_{\text{s}} \circ \Sigma_{\text{s}} \circ \Pi \circ \hat{F}_{\text{f}_1} \circ \hat{G}_{\text{ASLIP}} \circ \hat{G}_{\text{ASLIP}} \circ \hat{F}_{\text{s}} \circ \Sigma_{\text{s}}\ . \tag{3.49}$$

As a result of the decoupling of the motion at flight phase, we get

$$\Sigma_{\text{s}} \circ \Pi \circ \hat{F}_{\text{f}_1} \circ \hat{G}_{\text{ASLIP}} = \Sigma_{\text{s}} \circ F_{\text{f}_1} \circ \Pi \circ \hat{G}_{\text{ASLIP}} = \Sigma_{\text{s}} \circ F_{\text{f}_1} \circ G_{\text{ASLIP}} \circ \Pi\ , \tag{3.50}$$

where F_{f_1} is the non-x_{cm} component of $\hat{F}_{\text{f}_1}$ under the control policy γ_1 and $G_{\text{ASLIP}} = \text{diag}\ [1, 1, 1, -1, 1]$ [2]. Similarly, the restricted stride-two Poincaré return map in (3.49) can be further simplified as:

$$P^{\mathcal{Z}}_{\text{two}} = F_{\text{f}_2} \circ G_{\text{ASLIP}} \circ \Pi \circ \hat{G}_{\text{ASLIP}} \circ \hat{F}_{\text{s}} \circ \Sigma_{\text{s}} \circ F_{\text{f}_1} \circ G_{\text{ASLIP}} \circ \Pi \circ \hat{G}_{\text{ASLIP}} \circ \hat{F}_{\text{s}} \circ \Sigma_{\text{s}}. \tag{3.51}$$

When the symmetry leg control policy $\gamma^{\text{sym}}_{\text{ASLIP}}$ defined in (3.41) is adopted for the flight phases, the non-x_{cm} flight map F_{f_1} or F_{f_2}—the only difference between the two phases is the leg control policy—will be denoted as $F_{\text{f}\gamma^{\text{sym}}_{\text{ASLIP}}}$. With this definition, we have the following lemma:

Lemma 1. *If the symmetry leg angle control policy* (3.41) *is adopted for the flight phase, then for every liftoff state* $z_0 \in \Pi(\mathcal{Z})$ *with* $\dot{y}_{\text{cm}} > 0$, $F_{\text{f}\gamma^{\text{sym}}_{\text{ASLIP}}}(z_0) = G_{\text{ASLIP}}(z_0)$.

Proof. This lemma is a direct result of the symmetric leg angle: due to this policy, the ascending and descending part of the flight phase have the same duration. As a consequence of the fact that the motion of the system during flight is ballistic, only the vertical velocity changes direction. Notice that the torso will maintain its vertical configuration since it starts from the set $\mathcal{Z}$ with $\dot{\theta} = 0$ and $\theta = \frac{\pi}{2}$. □

[2] G_{ASLIP} can be obtained by directly checking the matrix multiplication of $\hat{G}_{\text{ASLIP}} \circ \Pi$

As a result, if $\gamma_{\text{ASLIP}}^{\text{sym}}$ is adopted for F_{f1}, (3.50) can be simplified to

$$\Sigma_{\text{s}} \circ F_{\text{f}_1} \circ G_{\text{ASLIP}} \circ \Pi = \Sigma_{\text{s}} \circ F_{\text{f}\gamma_{\text{ASLIP}}^{\text{sym}}} \circ G_{\text{ASLIP}} \circ \Pi = \Sigma_{\text{s}} \circ G_{\text{ASLIP}} \circ G_{\text{ASLIP}} \circ \Pi = \Sigma_{\text{s}} \circ \Pi \quad (3.52)$$

and the restricted stride-two Poincaré return map (3.51) is simplified as

$$P_{\text{two}}^{\mathcal{Z}} = F_{\text{f}_2} \circ G_{\text{ASLIP}} \circ \Pi \circ \hat{G}_{\text{ASLIP}} \circ \hat{F}_{\text{s}} \circ \Sigma_{\text{s}} \circ \Pi \circ \hat{G}_{\text{ASLIP}} \circ \hat{F}_{\text{s}} \circ \Sigma_{\text{s}}. \quad (3.53)$$

Lemma 2. *For every touchdown state $x_0 \in \mathcal{S} \cap \mathcal{Z}$, under the torso controller (3.43), $\hat{G}_{\text{ASLIP}} \circ \hat{F}_s \circ \hat{G}_{\text{ASLIP}} \circ \hat{F}_s(x_0) = I_{6\times 6}$, where $\hat{G}$ is defined in (3.48).*

Proof. On $\mathcal{Z}$, the torso will remain vertical due to the controller (3.43). As a result, the model is governed by the zero dynamics. By checking the vector field of (3.47) directly, it can be found that it satisfies the following symmetry property[3]

$$\hat{G}_{\text{ASLIP}} \times f_{\text{cl,s}}^{\mathcal{Z}} = -f_{\text{cl,s}}^{\mathcal{Z}} \circ \hat{G}_{\text{ASLIP}} \quad (3.54)$$

on $\mathcal{Z}$. This is equivalent to

$$\hat{G}_{\text{ASLIP}} \circ \phi_{\text{s}}^{t} = \phi_{\text{s}}^{-t} \circ \hat{G}_{\text{ASLIP}}. \quad (3.55)$$

where ϕ_{s}^{t} is the flow of stance dynamics on $\mathcal{Z}$.

Next we show that the time-to-switch function satisfies $T_{\text{s}} \circ \hat{G}_{\text{ASLIP}} \circ \hat{F}_{\text{s}}(x_0) = T_{\text{s}}(x_0)$. According to the definition, the threshold function of the left side is

$$\begin{aligned} &H_{\text{s}\to\text{f}}(\phi_{\text{s}}^{t} \circ \hat{G}_{\text{ASLIP}} \circ \hat{F}_{\text{s}}(x_0)) = H_{\text{s}\to\text{f}}(\phi_{\text{s}}^{t} \circ \hat{G}_{\text{ASLIP}} \circ \phi_{\text{s}}^{T_{\text{s}}(x_0)}(x_0)) \\ &= H_{\text{s}\to\text{f}}(\hat{G}_{\text{ASLIP}} \circ \phi_{\text{s}}^{T_{\text{s}}(x_0)-t}(x_0)) = H_{\text{s}\to\text{f}}(\phi_{\text{s}}^{T_{\text{s}}(x_0)-t}(x_0)). \end{aligned} \quad (3.56)$$

Noticing that $t = 0$ and $t = T_{\text{s}}(x_0)$ will make the right side of (3.56) equal to zero, and recall that T_{s} is the minimal solution, there is no other $0 < t < T_{\text{s}}$ will make the threshold function be zero. This proves $T_{\text{s}}(x_0) = T_{\text{s}} \circ \hat{G} \circ \hat{F}_{\text{s}}(x_0)$.

[3] This justifies the choice of $\hat{G}_{\text{ASLIP}}$. $\hat{G}_{\text{ASLIP}}$ reverses the sign of horizontal displacement and vertical velocity. This is due to the fact that after stance phase, the torso is in front of the foot and the vertical velocity is changing from downward to upward.

As a result of (3.55) and (3.56), we obtain:

$$\begin{aligned}\hat{G}_{\text{ASLIP}} \circ \hat{F}_{\text{s}} \circ \hat{G}_{\text{ASLIP}} \circ \hat{F}_{\text{s}} &= \hat{G}_{\text{ASLIP}} \circ \phi^{T_{\text{s}}(\hat{G}_{\text{ASLIP}} \circ \hat{F}_{\text{s}}(x_0))} \circ \hat{G}_{\text{ASLIP}} \circ \phi^{T_{\text{s}}(x_0)} \\ &= \phi^{-T_{\text{s}}(G_{\text{ASLIP}} \circ F(x_0))} \circ \phi^{T_{\text{s}}(x_0)} = I_{6\times 6} \ .\end{aligned} \tag{3.57}$$

□

Lemma 3. *For $x_1 := \hat{G}_{\text{ASLIP}} \circ \hat{F}_{\text{s}} \circ \Sigma_{\text{s}}(z_0)$, where $z_0 \in (\Pi(\mathcal{Z}) \cap \Pi(\mathcal{S}))$ is the state of the ASLIP model at the touchdown event (the beginning of stance), $\Sigma_{\text{s}} \circ \Pi(x_1) = I_{6\times 6}$.*

Proof. Define $x_2 := \hat{F}_{\text{s}} \circ \Sigma_{\text{s}}(z_0)$ denoted as $x_2 := (x_{\text{cm},2}, y_{\text{cm},2}, \pi/2, \dot{x}_{\text{cm},2}, \dot{y}_{\text{cm},2}, 0)'$, which is the state at liftoff (end of stance phase). Notice that the COM is in front of the toe at the end of stance phase, $x_{\text{cm},2} = \sqrt{l_0^2 - (y_{\text{cm},2} - L)^2}$. As a result, $x_1 = \hat{G}_{\text{ASLIP}}(x_2)$ will be:

$$x_1 := \hat{G}_{\text{ASLIP}} \circ \hat{F}_{\text{s}} \circ \Sigma_{\text{s}}(z_0) = (-x_{\text{cm},2}, y_{\text{cm},2}, \pi/2, \dot{x}_{\text{cm},2}, -\dot{y}_{\text{cm},2}, 0)'. \tag{3.58}$$

Meanwhile, applying $\Sigma_{\text{s}} \circ \Pi$ on x_1, we get the following

$$\Sigma_{\text{s}} \circ \Pi(x_1) = \begin{bmatrix} -\sqrt{l_0^2 - (y_{\text{cm},2} - L)^2} \\ y_{\text{cm},2} \\ \pi/2 \\ \dot{x}_{\text{cm},2} \\ -\dot{y}_{\text{cm},2} \\ 0 \end{bmatrix} = \begin{bmatrix} -x_{\text{cm},2} \\ y_{\text{cm},2} \\ \pi/2 \\ \dot{x}_{\text{cm},2} \\ -\dot{y}_{\text{cm},2} \\ 0 \end{bmatrix} = x_1. \tag{3.59}$$

□

The proof of Theorem 2 is provided next.

Proof of Theorem 2. The first part of the theorem is an immediate consequence of Lemmas 1, 2 and 3. By applying the leg control policy (3.41) at $\hat{F}_{\text{f1}}$, and using the controller defined in (3.43), (3.53) would now becomes

$$P_{\text{two}}^{\mathcal{Z}} = F_{\text{f}_2} \circ G_{\text{ASLIP}} \circ \underbrace{\Pi \circ \hat{G}_{\text{ASLIP}} \circ \hat{F}_{\text{s}} \circ \Sigma \circ \Pi \circ \hat{G}_{\text{ASLIP}} \circ \hat{F}_{\text{s}} \circ \Sigma}_{id} = F_{\text{f}_2} \circ G_{\text{ASLIP}} \ . \tag{3.60}$$

This shows that the stride-two Poincaré return map is reduced to a flight phase map. Recall that the dynamics of the flight phase can be integrated analytically, $P^{\mathcal{Z}}_{\text{two}}$ is *analytically solvable*. Moreover, if we apply the leg placement control policy $\gamma^{\text{sym}}_{\text{ASLIP}}$ in (3.41) also for flight phase $\hat{F}_{\text{f}_2}$, then the stride-two return map would become

$$P^{\mathcal{Z}}_{\text{two}} = F_{\text{f}_2} \circ G_{\text{ASLIP}} = F_{\text{f}_{\gamma^{\text{sym}}_{\text{ASLIP}}}} \circ G_{\text{ASLIP}} = I_{5\times 5} \tag{3.61}$$

using the result of Lemma 1. As a result, every point on $\Pi(\mathcal{Z}) \cap \Pi(\mathcal{S})$ is a stride-two fixed point of $P^{\mathcal{Z}}_{\text{two}}$, and they are all neutrally stable in the sense of Lyapunov on the manifold $\Pi(\mathcal{Z}) \cap \Pi(\mathcal{S})$. In addition, these points are also fixed points of the full map P^{two}, since the constant torso angle is trivially periodic. □

Remark 1. *A result similar to theorem 2 can be obtained for SLIP model: under the leg angle control law* (3.41)*,* $P_{\text{two}} = I_{3\times 3}$*, indicating that every point on* $\Pi(\mathcal{S})$ *is a stride-two fixed point for SLIP, and they are all neutrally stable in the Lyapunov sense. Figure 3.3 gives the intuition. Under* $\gamma^{\text{sym}}_{\text{ASLIP}}$*, the two stance phases are canceled out by each other. Since the results are proved using the symmetric property of the vector field without any approximation, conclusions on stability can be drawn. In contrast, [86] proved that* (3.41) *will necessarily produce periodic-two gaits for SLIP model by ignoring gravity during stance phase and approximating the stance phase map using conservation of energy. However, no conclusion on stability can be drawn in that case: the approximated linear system has eigenvalues equal to one and the stability property of the original nonlinear system cannot be determined.*

3.2.4 Stabilizing the Full Dynamics

Although every point on $\Pi(\mathcal{Z}) \cap \Pi(\mathcal{S})$ is a fixed point for both $P^{\mathcal{Z}}_{\text{two}}$ and P_{two}, the stability property on the zero dynamics manifold $\mathcal{Z}$ does not carry to the full dynamics. Indeed, when there are disturbances in the θ and /or $\dot{\theta}$ components of the state vector, the system will no longer evolve on the zero dynamics manifold $\mathcal{Z}$ because

under (3.43), θ is not stabilized as can be seen from (3.44). To stabilize the pitch angle, the hip controller in (3.43) is modified as follows:

$$\tau_{\text{hip}} = \tau_{\text{VPP}} + \tau_{\text{finite}} \ , \tag{3.62}$$

where τ_{VPP} is the VPP controller defined in (3.43); τ_{finite} is defined as

$$\tau_{\text{finite}} = \frac{J}{J_{\text{Jac, 3}}} \cdot \frac{-\text{sign}(\dot{y})|\dot{y}|^{\alpha} - \text{sign}(\eta(y,\dot{y}))|\eta(y,\dot{y})|^{\alpha/(2-\alpha)}}{\epsilon} \tag{3.63}$$

where $y = \theta - \pi/2$ is the output defined at (3.46); $\eta(y,\dot{y}) = y + (1/2-\alpha)\text{sign}(\dot{y})|\dot{y}|^{2-\alpha}$ with $\alpha \in (0,1)$; ϵ is used to adjust the rate of convergence; J is the moment of inertia of torso; $J_{\text{Jac, 3}}$ is the third element of the Jacobian defined in (3.6). By checking stance phase vector field (3.7) and recall (3.44), the pitch dynamics will now be governed by

$$\ddot{\theta} = \frac{-\text{sign}(\dot{\theta})|\dot{\theta}|^{\alpha} - \text{sign}(\eta(y,\dot{\theta}))|\eta(y,\dot{\theta})|^{\alpha/(2-\alpha)}}{\epsilon} \tag{3.64}$$

This is exactly the continuous finite-time controller used in [5,6,31] for double integrator. As a result, under hip controller (3.62), the pitch angle will be driven to $\pi/2$ in finite time and the system will eventually converges to the zero dynamics manifold $\mathcal{Z}$. As a result, the zero dynamics manifold $\mathcal{Z}$ is finite attractive under (3.62). Notice that once the system converges to $\mathcal{Z}$, τ_{finite} becomes zero, and the controller (3.62) becomes (3.43). Hence, $\mathcal{Z}$ is hybrid invariant.

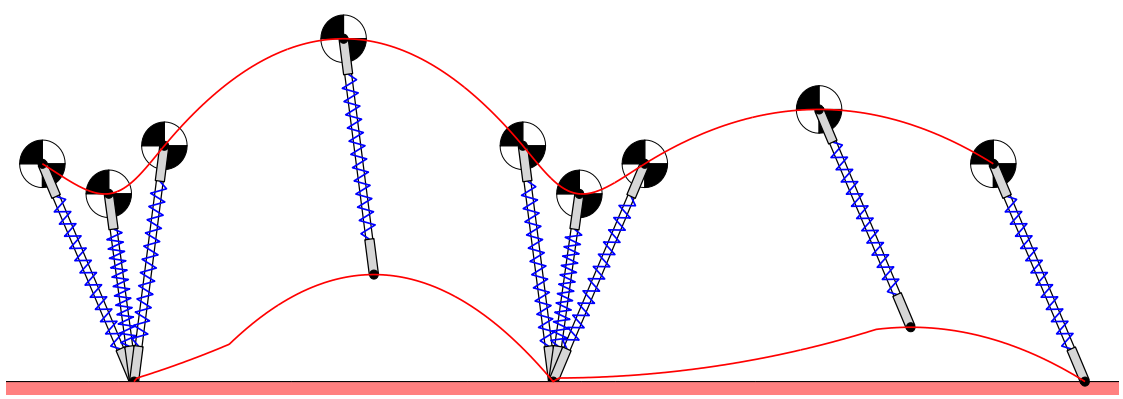

Figure 3.3: Stride-Two gait of SLIP, begins at touchdown event. Every point at the Poincaré section $\mathcal{S}$ is a stride-two fixed point under $\gamma^{\text{sym}}_{\text{ASLIP}}$. Meanwhile, they are all neutrally stable in Lyapunov sense.

As a direct result of theorem [102, Theorem 4.5], we obtain the following lemma:

Lemma 4. *Under* (3.41) *and* (3.62)*, every point on* $\Pi(\mathcal{Z}) \cap \Pi(\mathcal{S})$ *is a fixed point for* P^{two}*, and they are all neutrally stable in Lyapunov sense.*

The performance of the controller will be evaluated numerically later in Sec. 3.4.1.

3.3 Stability Analysis of Quadruped Bounding

In this section, the stability of passive bounding gaits under a family of symmetric leg angle control law is analyzed using a similar approach. Before we proceed, we first factor (3.40) as

$$\begin{aligned} P &= \Pi \circ \hat{F}_{\text{f}_2} \circ \hat{F}_{\text{sp}} \circ \Sigma_{\text{sp}} \circ \Pi \circ \hat{F}_{\text{f}_1} \circ \hat{F}_{\text{sa}} \circ \Sigma_{\text{sa}} \\ &= F_{\text{f}_2} \circ \Pi \circ \hat{F}_{\text{sp}} \circ \Sigma_{\text{sp}} \circ F_{\text{f}_1} \circ \Pi \circ \hat{F}_{\text{sa}} \circ \Sigma_{\text{sa}} \\ &= F_{\text{f}_2} \circ F_{\text{sp}} \circ F_{\text{f}_1} \circ F_{\text{sa}} \\ &= \underbrace{F_{\text{f}_2} \circ G_{\text{quad}}}_{P_2} \circ \underbrace{G_{\text{quad}} \circ F_{\text{sp}} \circ F_{\text{f}_1} \circ F_{\text{sa}}}_{P_1} , \end{aligned} \tag{3.65}$$

where F_{f_2} and F_{f_1} is the restriction of $\hat{F}_{\text{f}_2}$ and $\hat{F}_{\text{f}_1}$ on $\Pi(\mathcal{X})$ so that $\Pi \circ \hat{F}_{\text{f}_2} = F_{\text{f}_1} \circ \Pi$ due to the decoupling of the horizontal motion from the vertical and the rotational motions during flight. $F_i := \Pi \circ \hat{F}_i \circ \Sigma_i$ for $i \in \{\text{sa}, \text{sp}\}$. G_{quad} is a diagonal matrix defined as

$$G_{\text{quad}} := \text{diag}\ [1, -1, 1, -1, 1] \tag{3.66}$$

and $G_{\text{quad}} \cdot G_{\text{quad}} = I_{5\times5}$. Note that the factor P_1 in (3.65) does *not* correspond to the time-reversed flow map of an individual phase; rather it is the time-reversed composition of three flow maps.

3.3.1 Passive Periodic Bounding Gaits

Unlike the ASLIP model, by properly controlling the touchdown angles of the two legs, a number of passive periodic bounding gaits can be found numerically. Figure 3.4 gives the touchdown angles as well as several states of one such gait. From Fig.3.4(a) it can be observed that the touchdown angle of the posterior (anterior) leg

is equal to the negative value of the liftoff value of the anterior (posterior) leg for the fixed point; i.e., $\gamma_a^{\text{td}} = -\gamma_p^{\text{lo}}$ and $\gamma_p^{\text{td}} = -\gamma_a^{\text{lo}}$. Focusing on the first three phases, it can be seen that

$$P_1(\bar{z}) := G_{\text{quad}} \circ F_{\text{sp}} \circ F_{\text{f}_1} \circ F_{\text{sa}}(\bar{z}) = \bar{z}. \tag{3.67}$$

Gaits that satisfy (3.67) are central to the following analysis for quadrupedal bounding in this work, the purpose of which is to exploit the symmetries of the underlying vector fields for analyzing stability in symmetric bounding motions.

3.3.2 Necessary Conditions for Stability of Bounding

We begin with Theorem 3 which establishes conditions under which P_1 is an involution:

$$(G_{\text{quad}} \circ F_{\text{sp}} \circ F_{\text{f}_1} \circ F_{\text{sa}}) \circ (G_{\text{quad}} \circ F_{\text{sp}} \circ F_{\text{f}_1} \circ F_{\text{sa}}) = \text{id}_{\Pi(\mathcal{S}_{\text{sa}})}. \tag{3.68}$$

Theorem 3. *For $z \in \Pi(\mathcal{S}_{\text{sa}})$, where $\mathcal{S}_{\text{sa}}$ is defined in (3.36), and let Π be the projection as per (3.17), if the posterior leg has its touchdown angle set according the following law*

$$\gamma_{\text{p}}^{\text{td}} = -\gamma_{\text{a}}^{\text{lo}} \ , \tag{3.69}$$

then P_1 is an involution on $\Pi(\mathcal{S}_{\text{sa}})$. Furthermore, if z is a fixed point of P shared by P_1, we have that $|\det(D_z P_1)(z))| = 1$.

The proof of Theorem 3 is organized in two lemmas.

Lemma 5. *On $\Pi(\mathcal{S}_{\text{sp}})$, $F_{\text{sa}} \circ G_{\text{quad}} \circ F_{\text{sp}} = G_{\text{quad}}$. Similarly, on $\Pi(\mathcal{S}_{\text{sa}})$, $F_{\text{sp}} \circ G_{\text{quad}} \circ F_{\text{sa}} = G_{\text{quad}}$.*

Proof. We focus on the first part of the Lemma, the second part can be proved by a similar argument. By inspecting the vector fields f_{sa} and f_{sp} it can be verified directly that $\hat{G}_{\text{quad}} \circ f_{\text{sp}} = -f_{\text{sa}} \circ \hat{G}_{\text{quad}}$, where $\hat{G}_{\text{quad}} = \text{diag}\ [-1, 1, -1, 1, -1, 1]$ and $\hat{G}_{\text{quad}} \cdot \hat{G}_{\text{quad}} = I_{6\times 6}$. Integrating from an initial condition $x_0 \in \mathcal{S}_{\text{sp}}$ results in

$$\hat{G}_{\text{quad}} \circ \hat{\phi}_{\text{sp}}^{t} = \hat{\phi}_{\text{sa}}^{-t} \circ \hat{G}_{\text{quad}} \ . \tag{3.70}$$

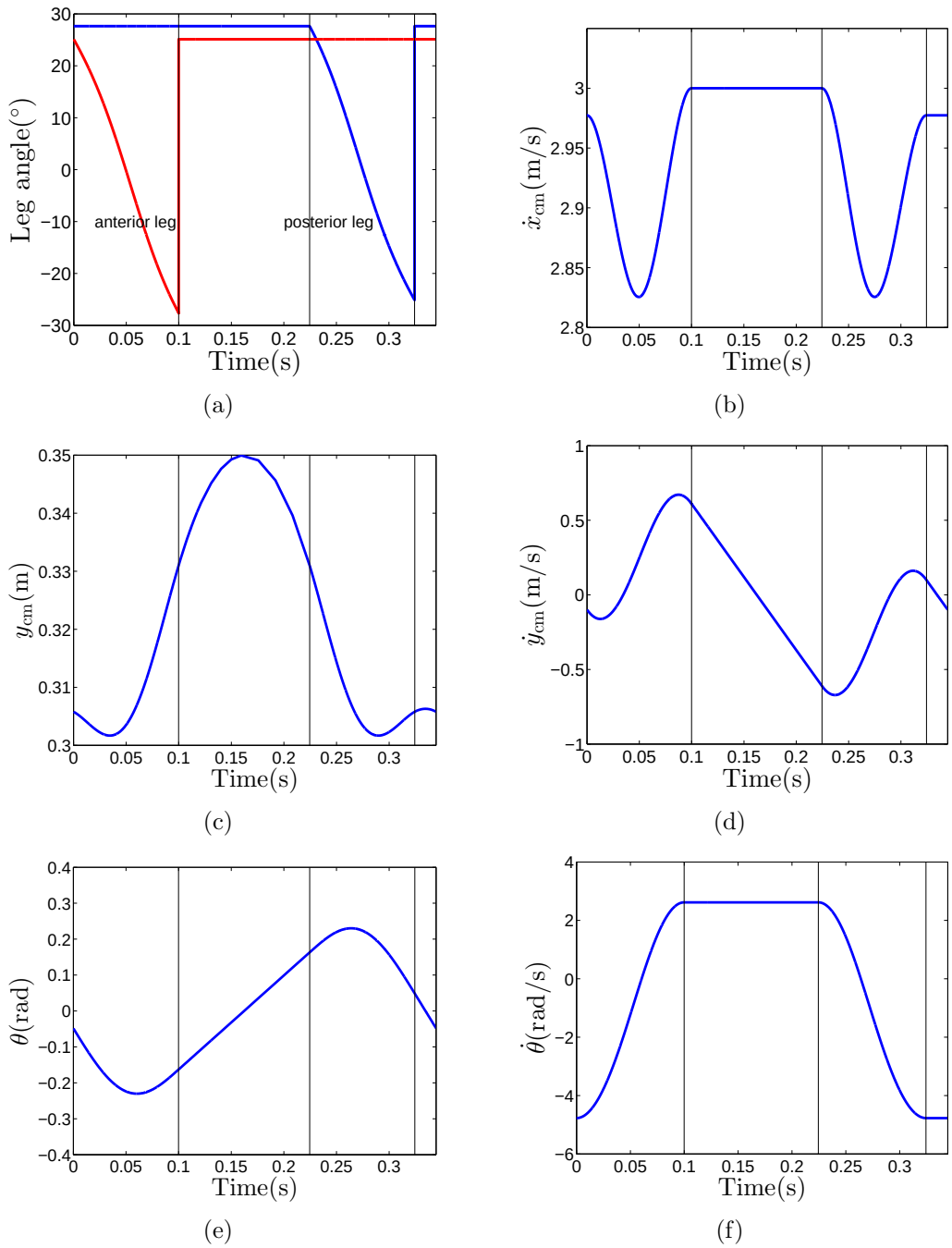

Figure 3.4: (a) Leg angle; (b)-(f) State evolution of a periodic bounding gait. Vertical lines represent events; from left to right: anterior leg liftoff, posterior leg touchdown, posterior leg liftoff.

Next we show that $T_{\text{sp}}(x_0) = T_{\text{sa}}(\hat{G}_{\text{quad}}(x_0))$. According to (3.70), $H_{\text{sp}\to\text{f}} \circ \hat{\phi}^t_{\text{sp}} = H_{\text{sp}\to\text{f}} \circ \hat{G}_{\text{quad}} \circ \hat{\phi}^{-t}_{\text{sa}} \circ \hat{G}_{\text{quad}}$.

Now, by the definitions (3.27) and (3.28) of the corresponding threshold functions observe that $H_{\text{sp}\to\text{f}} = H_{\text{sa}\to\text{f}} \circ \hat{G}_{\text{quad}}$. Then, $H_{\text{sp}\to\text{f}} \circ \hat{G}_{\text{quad}} \circ \hat{\phi}^{-t}_{\text{sa}} \circ \hat{G}_{\text{quad}} = H_{\text{sa}\to\text{f}} \circ \hat{\phi}^{-t}_{\text{sa}} \circ \hat{G}_{\text{quad}}$, and hence

$$H_{\text{sp}\to\text{f}} \circ \hat{\phi}^t_{\text{sp}} = H_{\text{sa}\to\text{f}} \circ \hat{\phi}^{-t}_{\text{sa}} \circ \hat{G}_{\text{quad}}. \tag{3.71}$$

This implies that the value of the threshold function $H_{\text{sp}\to\text{f}}$ along the flow $\hat{\phi}^t_{\text{sp}}(x_0)$ is equal to the value of $H_{\text{sa}\to\text{f}}$ along the time-reversed flow $\hat{\phi}^{-t}_{\text{sa}} \circ \hat{G}_{\text{quad}}(x_0)$. Since by (3.32) and (3.33), T_{sp} and T_{sa} represent the minimal solutions of the corresponding threshold equations being equal to zero, (3.71) implies $T_{\text{sp}}(x_0) = T_{\text{sa}}(\hat{G}_{\text{quad}}(x_0))$. As a result, (3.70) can be written in a flow map form. Applying the projection map Π (3.17) completes the proof. □

Remark 2. *Figure 3.5 provides some intuition on Lemma 5. Due to the fact the vector fields f_{sp} and f_{sa} of the stance-posterior and stance-anterior phases are related through $\hat{G}_{\text{quad}}$, the evolution of the stance-posterior phase starting from initial conditions $z_A = \Pi(x_A)$ and progressing forward in time is* indistinguishable *from the evolution of the stance-anterior phase starting from the corresponding G_{quad}-*reflected *initial conditions, $z_D = \Pi(\hat{G}_{\text{quad}}(x_A)) = G_{\text{quad}}(z_A)$, and progressing* backward *in time. Lemma 5 establishes that not only the flows, but also the flow maps of the two phases are G_{quad}-related because the corresponding threshold functions "preserve" the time reversal symmetry G_{quad}.*

Next we show that the flow map of the flight phase prior to the posterior-stance is G_{quad}-related with itself, provided that the touchdown angle of the posterior leg is selected according to a simple control law.

Lemma 6. *Let $\gamma^{\text{lo}}_{\text{a}}$ be the liftoff angle of the anterior leg. Define $\mathcal{S}_{\text{f}} := \{x \in \mathcal{X} \mid H_{\text{sa}\to\text{f}}(x) = 0, \dot{y}_{\text{cm}} > 0\}$ and let $\Pi(\mathcal{S}_{\text{f}})$ be the projection as per (3.17). If the touchdown angle of posterior leg is selected according to the rule $\gamma^{\text{td}}_{\text{p}} = -\gamma^{\text{lo}}_{\text{a}}$ then $F_{\text{f}_1} \circ G_{\text{quad}} \circ F_{\text{f}_1} = G_{\text{quad}}$ for initial state $z_0 \in \Pi(\mathcal{S}_{\text{f}})$.*

Proof. (sketch) The condition $\gamma_{\mathrm{p}}^{\mathrm{td}} = -\gamma_{\mathrm{a}}^{\mathrm{lo}}$ guarantees that the time-to-switch functions for the two phases satisfy $T_{\mathrm{f}}(x_0) = T_{\mathrm{f}}(\hat{G}_{\mathrm{quad}}(x_0))$. The arguments are identical to those in the proof of Lemma 5 and are omitted for brevity. □

The proof of Theorem 3 is provided next.

Proof of Theorem 3. The first part of the theorem proof is an immediate result of the Lemmas 5 and 6. The second part is a result of Theorem 1 under condition (3.67). □

With Theorem 3 in hand, we can now state necessary conditions for the stability of periodic bounding gait. The determinant of the Poincaré map at a fixed point $\bar{z}$ realized under the touchdown angle control policy suggested by Theorem 3 is

$$|\det(D_z P(\bar{z}))| = |\det(D_z P_2(P_1(\bar{z})) \cdot D_z P_1(\bar{z}))| = |\det(D_z P_2(\bar{z}))| = |\det(D_z F_{\mathrm{f}_2}(\bar{z}))|.$$

As stated in (2.4), a necessary condition for $\bar{z}$ to be a stable fixed point of P is $|\det(D_z F_{\mathrm{f}_2}(\bar{z}))| < 1$. Otherwise, the Poincaré return map would have at least one eigenvalue which is bigger than one. Note that F_{f_2} is the flow map of the flight following the posterior stance and that the corresponding touchdown angle has not been fixed by the procedure, thus it is available for control.

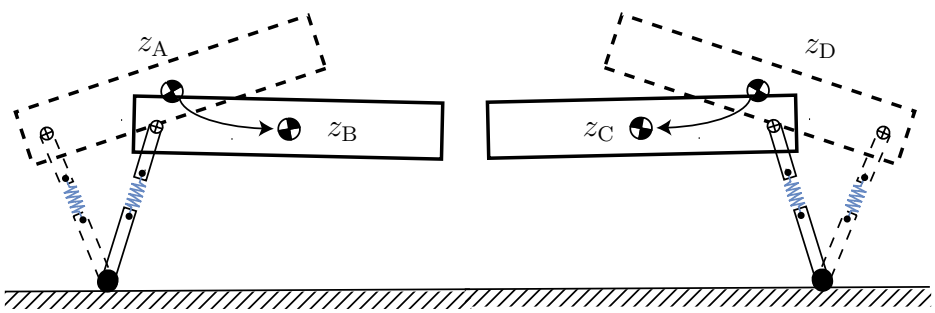

Figure 3.5: The stance-posterior and stance-anterior phases are related through a time-reversal symmetry.

Given an initial condition $z_0 = \Pi(x_0)$, the fight phase flow map F_{f_2} can be computed analytically due to the integrability of the underlying vector field f_{f}; i.e.,

$$F_{\mathrm{f}_2}(z_0) = \begin{pmatrix} y_{\mathrm{cm},0} + \dot{y}_{\mathrm{cm},0} T_{\mathrm{f}} - \frac{1}{2} g T_{\mathrm{f}}^2 \\ \theta_0 + \dot{\theta}_0 T_{\mathrm{f}} \\ \dot{x}_{\mathrm{cm},0} \\ \dot{y}_{\mathrm{cm},0} - g T_{\mathrm{f}} \\ \dot{\theta}_0 \end{pmatrix} \tag{3.72}$$

where[4] $T_{\mathrm{f}} = T_{\mathrm{f}}(z_0, \gamma_{\mathrm{a}})$ is an implicit function of initial state and front leg angle, which will be determined by a state feedback law of the form $\gamma_{\mathrm{a}}(z_0)$. T_{f} is described by zeroing the threshold equation $H_{\mathrm{f}\to\mathrm{sa}}$:

$$y_{\mathrm{cm}} + \dot{y}_{\mathrm{cm}} T_{\mathrm{f}} - \frac{g T_{\mathrm{f}}^2}{2} + L \sin(\theta_0 + \dot{\theta} T_{\mathrm{f}}) - l_0 \cos \gamma_{\mathrm{a}}^{\mathrm{td}} = 0 \tag{3.73}$$

The determinant of $D_z F_{\mathrm{f}_2}(z_0)$ can be computed by

$$\det(D_z F_{\mathrm{f}_2}) = 1 - g \frac{\partial T_{\mathrm{f}}}{\partial \dot{y}_{\mathrm{cm},0}} + \dot{y}_{\mathrm{cm},0} \frac{\partial T_{\mathrm{f}}}{\partial y_{\mathrm{cm},0}} + \dot{\theta}_0 \frac{\partial T_{\mathrm{f}}}{\partial \theta_0} \tag{3.74}$$

The partial derivative of T_{f} in the determinant can be replaced using implicit differentiation rules on (3.73). After some manipulation, $D_z F_{\mathrm{f}2}(z_0)$ can be written as

$$\det(D_z F_{\mathrm{f}_2}(z_0)) = \frac{\Delta_1}{-\Delta_2} \ , \tag{3.75}$$

where

$$\Delta_1 = \sin \gamma_{\mathrm{a}}^{\mathrm{td}} l_0 \left(\dot{y}_{\mathrm{cm},0} \frac{\partial \gamma_{\mathrm{a}}^{\mathrm{td}}}{\partial y_{\mathrm{cm},0}} + \dot{\theta}_0 \frac{\partial \gamma_{\mathrm{a}}^{\mathrm{td}}}{\partial \theta_0} - g \frac{\partial \gamma_{\mathrm{a}}^{\mathrm{td}}}{\partial \dot{y}_{\mathrm{cm},0}} \right)$$

$$\Delta_2 = \dot{y}_{\mathrm{cm},0} - g T_{\mathrm{f}} + \dot{\theta}_0 L \cos(\theta_0 + \dot{\theta}_0 T_{\mathrm{f}})$$

See Appdendix A for the detailed derivation.

[4] Note that by (3.30), $H_{\mathrm{f}\to\mathrm{sa}}$ does not depend on x_{cm}, thus T_{f} is essentially a function of z.

3.4 Numerical Simulation

3.4.1 Evaluation for ASLIP Model

Figure 3.6 (a)-(c) presents the stride-one and stride-two fixed points for the ASLIP model in the y_{cm}-$\dot{y}_{\text{cm}}$ plane at the Poincaré section (the beginning of stance) for three different running velocities. The red and black lines in the figures are unstable and stable stride-one fixed points under a constant touchdown angle controller and torso controller (3.62). Notice that no self-stable stride-one fixed points are found for 2m/s. Meanwhile, the blue dots represent stride-two fixed points under (3.62) and (3.41), and as proved by Theorem 4, they are all stable. Moreover, there is more area in y_{cm}-$\dot{y}_{\text{cm}}$ plane which allows stride-two fixed points.

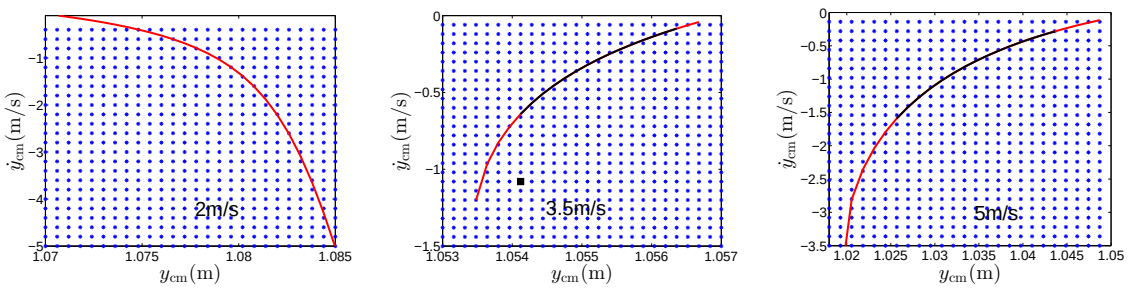

(a) (b) (c)

Figure 3.6: Stride-one and Stride-two fixed points for ASLIP. The black line includes stable stride-one fixed points, where the red line includes unstable stride-one fixed points. The blue points i stride-two fixed points under (3.62) and (3.41). All the stride-two fixed points are neutral stable in Lyapunov sense.

Figure 3.7 illustrates how the ASLIP model converges to the zero dynamics manifold under torso controller (3.62). The torso starts from a initial condition with $\dot{\theta} \neq 0$. The controller driven the torso back to the zero dynamics manifold in finite time.

To examine if the stride-two gaits can negotiate disturbances in the form of unexpected ground height variations and energy changes, we test one of the stride-two fixed points, the point marked by a black square dot in Fig 3.6(b). The ground

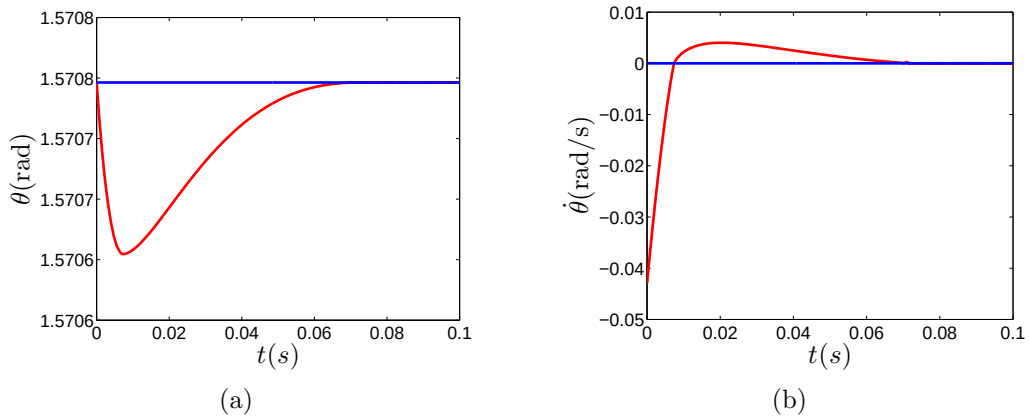

(a) (b)

Figure 3.7: The converge of ASLIP to the zero-dynamcis manifold under (3.62).

is modeled as a 200m trail, composed by 0.2m-wide flat surfaces of different height. The height of each surface is a uniform distributed random variable within [-0.1,0], described by the following equation:

$$y_{\text{gnd}} = -0.1 + 0.1 \text{ rand} \ . \tag{3.76}$$

To provide enough toe clearance, the leg length is set to 80% of the rest length after liftoff and extended to full length after apex. 100 simulation runs are carried out and all the tests are success, i.e., the model can run to the end of the 200m noisy trail. Figure 3.8 presents the ground height profile of a portion of the random trail, and the corresponding COM velocity at Poincaré section.

3.4.2 Analysis of Bounding Under A Leg Control Law

In this section, we analyze the stability of bounding under a control law, which is discussed next. Based on our previous analysis, we set

$$\gamma_{\text{p}}^{\text{td}}[n] = -\gamma_{\text{a}}^{\text{lo}}[n] \ , \tag{3.77}$$

and we employ the following feedback controller to regulate the touchdown angle of the anterior leg

$$\gamma_{\text{a}}^{\text{td}}[n] = \bar{\gamma}_{\text{a}}^{\text{td}} + c(\bar{\gamma}_{\text{p}}^{\text{lo}} - \gamma_{\text{p}}^{\text{lo}}[n]) \tag{3.78}$$

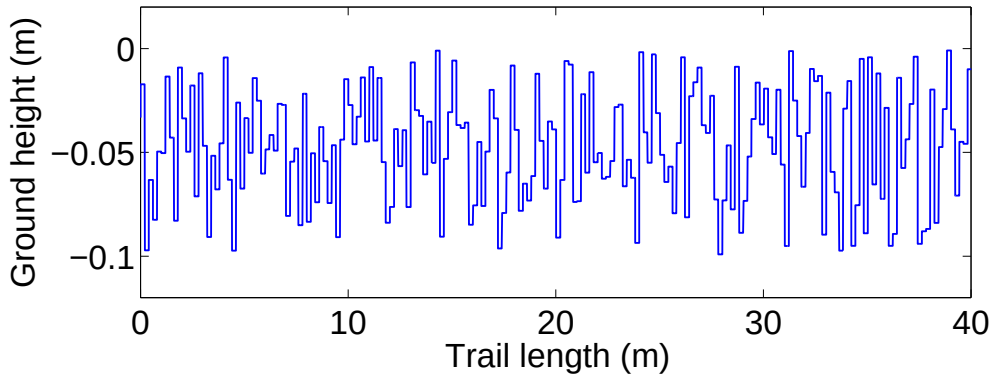

(a)

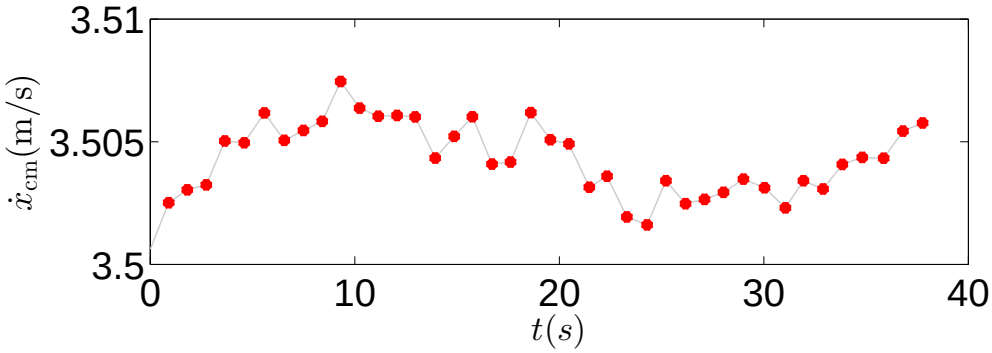

(b)

Figure 3.8: The response of one stride-two gait of ASLIP under $\bar{\gamma}$ to ground variation. (a) One set of the ground profile. (b) The horizontal COM velocity.

where $\bar{\gamma}_{\mathrm{a}}^{\mathrm{td}}$ and $\bar{\gamma}_{\mathrm{p}}^{\mathrm{lo}}$ are the anterior leg touchdown and the posterior leg liftoff angles at a fixed point; c is a constant gain, and $\gamma_{\mathrm{p}}^{\mathrm{lo}}$ is the posterior leg's liftoff angle.

Noticing that $\gamma_{\mathrm{p}}^{\mathrm{lo}} = -\mathrm{acos}(\frac{y_{\mathrm{cm},0}-L\sin\theta_0}{l_0})$ and using $\gamma_p^{\mathrm{td}} = -\gamma_a^{\mathrm{lo}}$ at a symmetric fixed point $\bar{z}_0$, the determinant of the Jacobian of the Poincaré return map at fixed point $\bar{z}$ is

$$|\det(D_z\mathcal{P}(\bar{z}))| = |\det(D_zF_{\mathrm{f}_2}(\bar{z}))| = |c|. \tag{3.79}$$

See Appdendix A for the detailed derivation. As a result, a necessary condition for the system to be stable is $c \in [-1, 1]$.

Figure 3.9 shows the discrete evolution of the system in closed loop with the controller (3.77)-(3.78) under a perturbation away from the fixed point of Fig. 3.4. The

perturbation does not change the total energy of the system. Three different values of c are considered. Although, (3.79) is necessary but not sufficient for stability, it can be seen that for $c < 1$ the system converges to a fixed point. For $c = 1$ the evolution oscillates around the fixed point while it diverges for $c > 1$. Finally, to fully characterize stability, Fig. 3.10 presents the root locus of the eigenvalues of the linearization of the Poincaré map for different values of c at the fixed point. It can be seen that for $|c| > 1$ the system is indeed unstable.

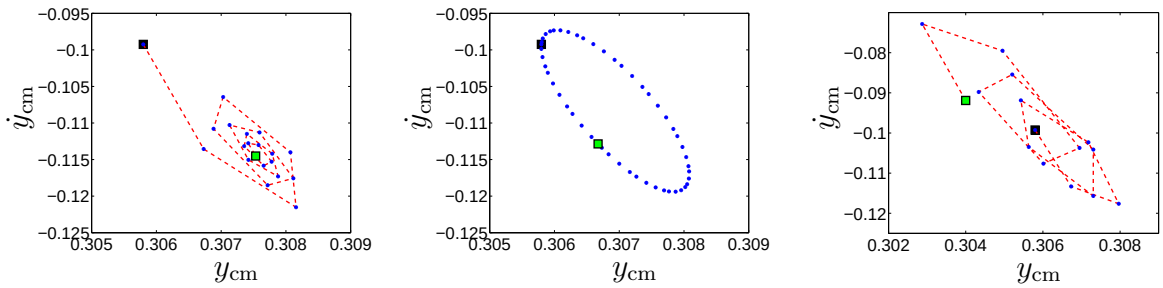

(a) (b) (c)

Figure 3.9: Discrete evolution of the closed loop system (blue dots) under a perturbation that leaves the system's total energy unchanged. The initial state is marked by the black square while the final condition is marked as green square. 3.9(a): $c = 0.5$; 3.9(b): $c = 1$; and 3.9(c): $c = 1.2$.

3.5 Conclusion and Discussion

This chapter analyzed the stability of running gaits using the method of the Poincaré return map. Rather than treating the nonintegrable maps as *a black box* and resorting to numerical methods, we factor the Poincaré return map based on symmetries and offer analytically expressed conclusions on stability. Two reduced-order templates with non-trivial torso moment of inertia, one for monopedal hopping and one for quadrupedal bounding, were studied. For the ASLIP model, the analysis provides a synthesized controller with analytically tractable stability properties. The controller is composed of a torso controller and a symmetry leg placement controller. It is shown analytically that every point on the manifold $\mathcal{Z}$ with upright torso angle which can lead to a gait is a periodic gait and they are all stable in Lyapunov sense.

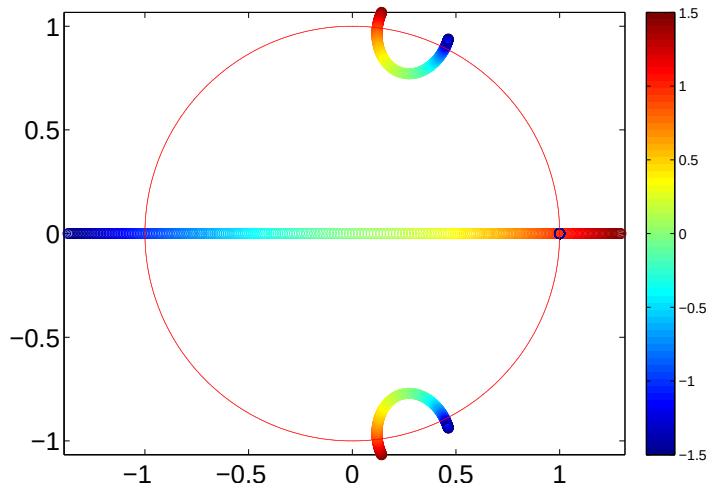

Figure 3.10: Locus of the eigenvalues as c varies in $[-1.5, 1.5]$.

For the quadrupedal bounding, the approach offers analytically expressed necessary conditions for stability. Inspired by this analysis, a simple touchdown angle policy is devised with its control gains selected so that the necessary condition for stability is satisfied. Numerical simulation demonstrates the performance of controllers for the two models in case of ground height variation and state perturbation.

Chapter 4

ACTIVE COMPLIANCE HYBRID ZERO DYNAMICS CONTROL OF BOUNDING ON HYQ

In this chapter, an elaborate model with segmented legs is employed to study quadrupedal bounding, the morphology of which resembles that of HyQ. In contrast to the reduced-order template models analyzed in the previous chapter, this model has nontrivial leg mass. As a result, the model is no longer energy conservative due to the inelastic impact between the toe and the ground. In addition, this model has *no passive compliant elements* because HyQ features no spring. In light of the role of compliance in running, this chapter proposes a bounding controller which incorporates *active compliant elements* into the Hybrid Zero Dynamics framework to realize stable periodic bounding gaits. Exploiting the hybrid nature of the system, the control action is developed in both continuous and discrete time to regulate the torque applied at the support leg and the motion of the swing leg. The performance of the controller is evaluated by numerical simulations. Part of this chapter has appeared in [55].

This chapter is organized as follows. Section 4.1 develops a saggital-plane bounding model of HyQ. Section 4.2 gives a detailed account on the controller design. Section 4.3 evaluates the controller in simulation and Section 4.4 concludes the chapter.

4.1 Modeling Bounding of HyQ

Figure 4.1(a) presents the **Hy**draulically actuated **Q**uadruped HyQ. HyQ is a fully torque-controlled robot built by the Dynamic Legged Systems Lab of the Istituto Italiano di Tecnologia (IIT) [90]. The robot weighs about 86kg in its current configuration and has a height of 1m with fully extended legs. Each leg has three hydraulic joints: two in the hip (abduction/adduction (HAA) and flexion/extension (HFE)) and

one in the knee (flexion/extension (KFE)). High-performance servovalves enable joint-level torque and position control with excellent tracking performance [8]. The high power-density of hydraulic actuators allow strong and fast leg motions. The robustness of hydraulic actuation against impact also makes HyQ a very suitable platform for dynamic gaits, such as trotting and bounding.

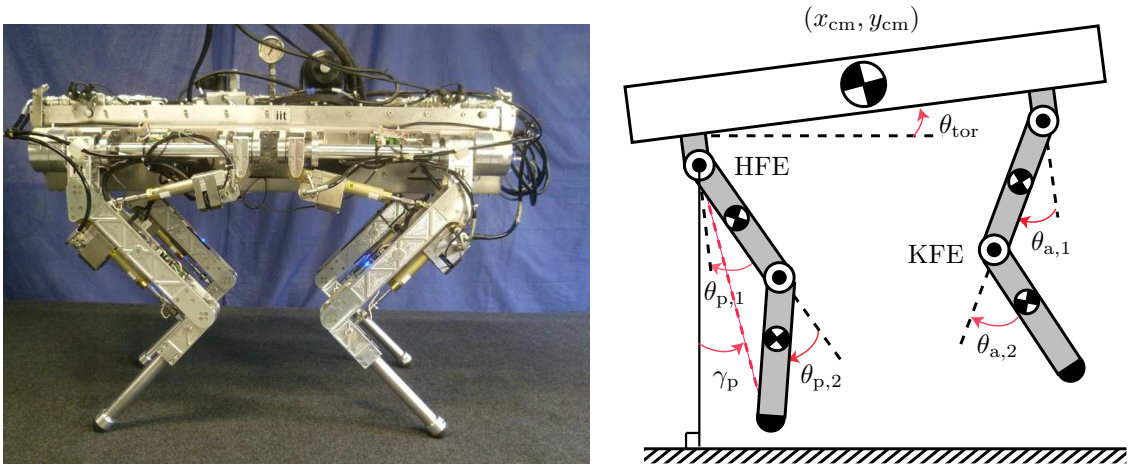

(a) (b)

Figure 4.1: (a) The Hydraulically Actuated Quadruped (HyQ). HyQ is developed by the Dynamic Legged Systems Lab of the Istituto Italiano di Tecnologia (IIT). It features three degrees of freedom per leg, two in the hip abduction/adduction and flexion/extension joints and one in the knee flexion/extension joint. (b) A sagittal plane model of HyQ used for controller design.

4.1.1 Modeling Assumption

In modeling bounding with HyQ, it is assumed that the essential features of bounding motion take place in the sagittal plane, resulting in the planar model of Fig. 4.1(b). As a result, the hip abduction-adduction degrees of freedom are not considered in the model. In Fig. 4.1(b), the back and front virtual legs represent the collective effect of the back and front physical leg pairs, respectively. The geometric and inertia parameters of the model can be found in Table 4.1.

Table 4.1: Mechanical Parameters of the Model

Parameter	**Value**	**Units**
Torso mass (including HAA joints) (M)	72.00	kg
Upper leg mass (virtual leg) (M_1)	5.30	kg
Lower leg mass (virtual leg) (M_2)	1.60	kg
Total Mass (M_{total})	85.80	kg
Torso Inertia (including HAA joints) ($J0$)	6.98	kg m^2
Upper leg inertia ($J1$)	0.05	kg m^2
Lower leg inertia ($J2$)	0.02	kg m^2
Hip-to-Hip distance ($2 \times L$)	0.74	m
HAA linkage length (L_0)	0.12	m
Upper leg linkage length (L_1)	0.35	m
Lower leg linkage length (L_2)	0.33	m
Upper leg COM to hip distance ($L_{\text{m},1}$)	0.162	m
Lower leg COM to knee distance ($L_{\text{m},2}$)	0.122	m

Depending on the contact between the foot with the ground, the model can be in one of the following phases: flight "f," anterior stance "sa," posterior stance "sp," and *double stance* "sd". Figure 4.2 shows the phase sequence of a *nominal* bounding gait, which does not include a double stance phase; Note, however, that while converging from a perturbation the model can go through double stance phases. The indices "sw" and "su" refer to the swing leg and the support leg respectively. Furthermore, quantities related to the hip and knee joints, such as torques and angles, will be denoted by "1" and "2," respectively.

4.1.2 Dynamics in Floating-base Form

As defined in Fig. 4.1(b), a convenient choice of generalized coordinates describing the model's configuration is $q := (x_{\text{cm}}, y_{\text{cm}}, \theta_{\text{tor}}, \theta_{\text{p},1}, \theta_{\text{p},2}, \theta_{\text{a},1}, \theta_{\text{a},2})'$, where $(x_{\text{cm}}, y_{\text{cm}})$ correspond to the Cartesian position of the torso's center of mass (COM), θ_{tor} is the pitch angle of the torso with respect to the horizontal, $(\theta_{\text{p},1}, \theta_{\text{a},1})$ are the hip angles of

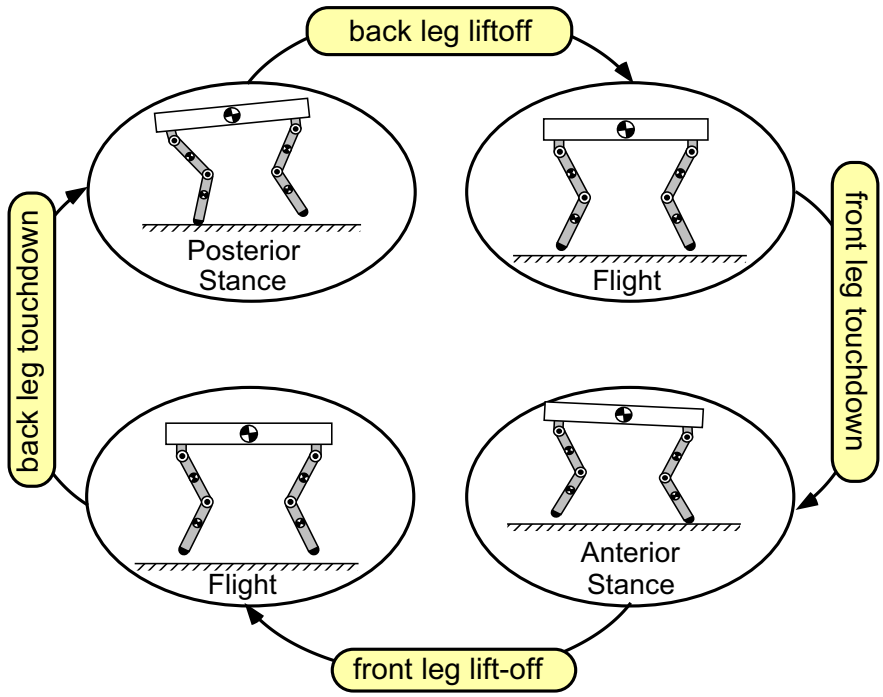

Figure 4.2: Phase transition of a nominal bounding gait.

the posterior and anterior legs, and $(\theta_{\mathrm{p},2}, \theta_{\mathrm{a},2})$ are the knee angles of the posterior and anterior legs. The dynamics can be written in the form

$$D(q)\ddot{q} + C(q,\dot{q})\dot{q} + G(q) = Bu + J^T F_{\mathrm{ext}}, \tag{4.1}$$

where D is the mass matrix, C contains Coriolis and centrifugal terms, G is the vector of gravity-dependent forces, and B is the matrix mapping the input vector $u := (u_{\mathrm{p},1}, u_{\mathrm{p},2}, u_{\mathrm{a},1}, u_{\mathrm{a},2})'$ to the vector of generalized forces. In (4.1), $J := (J^{x\prime}, J^{y\prime})'$ is the contact Jacobian obtained by differentiating the position of the foot with respect to an inertia frame, while $F_{\mathrm{ext}} = (F^x_{\mathrm{ext}}, F^y_{\mathrm{ext}})'$ is the interaction force, which is zero when the leg/toe is in flight and not in contact with the ground.

The contact between the toe and the ground is modeled based on a Coulomb friction model, resulting in

$$J^y\ddot{q} + \dot{J}^y\dot{q} = 0 \tag{4.2}$$

$$J^x \ddot{q} + \dot{J}^x \dot{q} = 0 \quad \text{or} \quad F^x_{\text{ext}} = \mu F^y_{\text{ext}} \tag{4.3}$$

that are augmented to (4.1) to solve for $\ddot{q}$ and F_{ext}; in (4.3), μ is the sliding friction coefficient assumed to be 0.8. Depending on whether sliding occurs, either constraint in (4.3) is used.

4.1.3 Reduced Dynamics

In the anterior and posterior stance phases, and under the assumption that the toe does not slide over the ground, the equations of motion can be written as:

$$D_i(q_{\text{s}})\ddot{q}_{\text{s}} + C_i(q_{\text{s}}, \dot{q}_{\text{s}})\dot{q}_{\text{s}} + G_i(q_{\text{s}}) = B_i u \ , \tag{4.4}$$

for $i \in \{\text{sa}, \text{sp}\}$, where the configuration variables are $q_{\text{s}} := (\theta_{\text{tor}}, \theta_{\text{p},1}, \theta_{\text{p},2}, \theta_{\text{a},1}, \theta_{\text{a},2})'$. Notice that q_{s} does not include x_{cm} and y_{cm} of q.

4.1.4 Transitions

For bounding gaits, transitions among phases are triggered at the instance of touchdown (TD) or liftoff (LO) events.

Flight-to-stance Transition

Switching from flight to the anterior or posterior stance, or from the anterior or posterior stance to double stance, occurs at TD, which is modeled as a instantaneous inelastic impact that results in no rebound using to the assumptions listed in [102, Section 3.4]. Note that the resulting impact maps leave the configuration variables unaffected, while the corresponding velocities experience jumps.

Stance-to-flight Transition

The robot enters the flight phase when the support leg takes off. This event is characterized by the zeroing of the normal component of the ground reaction force. With the knee and hip joints actively controlled, the liftoff event can be initiated by actively flexing the joints. Hence, we will assume that the legs take off when the

corresponding knee joint angle is $\pm 40°$, where "+" refers to the posterior and "−" to the anterior leg.

4.2 Controller Design

The proposed controller—see Fig. 4.3 for an overview of the control action—is largely inspired by the study of passive bounding models in Chapter 3. By commanding appropriate leg touchdown angles at flight phases, and keeping the leg passive during the stance phases, self-stable periodic bounding gaits can be generated by low-dimension models with mass-less springy legs [71]. HyQ, however, is neither energy-conservative nor has any spring in it. Hence, to "mimic" the behavior of the passive model, the joints of the support leg are torque-controlled to create a virtual spring while the joints of the swing leg are motion controlled to imposes (virtual) holonomic constraints to land the robot with a preferred touchdown configuration. Utilizing the hybrid nature of the system, the introduce parameters are updated in a discrete time to render the constraints impact-invariant, leading to the notion of hybrid zero dynamics.

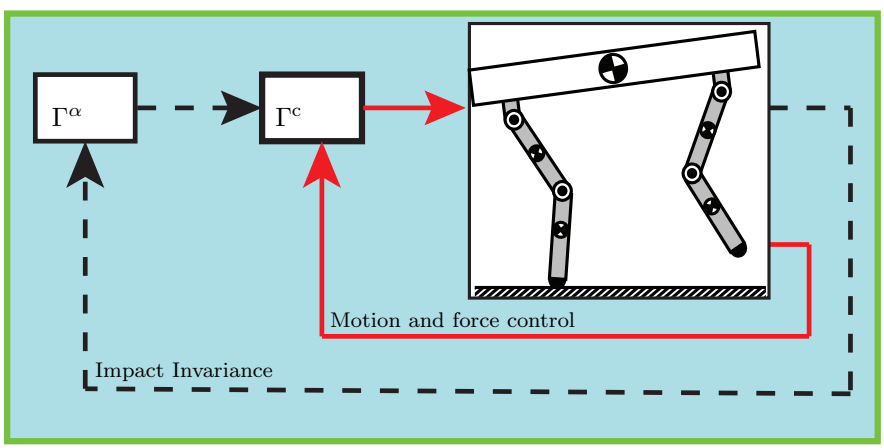

Figure 4.3: Feedback diagram illustrating the structure of the controller. The continuous line represents signals in continuous time; the dashed lines represent signals in discrete time. The continuous-time controller Γ^{c} creates an actively compliant zero dynamics using torque planning and motion control. The discrete-time controller Γ^{α} updates parameters to ensure invariance under the transition maps.

4.2.1 Stance Phase Torque Planning and Motion Control

The stance phase dynamics (4.4) can be written without interaction force as

$$\dot{x}_{\mathrm{s}} = f_i(x_{\mathrm{s}}) + g_i^{\mathrm{su}}(x_{\mathrm{s}})u_i^{\mathrm{su}} + g_i^{\mathrm{sw}}(x_{\mathrm{s}})u_i^{\mathrm{sw}}, \tag{4.5}$$

where $i \in \{\mathrm{sa}, \mathrm{sp}\}$ and $x_{\mathrm{s}} := (q_{\mathrm{s}}', \dot{q}_{\mathrm{s}}')'$ is the state vector. g_i^{su} and g_i^{sw} describe the influence of the support and swing leg torques u_i^{su} and u_i^{sw}, respectively. More explicitly, $u_{\mathrm{sp}}^{\mathrm{su}} = (u_{\mathrm{p},1}, u_{\mathrm{p},2})'$ and $u_{\mathrm{sp}}^{\mathrm{sw}} = (u_{\mathrm{a},1}, u_{\mathrm{a},2})'$ in stance-posterior and $u_{\mathrm{sa}}^{\mathrm{su}} = (u_{\mathrm{a},1}, u_{\mathrm{a},2})'$ and $u_{\mathrm{sa}}^{\mathrm{sw}} = (u_{\mathrm{p},1}, u_{\mathrm{p},2})'$ in stance-anterior.

The purpose of the controller at stance phases (sa or sp) is to "create" active compliant elements to (indirectly) control the interaction between the support leg and the ground, and to place the swing leg at a desired configuration. To achieve these objectives, a combination of torque planning and motion control is employed.

Active Compliance through Torque Planning for the Support Leg

To regulate the interaction between the torso and the environment, the controller commands desired torque profiles at the hip and knee joints of the leg in contact with the ground. In more detail, a constant torque β_i, $i \in \{\mathrm{sp}, \mathrm{sa}\}$ is commanded at the hip actuator of the support leg as

$$u_{\mathrm{p},1} = \beta_{\mathrm{sp}} \text{ and } u_{\mathrm{a},1} = \beta_{\mathrm{sa}} \tag{4.6}$$

for the stance-posterior and the stance-anterior phase. Next, the following torque is commanded at the knee joint

$$u_{\mathrm{p},2} = \bar{u}_{\mathrm{p},2} + k_{\mathrm{p}}(\theta_{\mathrm{p},2} - \bar{\theta}_{\mathrm{p},2}) \tag{4.7}$$

for the stance-posterior phase, and similarly

$$u_{\mathrm{a},2} = \bar{u}_{\mathrm{a},2} + k_{\mathrm{a}}(\theta_{\mathrm{a},2} - \bar{\theta}_{\mathrm{a},2}) \tag{4.8}$$

for the stance-anterior phase. In (4.7), k_{p} and $\bar{\theta}_{\mathrm{p},2}$ are the stiffness and the rest angle of the virtual knee spring for the posterior leg in the posterior-stance phase; similarly,

k_{a} and $\bar{\theta}_{\mathrm{a},2}$ in (4.8) are the corresponding constants for the anterior leg virtual spring in the anterior-stance phase. We require $\bar{\theta}_{\mathrm{p},2} = -\bar{\theta}_{\mathrm{a},2} = 40°$, consistent with the liftoff conditions in 4.1.4 so that the (virtual) spring is completely undeformed at liftoff. Note that the offsets $\bar{u}_{\mathrm{p},2}$ and $\bar{u}_{\mathrm{a},2}$ in (4.7) and (4.8), are added to ensure that the normal component of the ground reaction force is sufficiently large to prevent toe slipping.

To summarize, for each $i \in \{\mathrm{sp}, \mathrm{sa}\}$, the commanded torque profiles for the support leg during the stance-posterior and stance-anterior phases, can be written in the form

$$u_i^{\mathrm{su}} = \Gamma_i^{\mathrm{su}}(x_i, \alpha_i^{\mathrm{su}}) \tag{4.9}$$

for $i \in \{\mathrm{sp}, \mathrm{sa}\}$, where $\alpha_{\mathrm{sp}}^{\mathrm{su}} := \{\bar{u}_{\mathrm{p},2}, k_{\mathrm{p}}, \beta_{\mathrm{sp}}\}$ and $\alpha_{\mathrm{sa}}^{\mathrm{su}} := \{\bar{u}_{\mathrm{a},2}, k_{\mathrm{a}}, \beta_{\mathrm{sa}}\}$. With this notation, the stance dynamics (4.5) for $i \in \{\mathrm{sp}, \mathrm{sa}\}$ in closed loop with the controller of the corresponding support leg (4.9) becomes

$$\dot{x}_i = f_i^{\mathrm{sw}}(x_i, \alpha_i^{\mathrm{su}}) + g_i^{\mathrm{sw}}(x_i) u_i^{\mathrm{sw}}, \tag{4.10}$$

where $f_i^{\mathrm{sw}}(x_i, \alpha_i^{\mathrm{su}}) := f_i(x_i) + g_i^{\mathrm{su}}(x_i)\Gamma_i^{\mathrm{su}}(x_i, \alpha_i^{\mathrm{su}})$. Note that if a double stance phase occurs while converging from a perturbation, both legs are support legs and are torque controlled using the controller described here.

Swing Leg Motion Control

The continuous-time control input u^{sw} in (4.10) includes the hip and knee joint torques of the swing leg, and it will be used to prepare the swing leg for its ensuing touchdown. To achieve this objective, we associate to (4.10) the output

$$y_i = h_i(q_{\mathrm{s}}, \alpha_i^{\mathrm{sw}}) := H_i q_{\mathrm{s}} - h_i^{\mathrm{d}}(s_i(q_{\mathrm{s}}), \alpha_i^{\mathrm{sw}}) \tag{4.11}$$

for $i \in \{\mathrm{sp}, \mathrm{sa}\}$, where $H_i q_{\mathrm{s}}$ is the vector of the controlled variables, which contains the absolute hip angle and the knee angle relative to the upper part of the swing leg; i.e.,

$$H_{\mathrm{sp}} := \begin{bmatrix} 1 & -1 & 0 & 0 & 0 \\ 0 & 0 & 1 & 0 & 0 \end{bmatrix} \text{ and } H_{\mathrm{sa}} := \begin{bmatrix} 1 & 0 & 0 & -1 & 0 \\ 0 & 0 & 0 & 0 & 1 \end{bmatrix} \tag{4.12}$$

for the stance-posterior and the stance-anterior phases.

In (4.11), h_i^{d} is the desired evolution of the controlled variables, which is represented by smooth polynomials as detailed in Appendix B. We only mention here that the polynomials are parameterized by the normalized variables

$$s_{\mathrm{sp}}(q_{\mathrm{sp}}) := \frac{\gamma_{\mathrm{p}}(q_{\mathrm{sp}}) - \gamma_{\mathrm{p}}^{\mathrm{td}}}{\Delta_{\mathrm{sp}}} \quad \text{and} \quad s_{\mathrm{sa}}(q_{\mathrm{sa}}) := \frac{\gamma_{\mathrm{a}}(q_{\mathrm{sa}}) - \gamma_{\mathrm{a}}^{\mathrm{td}}}{\Delta_{\mathrm{sa}}} \tag{4.13}$$

where Δ_{sp} and Δ_{sa} are constants, γ_{p} and γ_{a} are the angles between the vertical and the line connecting the hip with the foot of the posterior and anterior leg, respectively, and $\gamma_{\mathrm{p}}^{\mathrm{td}}$, $\gamma_{\mathrm{a}}^{\mathrm{td}}$ are the corresponding values at touchdown; see Fig. 4.1(b). Note that, for each $i \in \{\mathrm{sp}, \mathrm{sa}\}$, s_i is a monotonic function of the configuration variables, essentially replacing time in the parameterization of the polynomials described in the Appendix B. Finally, all the parameters associated with the design of the desired evolution h_i^{d} of the controlled variables, are collected in the array α_i^{sw}, which, participates in the definition of the constraint (4.11).

The outputs (4.11) are functions of the configuration variables only; hence, they can be interpreted as holonomic constraints, which can be imposed (asymptotically) on the system by driving (4.11) to zero. To do so, we differentiate (4.11) for given values of $\alpha_i := \{\alpha_i^{\mathrm{su}}, \alpha_i^{\mathrm{sw}}\}$ to get[1]

$$\frac{d^2 y_i}{dt^2} = L_{f_i^{\mathrm{sw}}}^2 h_i(x_i, \alpha_i) + L_{g_i^{\mathrm{sw}}} L_{f_i^{\mathrm{sw}}} h_i(x_i, \alpha_i) u^{\mathrm{sw}} \tag{4.14}$$

where $L_{g_i^{\mathrm{sw}}} L_{f_i^{\mathrm{sw}}} h_i(x_i, \alpha_i)$ is the decoupling matrix. Upon verifying the invertibility of $L_{g_i^{\mathrm{sw}}} L_{f_i^{\mathrm{sw}}} h_i(x_i, \alpha_i)$,

$$u_*^{\mathrm{sw}}(x_i, \alpha_i) := -\left(L_{g_i^{\mathrm{sw}}} L_{f_i^{\mathrm{sw}}} h_i(x_i, \alpha_i)\right)^{-1} L_{f_i^{\mathrm{sw}}}^2 h_i(x_i, \alpha_i) \tag{4.15}$$

is the unique control input which renders the surface

$$\mathcal{Z}_{\alpha_i} := \left\{x_i \in \mathcal{X}_i \mid h_i(q_i, \alpha_i^{\mathrm{sw}}) = 0,\ L_{f_i^{\mathrm{sw}}} h_i(x_i, \alpha_i) = 0\right\} \tag{4.16}$$

[1] Note that the output (4.11) depends only on α_i^{sw}; however, when we differentiate along the dynamics (4.10) the resulting Lie derivatives depend also on the parameters α_i^{su} introduced by the force controller.

invariant under the flow of the closed-loop dynamics. Zeroing the output effectively reduces the dimension of the system by restricting its dynamics on the zero dynamics surface $\mathcal{Z}_{\alpha_i}$. The dynamics of the system restricted on $\mathcal{Z}_{\alpha_i}$,

$$\dot{z} = f_i^*|_{\mathcal{Z}_{\alpha_i}}(z) \tag{4.17}$$

is the corresponding zero dynamics. To ensure attractivity of $\mathcal{Z}_{\alpha_i}$, the input (4.15) is modified as

$$u^{\mathrm{sw}} = \Gamma_i^{\mathrm{sw}}(x_i, \alpha_i) = \left(L_{g_i^{\mathrm{sw}}} L_{f_i^{\mathrm{sw}}} h_i(x_i, \alpha_i)\right)^{-1} \left[\upsilon(y_i, \dot{y}_i, \epsilon) - L_{g_i^{\mathrm{sw}}} L_{f_i^{\mathrm{sw}}} h_i(x_i, \alpha_i)\right] \tag{4.18}$$

where

$$\upsilon(y_i, \dot{y}_i, \epsilon) := -\frac{1}{\epsilon^2} K_{\mathrm{P}} y_i - \frac{1}{\epsilon} K_{\mathrm{V}} \dot{y}_i, \tag{4.19}$$

and K_{P}, K_{V} are gain matrices, and $\epsilon > 0$. Under the influence of the continuous-time feedback laws Γ_i^{sw} for $i \in \{\mathrm{sp}, \mathrm{sa}\}$ the solutions of (4.10) converge to the invariant surface $\mathcal{Z}_{\alpha_i}$ exponentially fast.

In what follows, the combined continuous-time control action during the stance phases $i \in \{\mathrm{sp}, \mathrm{sa}\}$ will be denoted by $\Gamma_i^{\mathrm{c}} = \{\Gamma_i^{\mathrm{su}}, \Gamma_i^{\mathrm{sw}}\}$, depicted in Fig. 4.3.

4.2.2 Flight Phase Motion Control

The continuous-time control design in the flight phases is analogous to that of the stance, thus the exposition here will be terse. Let $x_{\mathrm{f}} := (q', \dot{q}')'$ be the state for the flight phase. Then, the dynamics in both flight phases can be written as

$$\dot{x}_{\mathrm{f}} = f_{\mathrm{f}}(x_{\mathrm{f}}) + g_{\mathrm{f}}(x_{\mathrm{f}})u. \tag{4.20}$$

To allow the use of polynomials with different coefficients in defining the desired evolution of the controlled variables, to each flight phase—that is, the flight phase after the posterior leg liftoff denoted by the index f_1, and the flight phase after the anterior leg liftoff denoted by f_2—we associate the output

$$y_i = h_i(x_{\mathrm{f}}, \alpha_i) := H_{\mathrm{f}} q - h_i^{\mathrm{d}}(s_{\mathrm{f}}(q), \alpha_i), \tag{4.21}$$

where $i \in \{\mathrm{f}_1, \mathrm{f}_2\}$. In (4.21), the controlled variables $H_{\mathrm{f}} q$ are the same in both flight phases, and correspond to the absolute hip and the relative knee angles of the posterior and anterior legs; that is, H_{f} is defined as

$$H_{\mathrm{f}} := \begin{bmatrix} \mathbf{0}_{2\times 2} & H_{\mathrm{sp}} \\ \mathbf{0}_{2\times 2} & H_{\mathrm{sa}} \end{bmatrix}. \tag{4.22}$$

Similarly, in (4.21), for each flight phase $i \in \{\mathrm{f}_1, \mathrm{f}_2\}$, h_i^{d} represents the desired evolution of the controlled variables, which is defined by smooth polynomials parameterized through the monotonic quantity

$$s_i(q_i) = \frac{x_{\mathrm{cm}} - x_{\mathrm{cm},i}^{\mathrm{lo}}}{\Delta_i}, \tag{4.23}$$

where Δ_i is a normalizing constant, and $x_{\mathrm{cm},i}^{\mathrm{lo}}$ is the value of the horizontal coordinate x_{cm} of the torso's COM at liftoff, so that (4.23) represents a monotonically increasing quantity that replaces time in the parameterization of the polynomials. The details associated with the polynomials are presented in the Appendix B; we only mention here that α_i are the parameters introduced by h_i^{d} in each flight phase $i \in \{\mathrm{f}_1, \mathrm{f}_2\}$.

To impose the constraints, a continuous-time controller that zeros the output (4.21) is designed. The process is similar to the one employed in the stance phase. In each phase $i \in \{\mathrm{f}_1, \mathrm{f}_2\}$, the corresponding controller has the form

$$u \ = \Gamma_i^{\mathrm{c}}(x_{\mathrm{f}}, \alpha_i) := \left(L_{g_{\mathrm{f}}} L_{f_{\mathrm{f}}} h_i(x_{\mathrm{f}}, \alpha_i)\right)^{-1} \left[\upsilon(y_i, \dot{y}_i, \epsilon) - L_{g_{\mathrm{f}}} L_{f_{\mathrm{f}}} h_i(x_{\mathrm{f}}, \alpha_i)\right]. \tag{4.24}$$

where the auxiliary control input υ has the same form with (4.19), and it renders the zero dynamics surface

$$\mathcal{Z}_{\alpha_i} = \{x_{\mathrm{f}} \in \mathcal{X}_{\mathrm{f}} \mid h_i(q_{\mathrm{f}}, \alpha_i) = 0, L_{f_{\mathrm{f}}} h_i(x_{\mathrm{f}}, \alpha_i) = 0\} \tag{4.25}$$

invariant and attractive.

4.2.3 Discrete-time Control Laws

At discrete transitions, zeroing of the output may be violated when $x_i^+ \notin \mathcal{Z}_{\alpha_i}$ for $i \in \{\mathrm{sp}, \mathrm{sa}, \mathrm{f}_1, \mathrm{f}_2\}$. x_i^+ is the state of the robot after transition. To ensure that the

zero dynamics surface in each phase is invariant under transitions, the control action updates the parameters α_i according to controllers

$$\alpha_i^+ = \Gamma_i^\alpha(x_i^+) \tag{4.26}$$

for $i \in \{\mathrm{sp}, \mathrm{sa}, \mathrm{f}_1, \mathrm{f}_2\}$ as detailed in the Appendix B.

4.3 Simulation Results

The bounding gait naturally defines a Poincaré return map. We select the Poincaré section to be the flight-to-stance-posterior switching surface $\mathcal{S}_{\mathrm{f}_2\to\mathrm{sp}}$, when the posterior leg touches the ground. The corresponding Poincaré map $\mathcal{P} : \mathcal{S}_{\mathrm{f}_2\to\mathrm{sp}} \to \mathcal{S}_{\mathrm{f}_2\to\mathrm{sp}}$ of the system under the influence of the combined continuous-time (state-based) controllers Γ_i^c and the discrete-time (state-based) controllers Γ_i^α, with $i \in \{\mathrm{sp}, \mathrm{sa}, \mathrm{sd}, \mathrm{f}_1, \mathrm{f}_2\}$ becomes

$$x_{\mathrm{sp}}^+[k+1] = \mathcal{P}\left(x_{\mathrm{sp}}^+[k]\right) \tag{4.27}$$

where $x_{\mathrm{sp}}^+[k]$ is the state after the k-th impact of the posterior leg with the ground. Then, a nominal periodic running gait corresponds to a fixed point of the Poincaré return map defined by

$$x_{\mathrm{sp}}^+ = \mathcal{P}\left(x_{\mathrm{sp}}^+\right) \tag{4.28}$$

4.3.1 Nominal Gait

By using Matlab's `fsolve`, a number of fixed points that respect the physical constraints can be computed for (4.28). Figs. 4.4 and 4.5 presents one such fixed point with an average horizontal velocity 2.527m/s. Numerical computations reveal that the norm of the dominant eigenvalue of the linearized Poincaré map (4.28) at this fixed point is 0.95, implying local exponential stability. Stable points has been found for velocities from 1.6m/s to 3.5m/s for different control parameters. Note also that the resulting nominal motion has neither double stance phase nor slip of the foot.

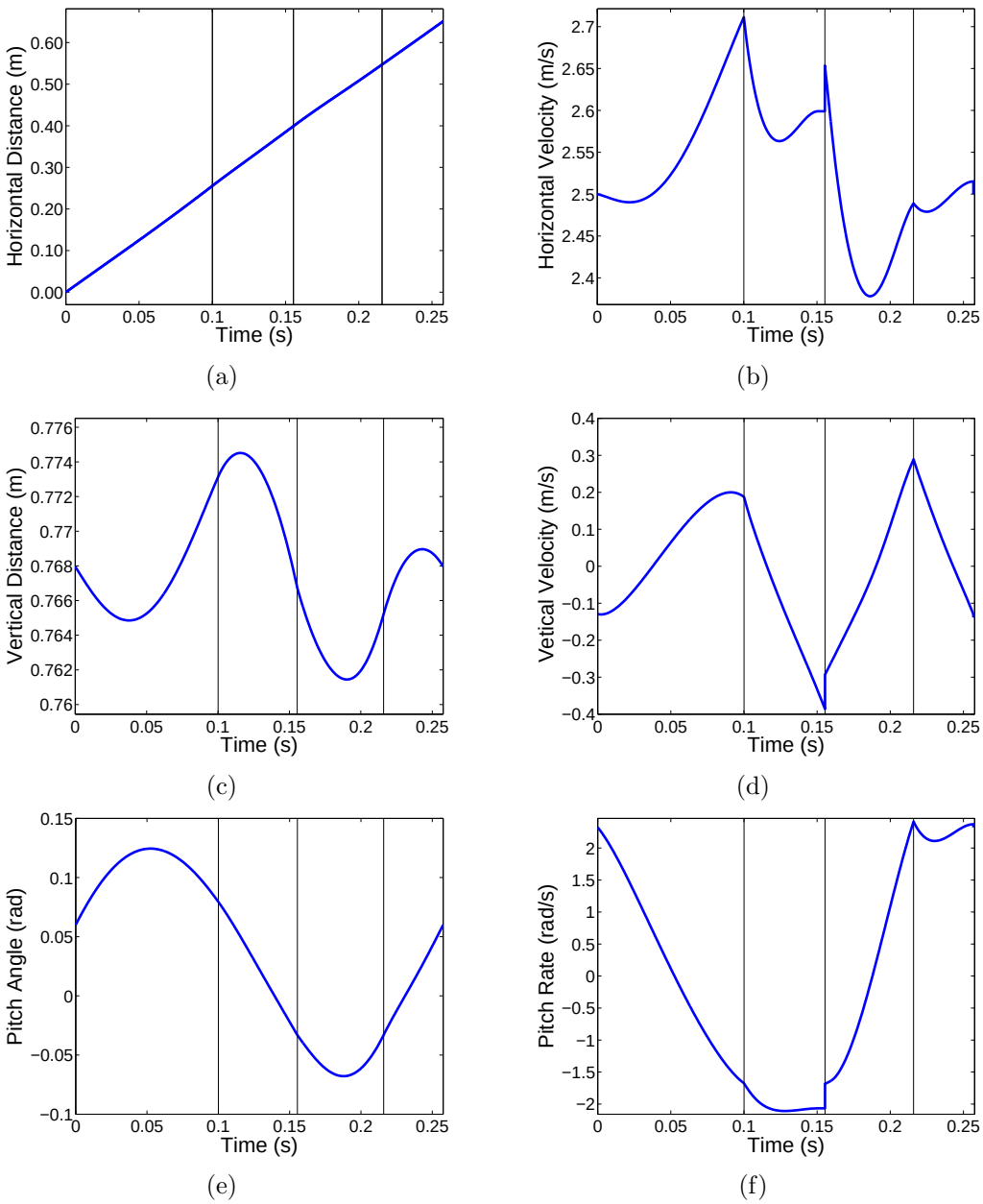

Figure 4.4: Evolution of the torso's COM cartesian variables and pitch angle with respect to time during the nominal bounding motion. The vertical lines correspond to the events; from left to right: posterior leg touchdown, posterior leg liftoff, anterior leg touchdown, anterior leg liftoff.

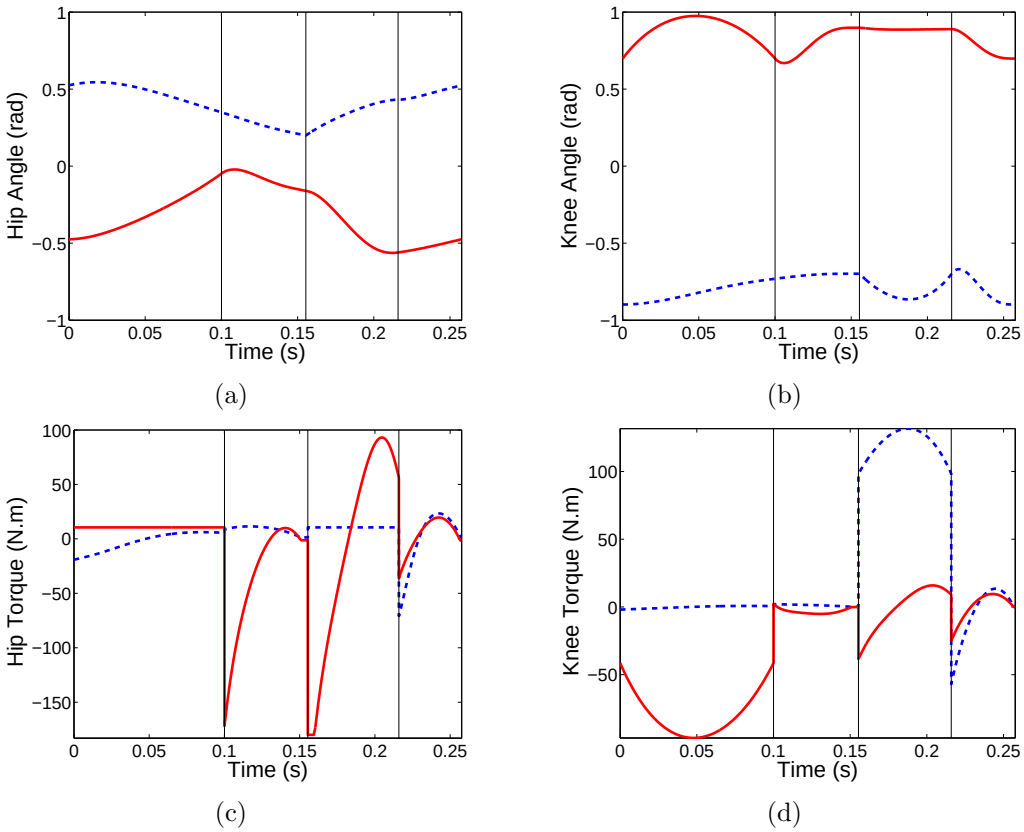

Figure 4.5: Evolution of the leg angles and actuator torques with respect to time during the nominal bounding motion of Fig. 4.4. The red lines correspond to the posterior leg and the blue dashed lines to the anterior leg. The vertical lines correspond to the events, as in Fig. 4.4.

4.3.2 Disturbance Rejection

To evaluate the performance of the controller, we consider the case where the model experiences an unexpected variation in the ground height of 9cm, which is approximately equal to 15% of the leg length. Figures 4.6(a) and 4.6(b) present the evolution of the torso height and the horizontal velocity, showing convergence to the nominal gait. The corresponding continuous-time inputs are presented in Figs. 4.6(c) and 4.6(d), illustrating that the peak torques are well within the capabilities of the hydraulic actuators of the robot.

Figure 4.7 presents an estimate of the domain of attraction of this controller in the $(\dot{x}_{\mathrm{cm}}, y_{\mathrm{cm}})$ plane. The disturbance is added at the end of the stance-posterior

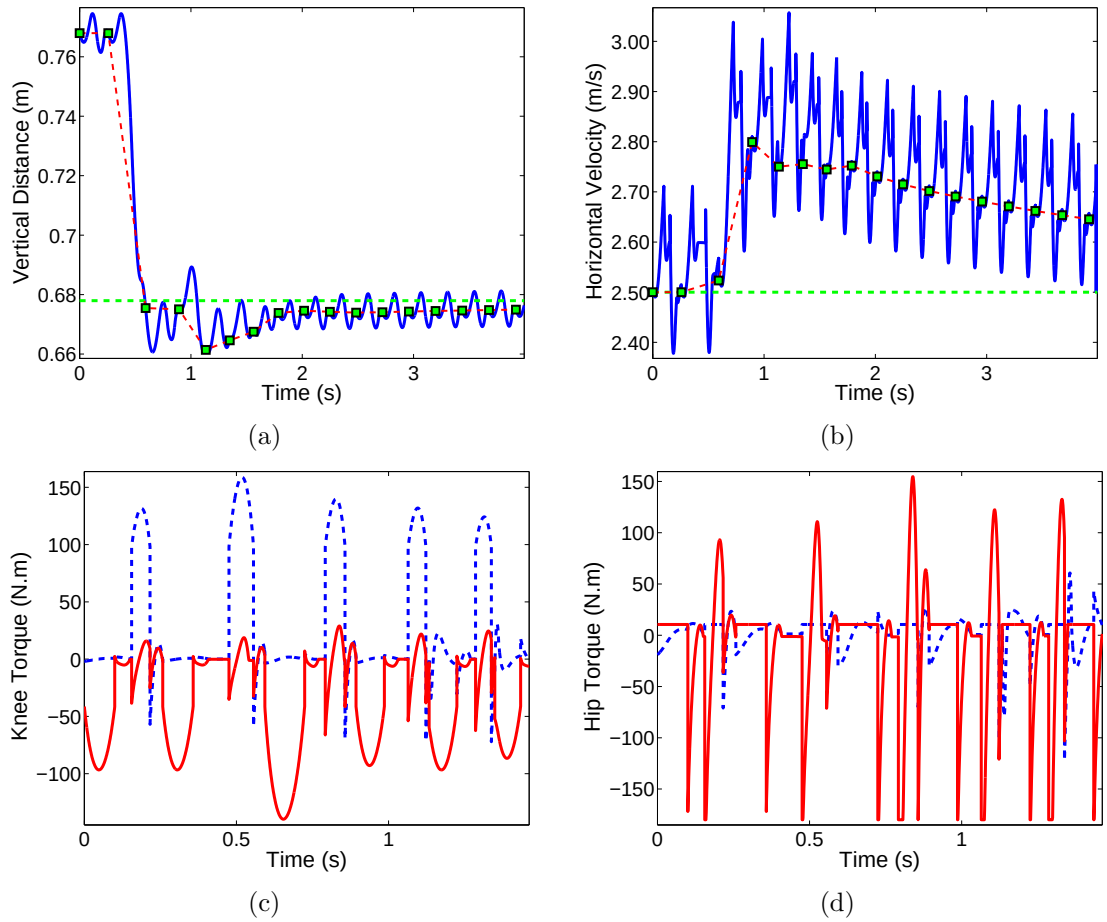

Figure 4.6: Response of the system to a 9cm step-down disturbance showing convergence to the nominal orbit. (a) Hopping height; (b) forward velocity; (c) knee joint actuator torque; (d) hip joint actuator torque. In (a) and (b), the green squares denote the state at Poincare section. In (c) and (d), the red lines correspond to the posterior leg and the blue dashed lines to the anterior leg torques.

phase. The blue area is the part where the robot eventually converges back to the original fixed point. Note that the largest portion of the region of attraction lies in the second quadrant, where the vertical displacement of the robot is increased while the velocity is decreased; this is due to the fact that such disturbances do not drastically increase the total energy of the system, and can be rejected relatively easily.

Finally, Fig. 4.8 presents the sensitivity of the controller to the inaccuracy in the inertia parameters. Here it is assumed that the mass of the thigh and shank has

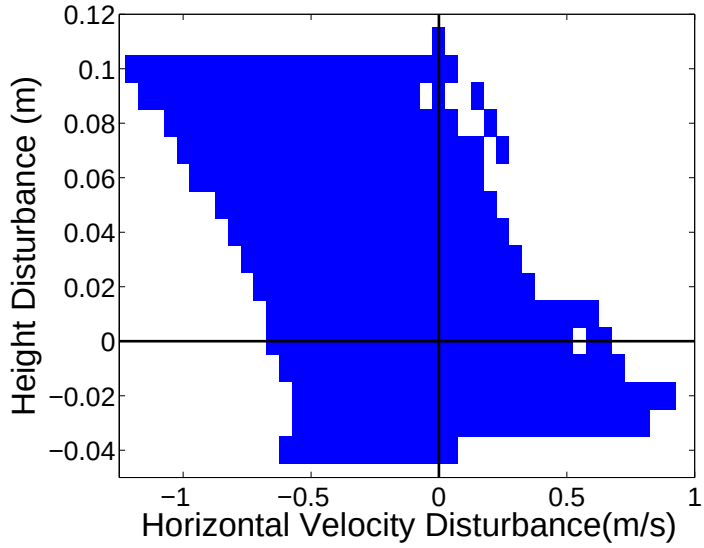

Figure 4.7: An estimate of the region of attraction. The blue area represents states that can be accommodated by the controller.

an inaccuracy randomly distributed within ±30% of the model, while the torso mass and moment of inertia is either increased or decreased by 20% (corresponding to 14kg and 1.4kg-m^2). For all the points randomly tested, the controller is able to converge to a periodic gait. Notice that due to the under-actuation of the system, the robot will not return to the nominal periodic gait, but it will converge to a nearby orbit.

4.4 Conclusion and Discussion

4.4.1 Conclusion

This chapter proposes a framework for designing controllers that integrate actively generated compliance and torque planning with motion control to induce dynamic stable bounding gaits on a model of HyQ. In continuous time the purpose of the controller is twofold. First, it commands suitably parameterized torque profiles to the support leg actuators to create active compliance and to compensate for energy loss. Second, it enforces a set of (virtual) holonomic constraints to restrict the evolution of the hip and knee angles on lower-dimensional surfaces in the state space of the system. The parameters introduced through continuous-time control are updated by the discrete-time controller, which effectively re-plans the constraint profiles providing

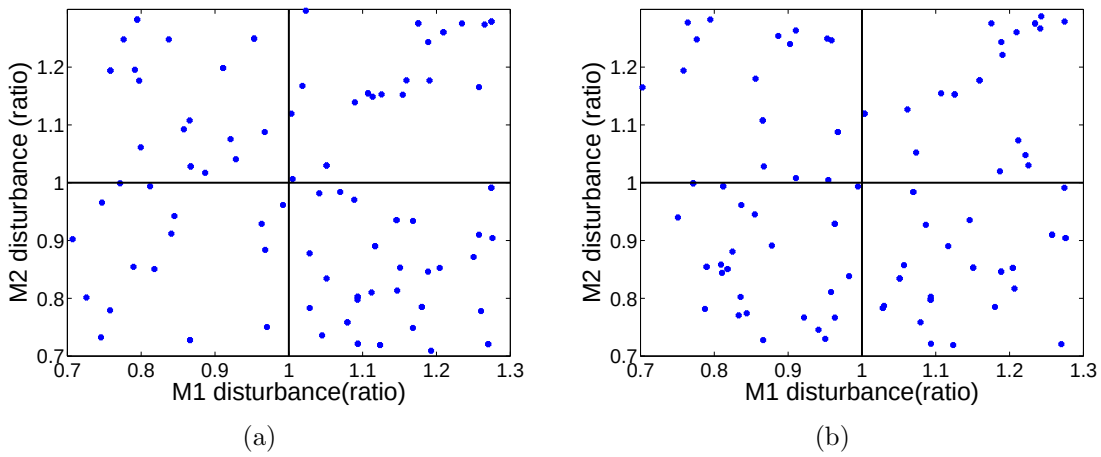

Figure 4.8: Robustness test. The leg mass M_1 and M_2 is randomly perturbed within $\pm 30\%$ of the nominal value. All the points randomly checked stabilized to periodic gaits. The torso mass and moment of inertia is increased by 20% (a) and decreased by 20% (b).

additional control action. The controller is tested in simulation under different disturbances, including unanticipated ground height variation, horizontal velocity, as wells as parameter inaccuracy.

4.4.2 Discussion

Compared to the case where physical springs are used, more energy is consumed when actuators are used to create active compliant elements. From (4.7) and (4.8), it can be observed that the knee actuator provides both a springy term and a "shaping" term. If a rotational spring is incorporated into the knee, the knee actuator only needs to provides the following torque

$$u_i^{\text{act}} = u_i - K_i(\theta_i - \Theta_i) \tag{4.29}$$

where u_i^{act} is the actuator torque after removing the part that can be provided by a passive linear rotational spring with stiffness K_i and rest angle Θ_i; u_i is the nominal torque specified in (4.7) and (4.8). For the nominal gait with 2.527m/s running velocity,

the optimized K_i and Θ_i can be obtained by minimizing the cost

$$W_{\text{mech}} = \sum \int_0^T \max(u_i^{\text{act}} \dot{\theta}_i, 0) dt \tag{4.30}$$

Notice that this cost corresponds to the mechanical energy that is consumed by the actuators.

By using Matlab's `fmincon`, the optimal K_i and Θ_i are numerically obtained. Table 4.2 gives the energy consumption of the hip and knee joints for the two cases with and without knee springs. When no spring is used, the nominal gait consumes 134.6J of energy, corresponding to a mechanical cost of transport (COT) of 0.246. When springs are added to the knee joints, the optimization shows a 40% reduction of energy consumption, corresponding to a COT of 0.148. Figure 4.9 also shows that the peak torque of the knee joint is reduced if a spring is used.

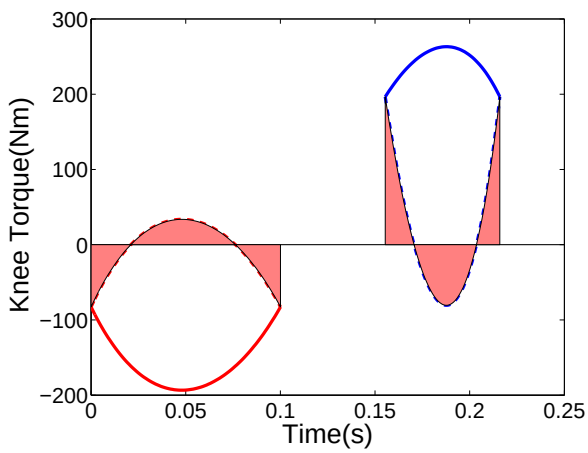

Figure 4.9: The torque of the back and front knee joints (leg pairs). The blue and red solid lines are the nominal torques of the front and back knee joints without the springs. The blue and red dashed lines are the torque of front and back knee actuators when there are springs.

These observations set the stage for the next chapter, in which a novel way to incorporate passive compliance into legged robots is explored. According to the design approach described in Chapter 5, a physical, where a physical spring is put in parallel with the knee actuator to reduce both the torque requirement and the energy consumption of running. In addition, to allow unobstructed joint movement during

Table 4.2: Energy Consumption of the Nominal Gait

(Joule)	Back Knee	Front Knee	Hips	Total
Without spring	39.5	39.2	55.9	134.6
With spring	10.8	14.5	–	81.2

flight phase, a mechanical switch is introduced to disengage the spring at flight phase. The working principle, hardware realization, as well as the experimental evaluation are presented in detail next chapter.

Chapter 5

DESIGN AND EVALUATION OF MONOPEDAL ROBOT SPEAR

Motivated by the role of compliant elements in animal motion, springs are introduced in the driving train of legged robots to reduce energy cost as well as to allow safer interaction with their environment. This chapter presents the working principle, hardware realization, numerical and experimental evaluation of a Switchable Parallel Elastic Actuator (Sw-PEA) design actuating the monopedal robot SPEAR. In the proposed design, a mechanical switch engages the parallel spring only during the stance phase, when it is needed to support body weight and promote energy recovery. During flight, the spring is disengaged to allow for unobstructed joint movement. Furthermore, the proposed design enables online leg stiffness adjustments simply by changing the landing configuration of the knee joint. Numerical simulations as well as experiments demonstrate the effectiveness of the design in promoting energy efficiency without compromising mobility. Part of this chapter has appeared in [54] and [52].

This chapter is organized as follows. Section 5.1 describes the working principle and design details of SPEAR, as well as the test setup. Section 5.2 builds a dynamic model of SPEAR and carries out numerical optimization to find the control strategies for the leg. Section 5.3 documents experiments on the leg. Section 5.4 discusses further improvements and concludes the chapter.

5.1 Design of SPEAR

In this section we present the basic principle underlying the Switchable Parallel Elastic Actuator (Sw-PEA) design, as well as the hardware implementation of the concept in realizing the monopedal robot SPEAR. The energy saving mechanism and the stiffness property of the leg are also discussed.

5.1.1 Working Principle of Sw-PEA

Introducing compliance into running robots is not a straightforward task, and has been a central theme in the development of actuators for such systems [33]. Part of the challenge stems from the fact that different objectives must be satisfied by the mechanical system of a running robot as it goes through different phases of its motion. Compliant elements may facilitate or hinder the achievement of these objectives. For instance, when a leg is in contact with the ground, springs can be beneficial by passively supporting body weight and by recycling mechanical energy that can be used to power the bouncing motion. In addition they can offer a degree of protection against impulsive loads by providing naturally compliant leg-ground interaction. When the leg is in the air, however, compliant elements may cause difficulties. For example, compliance in SEAs usually introduces oscillations which typically require feedback control action to attenuate if the joint damping is not carefully designed. On the other hand, compliance in PEAs may impede the free motion of the joint.

To address this challenge, we propose the Sw-PEA, a new actuator design which incorporates a discrete coupling element—a switch—to engage compliance in parallel with a motor when elastic energy storage is needed. For illustration purposes, Fig. 5.1(a) presents the underlying principle of the proposed design in the context of a prismatic joint configuration. In Fig. 5.1(a), Link A is assumed to be the base, and is connected to Link B through an actuator and a compliant element inserted in parallel with the actuator. The compliant element contains two springs S_1 and S_2 with different stiffnesses: the spring S_1 has stiffness K_1, much larger than the stiffness K_2 of spring S_2; i.e., $K_1 \gg K_2$. The two springs are connected in series through a mechanical switch realized by a key and a chain. The effective stiffness of the combined springs is determined by the status of the key. In more detail, when the key is inserted in the chain, the left side of the hard spring S_1 is restrained; hence, in this configuration, the mechanical switch engages S_1, leading to a large joint stiffness K_1 that favors energy storage as Link B moves. When the key is not in the chain, the springs S_1 and S_2 are connected in series, and the effective stiffness of the joint is mainly determined by

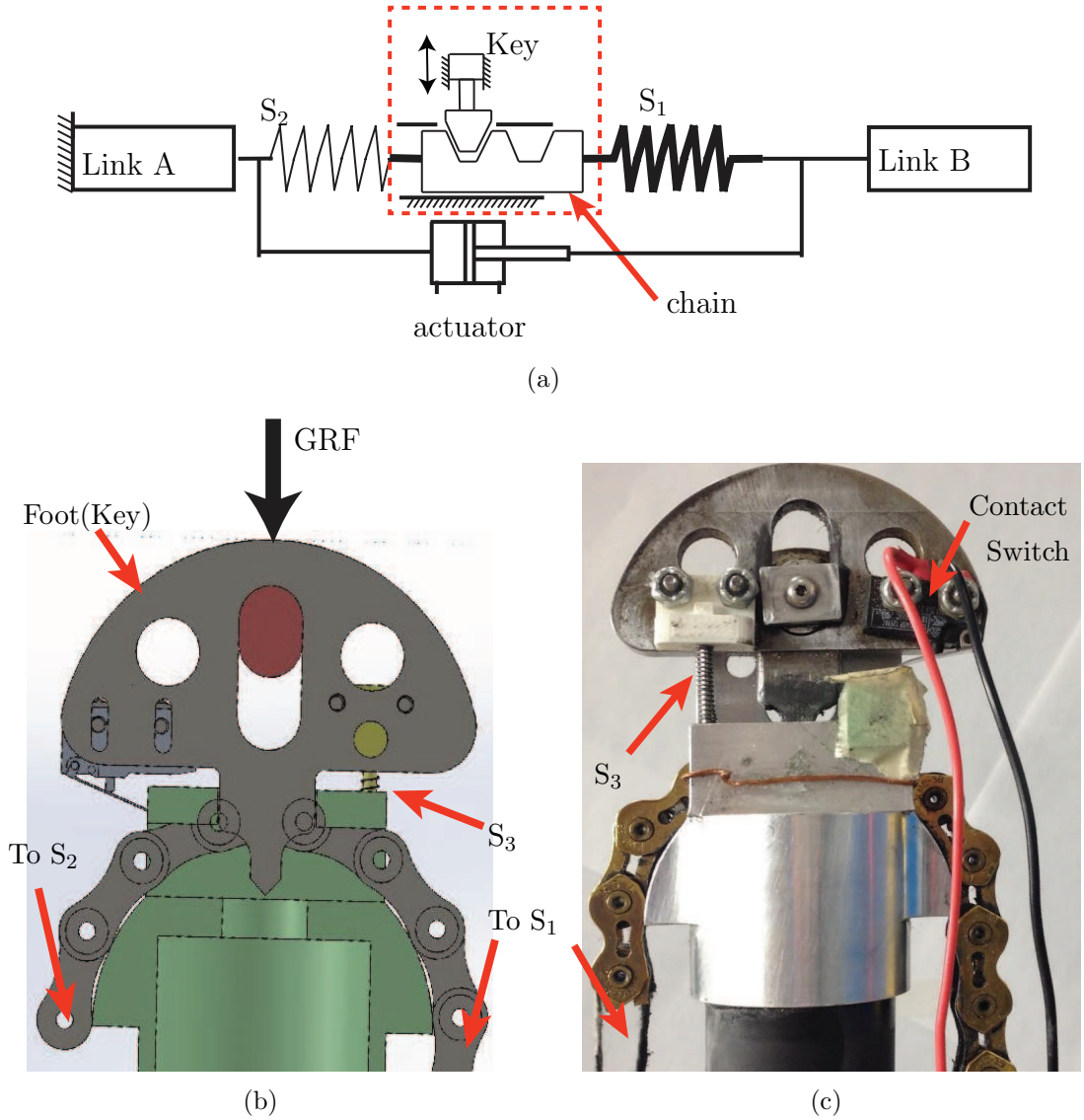

Figure 5.1: (a) The schematic of the proposed Sw-PEA design. The stiffness of the joint is determined by the status of the Key. (b) The section view of the foot which functions as the Key in (a). Here the foot is inserted into the chain by the ground reaction force (GRF) and spring S_1 is engaged. S_3 is a small spring used to keep the foot unplugged from the chain when there is no force applied. The contact switch is used to determine if the foot is inserted in the chain. (c) The manufactured foot.

the softer spring S_2. With K_2 negligible, the hard spring S_1 is effectively "switched off," and this configuration favors precise joint motion control via the actuator, as if no spring is present. In addition, when the key is not inserted in the chain, the rest

length of the combined compliant element can be easily adjusted by using the parallel actuator to modify the locking positions of the chain.

5.1.2 SPEAR: A Leg Design that Uses the Sw-PEA

The monopedal robot SPEAR has been designed to explore the implications of switchable parallel elastic actuation on realizing dynamic running gaits; Fig. 5.2 shows the assembled robot and a schematic representation of the mechanical system. SPEAR consists of a torso and two links corresponding to the thigh and the shank of a kneed leg that terminates at a point foot (toe). To reduce the overall weight of the system, the thigh is composed of two lightweight aluminum plates and the shank is formed by a carbon fiber tube. The thigh is connected to the torso via the hip joint with a range of motion $[-85°, 85°]$, while the shank is connected to the thigh by the knee joint with a range of motion $[-10°, 140°]$. The robot's torso is connected to a boom as described in Section 5.1.5 below. The assembly is actuated by two brushless motors; one responsible for the knee and the other the hip joint. To further reduce the moment of inertia with respect the hip axis, the knee motor is placed in proximity to the hip joint, and a cable-pulley system is used to transmit the motor torque to the knee. Table 5.1 provides a list of some relevant parameters of SPEAR.

As indicated in Fig. 5.2(b), the knee joint of SPEAR is driven by an Sw-PEA. In our implementation of the concept, the Sw-PEA is arranged so that the hard spring S_1 is engaged only during the stance phase, thereby harnessing its elastic energy storage capability when it is needed. During the subsequent flight phase, S_1 is disengaged, allowing the actuator to shorten or lengthen the leg without interfering with the spring. This configuration is realized as shown in Fig. 5.2. One end of a hard spring S_1 is rigidly attached to the thigh by a steel cable. The other end of S_1 is attached to another cable, which first wraps over the circular knee spacer that is rigidly mounted on the shank, and then connects to one end of a roller chain that passes through the foot. The other end of the chain is then attached to the shank via a soft return spring S_2.

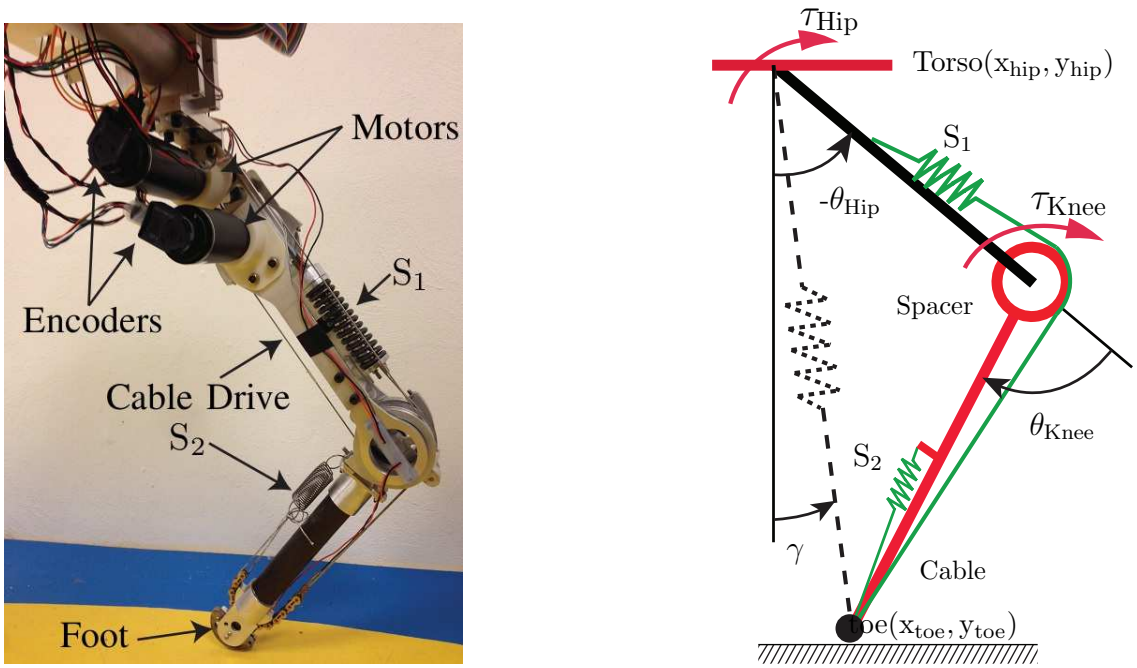

(a) (b)

Figure 5.2: (a) The manufactured leg. A cable-pulley system is used to move the knee actuator more close to the hip axis. (b) The schematic drawing of the robotic leg. One end of the large spring S_1 is attached to the thigh by a steel cable, while the other end first pass through the knee spacer, then pass through the foot (at this part, the cable is replaced by a roller chain), then attached to the shank by the small spring S_2.

The chain is one part of a "mechanical" switch, which effectively realizes the key/chain block in Fig. 5.1(a). The other part is the foot itself, as shown in Fig. 5.1(b)-5.1(c). The foot is designed to have a tooth shape at one end, and is connected to the shank via a prismatic joint, which allows the foot to move up and down with a maximum displacement of 1cm. During the stance phase, the ground reaction force pushes the tooth of the foot inside the chain, thereby engaging the spring S_1, as shown in Fig. 5.1(b)-5.1(c). During the flight phase, an additional small spring S_3 is used to push the foot outside the chain, thereby disengaging the spring S_1. As a result, this simple "mechanical" realization of the switch does not require additional control effort to synchronize the engagement of the energy storing spring S_1 with the state of the leg.

Table 5.1: SPEAR Parameters

Parameter	**Value**	**Units**
Torso mass (including boom and CPU) (M)	4.91	kg
Thigh mass (M_1)	2.43	kg
Thigh inertia (including motor) (J_1)	0.06	kgm^2
Shank mass (M_2)	0.73	kg
Shank inertia (including motor) (J_2)	0.02	kgm^2
Thigh length (L_1)	0.320	m
Shank length (L_2)	0.327	m
Hip friction coefficient (f_1)	0.31	Nm/(rad/s)
Knee friction coefficient(f_2)	0.06	Nm/(rad/s)
Motor torque constant (K_t)	0.0414	Nm/A
Motor coil resistance (R)	0.72	Ω

As a final remark, note that other types of locking devices—such brakes or clutches—could be used to implement the switch in the Sw-PEA concept of Fig. 5.1(a). In the case of running robots, however, due to the large ground reaction forces that are developed, a relatively high locking torque capability is required. While locking devices capable of reliably holding such torques are commercially available, they tend to be heavy and would have the undesirable effect of increasing the weight of the robot. Contrary to these solutions, the passive self-locking nature of the proposed "mechanical" switch makes the overall design compact and reliable. In addition, since the larger the spring deformation is, the larger the ground reaction force that pushes the key into the roller chain will be, the proposed design can be easily scaled to larger robots, as long as a stronger chain and a suitably selected spring are used.

5.1.3 Energy Flow of Sw-PEA in SPEAR

Figure 5.3 presents the energy flow diagram of the knee joint of SPEAR, from the energy source (battery) to the leg segments. Assuming that the total energy lost due to resistive (Ohmic) heating in the electrical circuitry and due to switching effects

in the motor drivers is small, three principal sources of energy dissipation are identified. As in [92], these are associated with Joule heating in the electromagnetic motor that actuates the knee joint, friction losses in the mechanical transmission system—primarily in the gearbox—and interaction losses occurring at the interface between the leg and the substrate.

As indicated in Fig. 5.3, the proposed Sw-PEA design improves the energetic performance of SPEAR mainly in two ways. First, the spring recycles part of the mechanical energy as it compresses during the early stages of the stance phase and uses it subsequently to power the cyclic motion. Negative mechanical work is inevitable in running, due to the forces required to re-direct the center of mass during stance. When negative work is performed, the energy flows back from the leg segments through the transmission to the actuators. In the absence of regenerative braking circuitry—the MIT Cheetah [92] features such capabilities, which though are typically not available in most current legged systems, including SPEAR—this energy is eventually lost in friction and Joule heating in the motors. The parallel spring in the Sw-PEA that is engaged during stance mitigates this effect by storing energy and release it later in the cycle.

The second aspect of the Sw-PEA that contributes to reduced energy consumption is associated with the configuration of the spring S_1, which is connected in parallel with the actuator. As a result, the torques developed by the spring and the combined actuator/transmission system are added during stance so that the need for the motor unit to develop large torques is lessened. This is beneficial for two reasons. First, reducing the required torque allows the motor to convert electrical energy to mechanical more efficiently. Indeed, neglecting rotor friction, the efficiency η_1 of a DC motor can be approximated by

$$\eta_1 \simeq 1 - \frac{I^2 R}{VI} = 1 - \frac{R}{K_t V}\tau_{\mathrm{m}} \tag{5.1}$$

where K_{t} is the torque constant, V is the supply voltage, I is the current that flows in the motor's coils with resistance R, and τ_{m} is the motor torque. Thus, for a given motor and voltage applied, the energy dissipated due to Joule heating decreases with

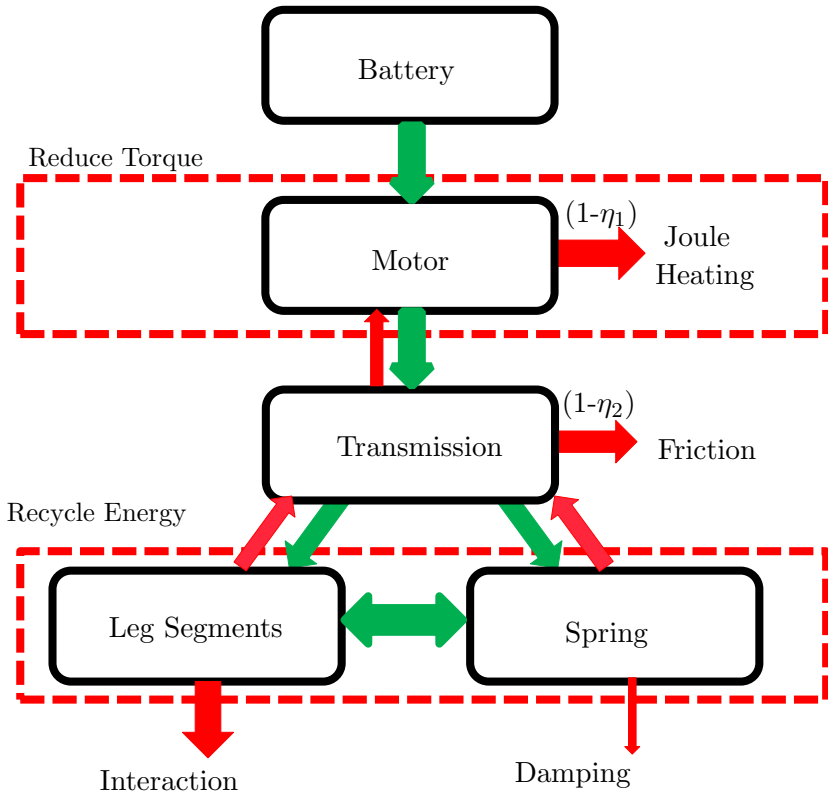

Figure 5.3: Energy flow of the Sw-PEA in the knee joint of SPEAR at stance phase, where the red arrows are energies that are eventually lost. The flight phase energy flow is similar but without the spring block and impact.

the motor torque. Second, due to the reduced torque requirement, a gearbox with a relatively smaller ratio can be chosen, which further improves the efficiency η_2 of the transmission system [36]. Hence, for a given specification of output torque, different combinations of motors and gearboxes can be selected depending on whether optimizing η_1 or η_2 is the objective of the specific design. It is important to emphasize though that choosing a smaller gear ratio is advantageous, for it decreases the reflected moment of inertia and it enhances joint back-drivability. This fact is particularly important in our implementation of the Sw-PEA concept. In SPEAR, a $25:1$ reduction ratio is used for the Sw-PEA as a design choice that balances transmission friction losses and Joule heating, and ensures a sufficiently back-drivable knee joint.

Finally, note that—contrary to the SEA architecture—in PEAs the combined

motor and transmission unit is not totally isolated from the leg segments, and thus it is exposed to the impulsive load associated with the impact of the leg at touchdown. The cable driven system adopted in SPEAR and the back-drivability of the knee joint provide sufficient protection against the contact loads. Additional protection of the Sw-PEA could be achieved by incorporating a torsion bar or a belt transmission system to isolate impact.

5.1.4 Stiffness Property of the Leg

Stiffness of the Knee Joint

Due to the geometry of the leg, the prismatic springs S_1 and S_2 have the equivalent effect of a rotational spring located at the knee joint. To relate the stiffness of the prismatic springs with the corresponding stiffness of the joint we will assume negligible deformation in the cables. With reference to Fig. 5.4, keeping the thigh fixed and rotating the shank from D to D′ causes the knee joint to rotate by an angle $\Delta\theta$, thereby deforming the prismatic spring by $\Delta L = r\Delta\theta$, where r is the radius of the knee spacer. As a result, the stiffness K_{Rot} of the rotational spring at the knee joint can be computed by

$$K_{\text{Rot}} = \frac{(K_{\text{Lin}} \times \Delta L) \times r}{\frac{\Delta L}{r}} = K_{\text{Lin}} \times r^2 \ , \tag{5.2}$$

where K_{Lin} represents the stiffness of the prismatic spring that is engaged. At stance, when the mechanical switch engages S_1,

$$K_{\text{Rot}} = K_{\text{Lin}} \times r^2 = K_1 \times r^2 \ . \tag{5.3}$$

In our design, $K_1 = 39000$N/m and $r = 1.5$in, resulting in $K_{\text{Rot}} = 56.67$Nm/rad. For this equivalent rotational stiffness, 28J of energy can be stored in the spring for a 1rad deformation. During flight, on the other hand, the springs S_1 and S_2 are connected in series and the effective rotational stiffness is

$$K_{\text{Rot}} = K_{\text{Lin}} \times r^2 < K_2 \times r^2 \ . \tag{5.4}$$

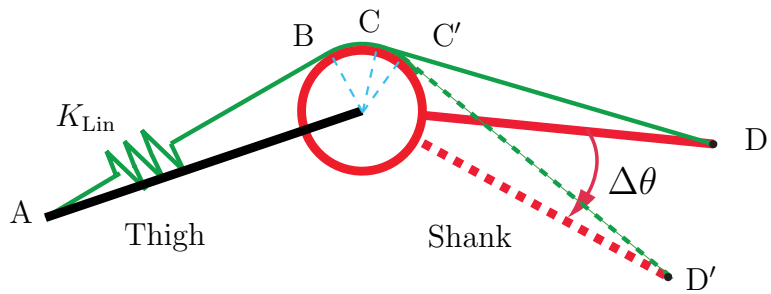

Figure 5.4: The relation between the linear spring and the corresponding knee rotational spring. The spring depicts the effect of S_1 or S_2.

With $K_2 = 310$N/m and $r = 1.5$in, the knee joint has a stiffness below 0.3Nm/rad, which is small enough and will be neglected.

To summarize, due to the switching, the knee joint of the SPEAR has a stiffness of 56.67Nm/rad when the leg is on the ground, acting primarily as an elastic energy storage element, developing torque

$$\tau_{\text{spring}} = -56.67(\theta_{\text{knee}} - \theta_{\text{knee}}^{\text{TD}}) \tag{5.5}$$

where $\theta_{\text{knee}}^{\text{TD}}$ is the touchdown angle of the knee. When the leg is in the air, however, the stiffness of the knee becomes smaller than 0.3Nm/rad, so that the motors can efficiently control the leg's motion.

Adjusting the Virtual Stiffness of the Leg

Leg compliance—passive or active—is essentially a defining feature of running [60], and the ability to vary the stiffness of the leg provides a useful tool for gait control [37]. The implementation of the Sw-PEA in SPEAR offers a simple way to adjust leg stiffness *on line* and in an energy efficient manner. Practically, this is achieved by varying the knee angle during flight to realize different landing configurations of the leg, so that the energy-storing spring S_1 engages at different knee angles when the foot contacts the ground.

In more detail, the equivalent rotational compliance of the knee joint corresponds to a nonlinear virtual spring acting along the line that connects the hip joint with the

foot; see Fig. 5.2(b). Furthermore, as detailed in [84], changing the rest angle of the knee compliance effectively modifies the stiffness of the virtual spring. In the context of the SPEAR, the mechanical switch engages the energy-storing spring S_1 as soon as the foot contacts the ground, and the value of the knee angle just prior to touchdown specifies the rest angle of the knee rotational compliance. As a result, modifying the angle of the knee at touchdown provides an effective means for adjusting the overall stiffness of the virtual spring between the hip and the foot. Note that it is very easy for the knee motor to achieve the desired knee angle during flight, when S_1 is not engaged, due to the rotational stiffness of the spring S_2 being negligible. Figure 5.5 presents the force-displacement relationship of the virtual spring for different knee touchdown angles. This simple mechanism of adjusting the effective stiffness of the leg will be explored further in the following sections.

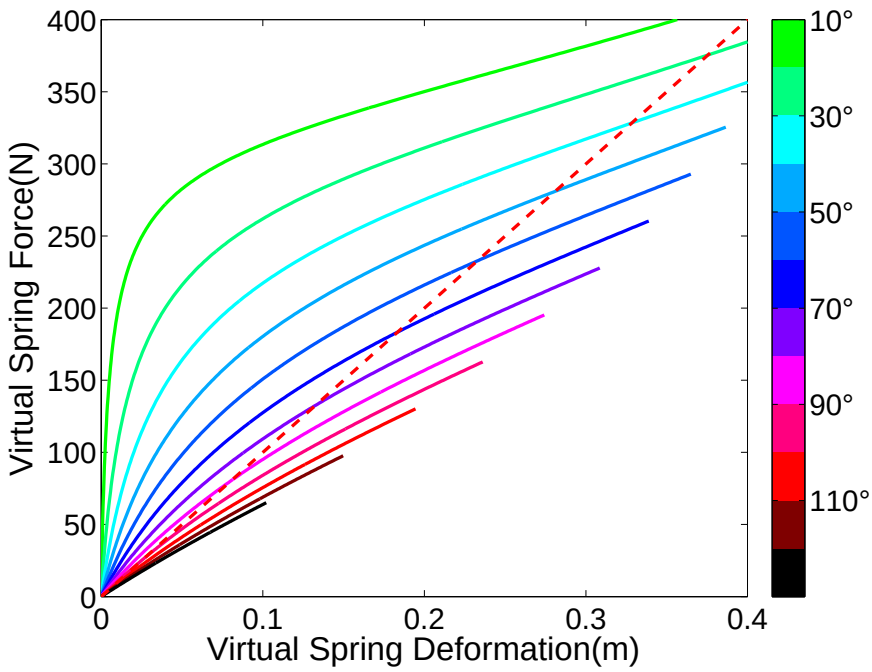

Figure 5.5: Changing the stiffness of the leg by changing the touchdown angle of knee joint. The x-axis is the deformation of the virtual spring, while the y-axis is the force of the virtual spring. As the knee becomes more straight (varying from 130° to 10°), the virtual spring is becoming stiffer.

5.1.5 Test Setup and Electronic System

To realize hopping motions in SPEAR, a support system consisting of a vertical and a horizontal boom arranged as shown in Fig. 5.6 has been constructed. SPEAR's torso is mounted at one end of the two-meter long horizontal boom, which restricts the motion of the hip joint on the surface of a sphere. In what follows, however, due to the relatively large length of the horizontal boom, we will assume that the motion of the system occurs in the sagittal plane. No counter weight is used, and the boom adds to the mass of the torso. A safety cable is used to offer some protection, but it does not prevent the leg from falling.

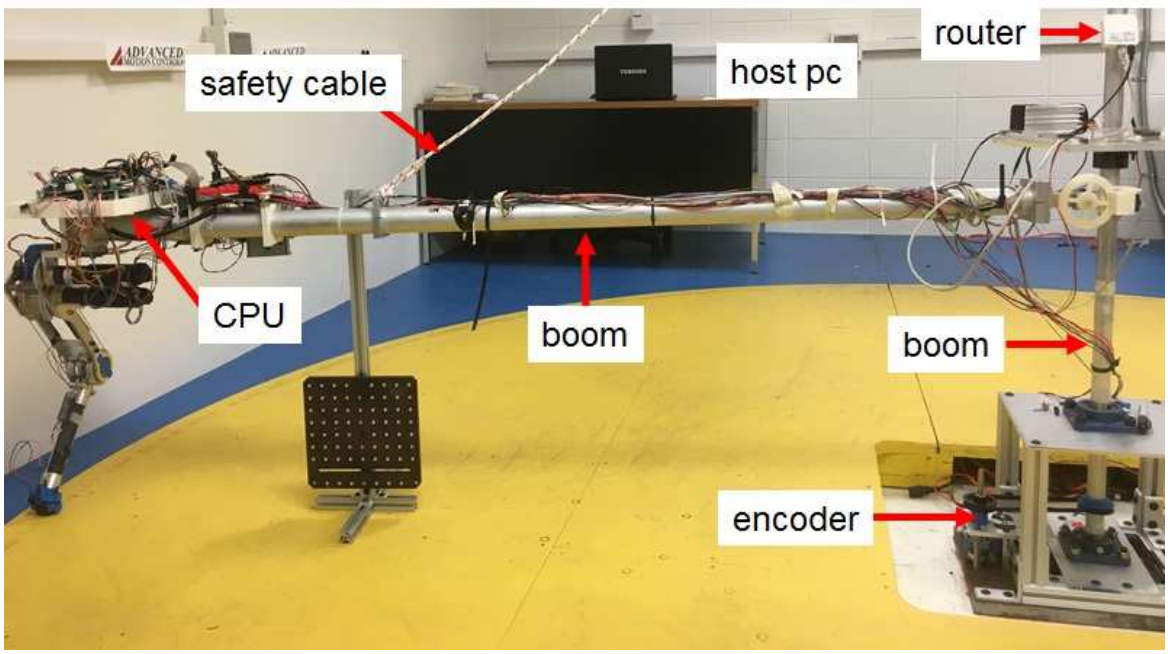

Figure 5.6: The testbed used for 2D hopping experiments.

To implement the locomotion controllers used in experiments—see Section 5.3 below for details—the position and velocity of the leg with respect to the world frame are required. To obtain this information, two incremental encoders are used to measure the rotation of the boom. Note that due to the relatively large length of the

horizontal boom, a $30,000$ counts per revolution encoder is used to estimate the horizontal displacement of the robot with accuracy 0.1mm, which is sufficient for controller implementation.

To monitor its motion, SPEAR is equipped with a collection of sensors to measure and estimate the robot's state, as well the contact state of the leg. At the joint level, measurements from the motor encoders are combined with data from joint potentiometers to provide accurate information regarding the position of the joints and the deformation of the springs. Furthermore, a snap-acting switch is placed at the foot to detect the state of the leg, stance or flight.

Figure 5.7 present the electronic system of SPEAR. A PC/104 stack computer with a low-power 1.6GHz Intel Atom CPU is used as the target computer, running a Simulink Realtime control model at 1kHz. Two motor servos with current control ability are used to servo the analog reference current signal from the DA converter of target computer. The current is measured by the motor servo and are sent to the target computer through the RS485 bus at 921.6kbps, which will be used to calculate the energy consumption. The target computer can connect with a laptop through a mini wireless router, allowing online debugging and data logging. As a prototype for a quadrupedal robot, the leg is designed to be power autonomous. The whole system can be powered by three 22.2V LiPo batteries, two of which are used to power the motor, a third for the control electronics.

5.2 Simulation Evaluation

In this section, we investigate the performance of SPEAR in the context of periodic hopping in place. The results are based on numerical optimization using a model of the robot, and provide insight for the experiments detailed in Section 5.3.

5.2.1 Hybrid Dynamics of the Hopping Gait

The model of SPEAR used in this section is presented in Fig. 5.8. As was described in Section 5.1, during stance, the mechanical switch in the Sw-PEA engages

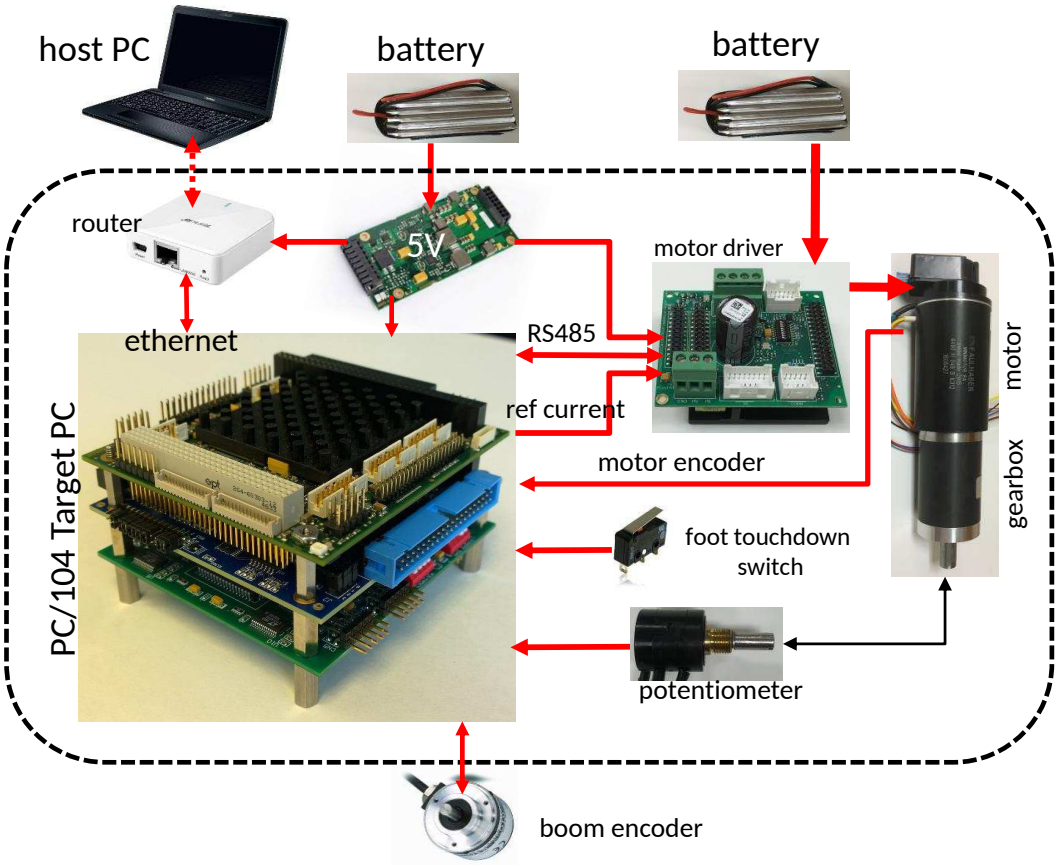

Figure 5.7: The electronic system of the leg. All the parts are commercial off-the-shelf components.

the stiff spring S_1, allowing energy storage. During the subsequent flight phase, the switch disengages S_1, allowing the actuator to control the knee joint so that only the soft spring S_2 is involved. With the effect of S_2 negligible, the torque developed at the (unilateral) rotational knee spring can be modeled by

$$\tau_{\text{spring}} = \begin{cases} -56.67\max\{(\theta_{\text{knee}} - \theta_{\text{knee}}^{\text{TD}}), 0\}, & \text{if } y_{\text{toe}} = 0 \\ 0, & \text{if } y_{\text{toe}} > 0 \end{cases} \tag{5.6}$$

where $\theta_{\text{knee}}^{\text{TD}}$ is the touchdown angle of the knee.

With reference to Fig. 5.8, the configuration variables of the model are selected as $q := [x_{\text{hip}}, y_{\text{hip}}, \theta_{\text{hip}}, \theta_{\text{knee}}]^{\text{T}}$. The continuous-time dynamics of SPEAR in hopping

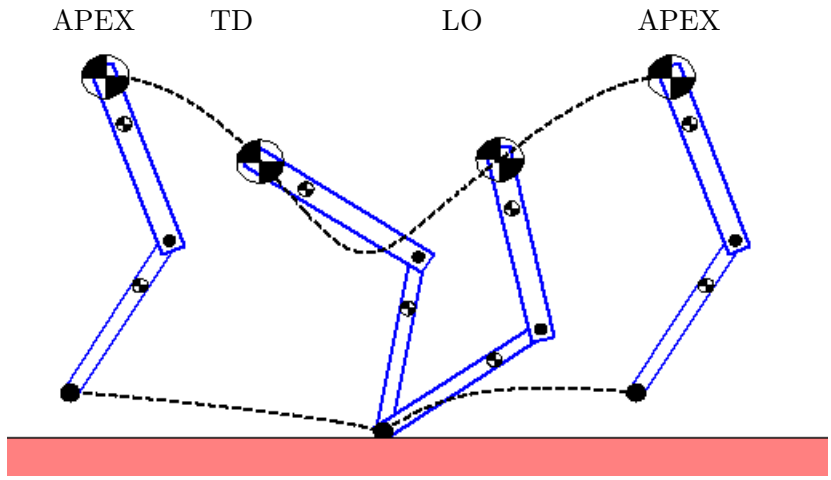

Figure 5.8: A complete hopping gait that begins at the apex.

can then be written in the form

$$D(q)\ddot{q} + h(q, \dot{q}) = B(\tau_{\text{Act}} + \tau_{\text{Pas}} + \tau_{\text{Damp}}) + J^{\text{T}}(q)F_{\text{ext}}, \tag{5.7}$$

where D is the inertia matrix and h is the vector of the configuration and the velocity dependent forces, excluding the spring's force. The matrix B maps to the vector of generalized forces the actuator (in joint) torques $\tau_{\text{Act}} := [\tau_{\text{m,hip}}, \tau_{\text{m,knee}}]^{\text{T}}$, the joint viscous friction torque τ_{Damp}, and the passive (unilateral) knee spring torque $\tau_{\text{Pas}} := [0, \tau_{\text{spring}}]^{\text{T}}$ computed by (5.6). Finally, J is the Jacobian matrix, mapping the contact force $F_{\text{ext}} = [F^x_{\text{ext}}, F^y_{\text{ext}}]^{\text{T}}$ to the vector of generalized forces. The contact of the toe with the ground is modeled as a unilateral constraint so that $J\ddot{q} + \dot{J}\dot{q} = 0$, which, together with (5.7), can be used to specify the acceleration $\ddot{q}$ and the contact force F_{ext}. During flight F_{ext} is zero.

The dynamics of hopping can be captured by a hybrid system composed of flight and stance phases that are separated by touchdown (TD) and liftoff (LO) events. Without loss of generality, the apex height event (APEX) is also defined and used to denote the beginning of a hopping gait. These events are defined as follows.

Touchdown Event

The transition from flight to stance occurs when the height of the toe decreases to zero. This transition is modeled as an inelastic instantaneous impact according to the assumptions in [102, Section 3.4]. This impact model leads to a jump in the velocity while keeping the configuration unchanged.

Liftoff Event

The transition from stance to flight phase happens when the unilateral constraint between the toe and the ground is open, i.e., F^y_{ext} decreases to zero. With the knee and hip joints actively controlled, the liftoff event can be initiated by actively flexing the joint. To ensure that the energy stored in the spring during compression is released back to the system, liftoff is specified when the knee angle as the leg extends reaches its touchdown value.

Apex Event

Without losing generality, a hopping gait is defined to begin and end when the hip axis reaches its maximum height at flight phase, characterized by $\dot{y}_{\text{hip}} = 0$.

5.2.2 Generation of Periodic Hopping Motions

To explore the effect of the Sw-PEA on the energetics of SPEAR, a controller for generating periodic hopping motions is developed and a performance index that captures electrical energy consumption is used to define an optimization problem, which is solved numerically. The controller is considered successful if it can generate periodic gait.

Input Parametrization

The controller essentially excites the dynamics by imposing desired torque inputs at the hip and knee joints during stance and nominal joint angle trajectories during

flight. In more detail, during stance, the joint torques are commanded according to the prescription

$$\tau_{\mathrm{m},i} = a_0 + \sum_{k=1}^{5} a_k^i \sin(k\omega s) + b_k^i \cos(k\omega s) \ , \tag{5.8}$$

for $i \in \{\mathrm{hip}, \mathrm{knee}\}$, where $s := t - t_{\mathrm{TD}}$ is the stance time reset at the touchdown event. Note that by parameterizing the torque directly, it is easier to compute motions that take advantage of compliance in the leg. During flight, on the other hand, PD controllers are used enforce the nominal joint angles $\bar{\theta}_i$ for $i \in \{\mathrm{hip}, \mathrm{knee}\}$ parameterized via Bézier polynomials

$$\bar{\theta}_i(s) = \sum_{k=0}^{5} c_k^i \frac{5}{k!(5-k)!} (s)^k (1-s)^{5-k} \ , \tag{5.9}$$

where s is the normalized time computed by

$$s = \frac{t - t_{\mathrm{LO}}}{t_{\mathrm{APEX}} - t_{\mathrm{LO}}} \quad \text{or} \quad s = \frac{t}{t_{\mathrm{TD}}} \ , \tag{5.10}$$

for the ascending and descending parts of the flight phase, respectively; in (5.10), t_{LO} and t_{TD} represent the liftoff and touchdown instants.

Return Map and Periodic Motions

The existence of periodic hopping gaits will be studied through the numerical construction of a Poincaré map $\mathcal{P}$ defined at the apex height event, as

$$z[k+1] = \mathcal{P}(z[k], \alpha[k]) \ , \tag{5.11}$$

where z is the state of the systems at a apex excluding the cyclic variable x_{hip}, and α comprises all the parameters introduced by the stance and flight control inputs (5.8) and (5.9), respectively. Then, finding periodic hopping gaits reduces to finding state vectors z and parameters α such that $z = P(z, \alpha)$.

Cost Functions and Optimization

To provide cost functions capable of capturing the total cost of transport—including electrical energy losses—a simplified DC actuator model is included in the

model. It is assumed that the electric time constant is small enough to be negligible and that the motors can be treated as ideal torque sources. Having the friction of the rotors lumped into the damping coefficient of the joints, the motor model becomes

$$I_i = \frac{\tau_{\mathrm{m},i}}{n_i K_t} \quad \text{and} \quad V_i = \dot{\theta}_i n_i K_t + R I_i, \tag{5.12}$$

for $i \in \{\text{hip}, \text{knee}\}$, where V_i and I_i are the supply voltage and current of the motor, R is the terminal resistance of the motor, $\tau_{\mathrm{m},i}$ is the torque of the joint, and n_i is the gearbox ratio. The hip and knee motors of SPEAR is the same, where the gearbox reduction ratio is 25:1 for the knee, and 60:1 for the hip. The rest of the parameters are listed in Table 5.1.

With the actuator model of (5.12), the electrical energy consumed during the gait can be approximated as in [105] by

$$W_{\mathrm{ele}} = \sum_{i \in \{\text{knee,hip}\}} \int_0^T \max\{(V_i I_i), 0\} dt = \sum_i \int_0^T \max\{(I_i^2 R + \tau_{\mathrm{m},i} \dot{\theta}_i), 0\} dt \ , \tag{5.13}$$

where T is the duration of a stride. Note that when negative mechanical work is performed at the knee joint, energy flows back from the leg segments to the motor, as described in Fig.5.3. Part of this energy could have been recovered to reduce the total energy consumption using regenerating motor driving circuitry as in [91]. However, as is typical in many legged robots, SPEAR does not have such capabilities; hence, as indicated by (5.13), we assume that this part of the energy is eventually dissipated.

With (5.11) and (5.13) available, finding periodic hopping gaits that minimize electrical energy consumption can be formulated as the constrained optimization problem

$$\begin{aligned} \text{minimize} \quad & W_{\mathrm{ele}}(\alpha, x) \\ \text{such that} \quad & z = \mathcal{P}(z, \alpha) \\ & \theta_{\mathrm{hip}} \in [-70^\circ, 70^\circ] \ , \ \theta_{\mathrm{knee}} \in [0^\circ, 140^\circ] \ . \end{aligned} \tag{5.14}$$

Additional equality constraints can be incorporated to (5.14) to compute hopping motions satisfying certain desired specifications; e.g., achieve a desired maximum toe clearance Y_{toe} or land with a desired knee touchdown angle $\Theta_{\mathrm{knee}}^{\mathrm{TD}}$. The optimization (5.14) is solved using MATLAB's `fmincon`.

5.2.3 Optimization Results

Recycling Mechanical Energy

The results presented in Fig. 5.9 correspond to an optimized hopping-in-place gait computed for $Y_{\text{toe}} = 7.5$cm. It can be seen from Fig. 5.9(a), that both the knee and hip actuators perform positive work during stance, with small amount of negative work done in flight. On the other hand, focusing on the spring, Fig. 5.9(a) indicates that the spring performs negative work during leg compression, which is stored and released later when the leg extends. Note also that during the later stages of the stance phase the parallel knee actuator does contribute to the positive work done by the spring by essentially "shaping" its response. In addition, compared with the spring, the motor only provides a small portion of the work.

Reducing motor torque requirements

Figure 5.9(c) presents the torques developed by the knee and hip motors and by the spring for the optimized hopping gait. It can be observed that during stance, the peak torque of the knee actuator is smaller than 2Nm. On the other hand, the spring generates a much larger torque, exceeding 35Nm at its peak. This drastic reduction in the required motor torque is a consequence of the parallel connection of the spring with the motor unit, and it relaxes the need for a high torque actuator and gearbox combination at the knee.

Increasing toe clearance by active knee flexion

As was discussed above, connecting the spring in parallel with the knee actuator significantly decreases the torque required by the motor during stance. During flight, on the other hand, if the mechanical switch were not present—as in typical PEA configurations—the knee motor would have to do unnecessary work against the spring to actively flex the knee joint. In this case, achieving a desired toe clearance by shortening the leg in flight would entail additional energy cost. In the context of the

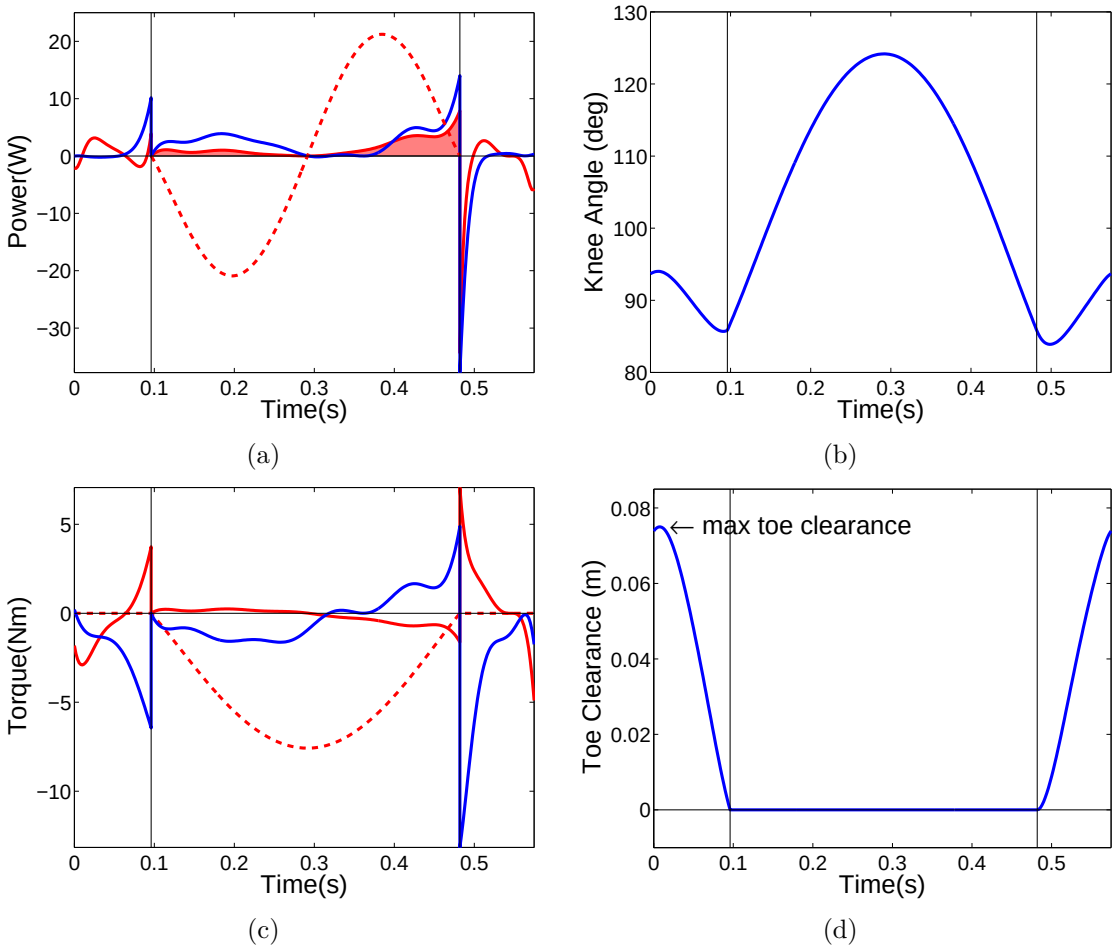

Figure 5.9: An optimized Hopping-in-place motion for 7.5cm maximum toe clearance. Vertical lines denote touchdown and liftoff. (a) Hip (blue solid), knee (red solid) and spring (red dotted) power. (b) Knee angle. (c) Hip (blue solid), knee (red solid) and spring (red dotted) torque. (d) Toe clearance. The spring power and torque in (a) and (c) is *scaled down* by a factor of five.

Sw-PEA, however, actively flexing the knee during flight does not involve the energy-storing spring and it could be a more energy-efficient way to increase the toe clearance.

To verify if this intuition is correct, we compare the energy consumption of SPEAR for different maximum toe clearances with one alternative leg model. That model has a PEA at its knee joint but no switch and will be referred as the *PEA model*. For the PEA model, u_{spring} in (5.7) is given by

$$u_{\text{spring}} = -56.67 \ \max\{(\theta_{\text{knee}} - \bar{\theta}_{\text{knee}}), 0\} \ , \tag{5.15}$$

where $\bar{\theta}_{\text{knee}}$ is the rest angle of the knee rotational spring. Due to the absence of the switch in the PEA model, $\bar{\theta}_{\text{knee}}$ cannot be adjusted; of course, the motor can modify the knee touchdown angle during flight, but such action necessarily deforms the spring. In what follows, we choose $\bar{\theta}_{\text{knee}} = 61°$ as the nominal configuration of PEA.

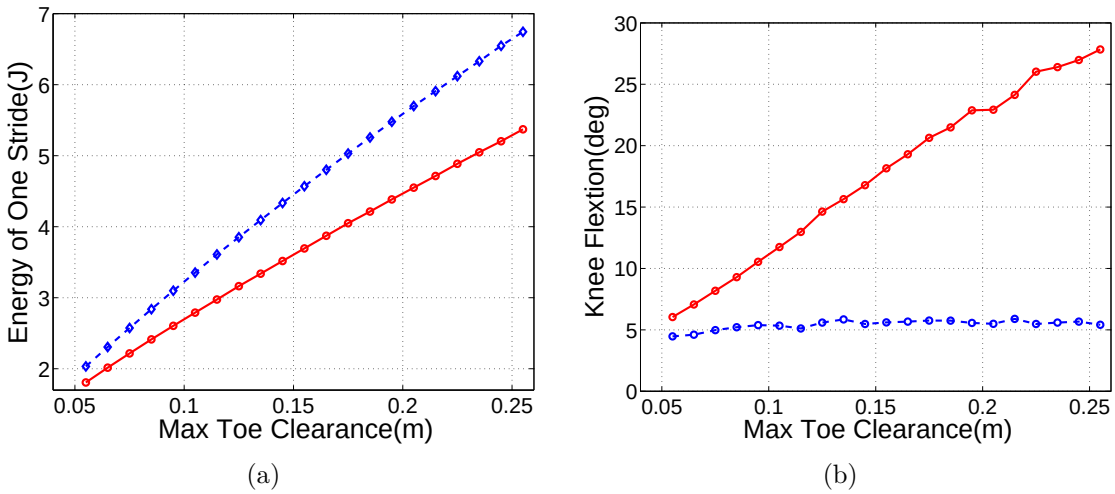

Figure 5.10: Hopping-in-place gait for the Sw-PEA (red solid line) and for the PEA leg (blue dashed line). (a): c_{ele} for different maximum toe clearance.(b): maximum contraction of the knee angle at flight phase.

Figure 5.10 presents optimized hopping-in-place gaits for both the Sw-PEA and the PEA leg models obtained for different maximum toe clearances. As Fig. 5.10(a) shows, while the energy cost is almost linearly increasing with the toe clearance, the PEA model uses 10-20% more energy than SPEAR. It can be seen in Fig. 5.10(b), that the optimizer favors motions in which the SPEAR flexes its knee joint actively in the flight phase to increase the toe clearance; this was also observed in Figs. 5.9(b)-5.9(d). The desired toe clearance is achieved by moving the relatively light shank through the knee actuator. The evolution of the knee torque shown in Fig. 5.9(c) also shows that the knee actuator first flexes the knee joint to reach the maximum clearance, then extends it to prepare for touchdown. However, the optimizer adopts a different strategy in the PEA leg model; this is due to the cost associated with flexing the knee during flight, where the knee actuator must perform work over the spring.

Adjusting leg stiffness for energy saving

As described in Section 5.1.4, the mechanical switch in the proposed Sw-PEA implementation allows for tuning the leg stiffness on a step-by-step fashion in an energy efficient way. This is simply achieved by landing at different knee angles that are specified during the flight phase. Figure 5.11 presents the results of the optimization (5.14) with $Y_{\text{toe}} = 7.5$cm for different knee touchdown angles $\Theta_{\text{knee}}^{\text{TD}}$. It can be seen that the cost is decreasing as the leg contacts the ground in a more flexed configuration that corresponds to a softer virtual spring. However, beyond a certain knee touchdown angle the energy cost starts increasing. This can be explained by the fact that for such excessively "crouched" configurations, the spring becomes too soft and the knee actuator needs to contribute to the negative work to decelerate the downward motion of the COM and prevent the leg from collapsing.

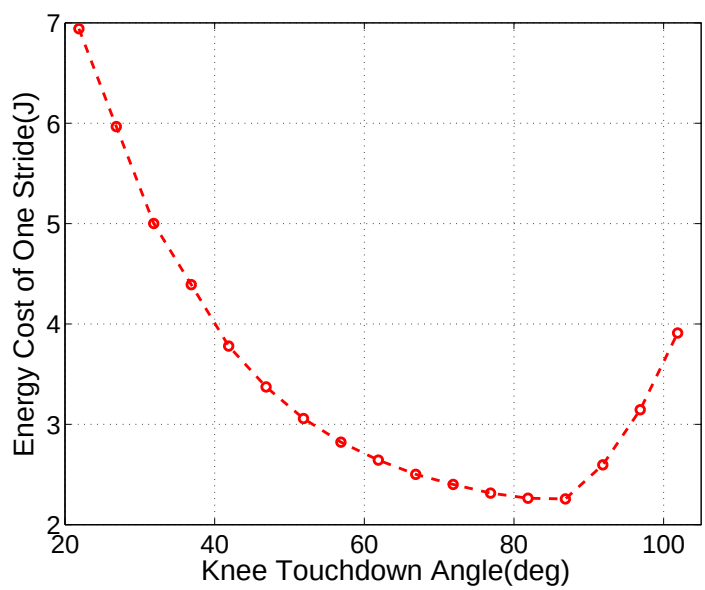

Figure 5.11: The electrical energy consumption for hopping with a fixed maximum toe clearance of 7.5cm with different touchdown angles.

5.3 Experimental Results

To evaluate the performance of the proposed implementation of a Sw-PEA, this section presents experiments with SPEAR realizing both hopping in place and forward running motions.

5.3.1 Hopping Controller

Similar to [69], the controller used here to stabilize hopping in place and running forward motions on the SPEAR is organized on two levels, as shown in Fig. 5.12. On the first level, a continuous-time feedback control law is used to apply desired torques to the hip and knee actuators during stance and to realize the desired landing configuration during flight. On the second level, the parameters introduced by the continuous-time controller are updated in an event-based fashion to regulate hopping height and and forward velocity.

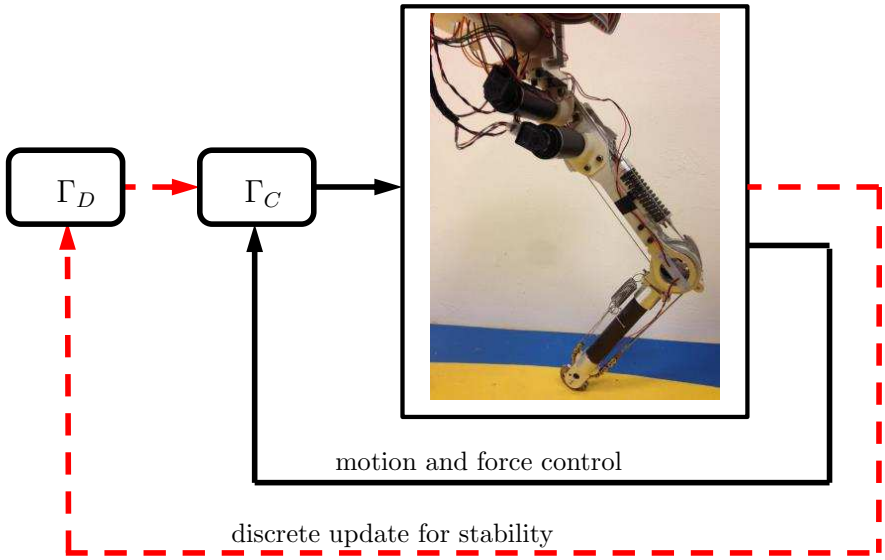

Figure 5.12: The framework of the controller used for experiments.

Continuous-time control

During stance, the continuous-time controller applies desired torques—instead of trajectories—at the knee and hip joints, with the objective of injecting energy in the system in a way that "preserves" the natural compliance of the leg. For simplicity in parameter tuning, the torque applied at the knee during stance is given by

$$\tau_{\text{knee}}(t) = \begin{cases} u_{\text{knee}}, & \text{if } t - t_{\text{TD}} < \frac{\bar{T}_{\text{st}}}{2} \\ -u_{\text{knee}}, & \text{if } t - t_{\text{TD}} \geq \frac{\bar{T}_{\text{st}}}{2} \end{cases} \tag{5.16}$$

where u_{knee} is constant over a step but can vary from one step to the next, as will be explained below—and t_{TD} is the touchdown instant of the current step, and $\bar{T}_{\text{st}}$ is a constant that captures, on average, the duration of the stance phase at a given speed. The prescription (5.16) ensures that the knee actuator performs mainly positive work, injecting energy by further compressing the spring S_1 during the first half of the stance phase and assisting with spring recoil during the second half in preparation for takeoff. Finally, throughout stance the hip actuator applies a constant torque

$$\tau_{\text{Hip}}(t) = \bar{\tau}_{\text{Hip}} \ , \tag{5.17}$$

with the intention of reducing the chance of slipping.

During flight, on the other hand, the objective of the controller is to drive the leg to a desired configuration prior to landing. This is achieved by specifying desired target angles $\bar{\theta}_{\text{knee}}$ and $\bar{\theta}_{\text{hip}}$ for the knee and hip joint, respectively. Note that $\bar{\theta}_{\text{knee}}$ specifies the rest position of the knee joint compliance and thus the equivalent stiffness of the virtual leg connecting the foot with the hip, while both angles $(\bar{\theta}_{\text{knee}}, \bar{\theta}_{\text{hip}})$ are needed to specify the touchdown angle γ defined in Fig. 5.2(b), which can be used to regulate forward velocity. With the ability to switch off the energy-storing spring during flight, the target joint angles are achieved simply, by using a Linear Quadratic Regulator (LQR) on a second-order approximation of the input/output dynamics of each of the hip and knee joints, assuming that the coupling between them is small.

Event-based control

The parameters introduced by the continuous-time control law are updated in an event-based fashion to stabilize the motion. In more detail, to regulate hopping height, the parameter $\bar{\tau}_{\text{knee}}$ in (5.16) is updated at the apex height of the k-th step based on feedback from the current hopping height $y[k]$ as follows

$$u_{\text{knee}}[k] = \bar{\tau}_{\text{knee}} - c_1(y[k] - \bar{y}) \ , \tag{5.18}$$

where $\bar{\tau}_{\text{knee}}$ and $\bar{y}$ are the nominal (desired) values of the knee torque and apex height, respectively, and c_1 is a positive gain.

To regulate the forward velocity, the touchdown angle γ of the virtual leg connecting the foot and the hip joint—see Fig. 5.2(b)—is updated according to a modified version of Raibert's velocity controller [74] as

$$\gamma[k] = \bar{\gamma} + c_2(\dot{x}_{\text{cm}}[k] - \bar{\dot{x}}_{\text{cm}}) \ , \tag{5.19}$$

where $\dot{x}_{\text{cm}}$ and $\bar{\dot{x}}_{\text{cm}}$ are current and nominal values of the horizontal velocity of the COM at the apex height of the k-th step, $\bar{\gamma}$ is the nominal touchdown angle and c_2 is a positive gain. To realize $\bar{\gamma}$ in (5.19), different combinations of $(\bar{\theta}_{\text{knee}}, \bar{\theta}_{\text{hip}})$ can be used. As was described in Section 5.1.4, $\bar{\theta}_{\text{knee}}$ determines the stiffness of the virtual leg during the subsequent stance phase, and has a great influence both on the stability and energy efficiency of the motion; its effect will be briefly explored in Section 5.3.3 below. Given $\bar{\theta}_{\text{knee}}$ and $\bar{\gamma}$ the target value of $\bar{\theta}_{\text{hip}}$ can then be computed easily, and the continuous-time flight controller can be applied to achieve the target touchdown values of the knee and hip joint angles.

Implementation details

To implement the controller, first the flight controller's LQR gains are computed to obtain a sufficiently fast step-response when the legs is not in contact with the ground. Then, the values of the parameters

$$\alpha = \{\bar{\tau}_{\text{hip}}, \bar{\tau}_{\text{knee}}, \bar{\gamma}, \bar{\theta}_{\text{knee}}, \bar{T}_{\text{st}}\} \tag{5.20}$$

corresponding to desired nominal forward velocity $\dot{\bar{x}}_{\text{cm}}$ and hopping height $\bar{y}$ are specified through experiments. The gains c_1 and c_2 are then tuned to achieve a stable motion. In implementing (5.19), the average velocity after liftoff instead of the instantaneous one is used for $\dot{x}_{\text{cm}}$ to filter out the noise. Finally, to start hopping, an initialization step is involved. Similar to the stance controller (5.16), the leg first bends its knee with its maximum torque to store energy in the spring, then, when the leg reaches its minimum height, the knee motor inverts its torque to push against the ground to begin hopping.

5.3.2 Leaping

The mobility of a legged robot is largely related to the height its toe can clear during flight. The proposed Sw-PEA can increase toe clearance in two different ways. First, as indicated by the stance phase knee controller (5.16), the actuator can inject energy into the spring during the first half of the stance phase compressing it further, much like loading a catapult mechanism. With this energy released later during stance, a much larger vertical liftoff velocity can be achieved causing the COM of the system to reach a higher position. Second, the leg is able to flex its knee freely during flight without interfering with the parallel spring, thereby further increasing the maximum toe clearance; see [52, Section VI] for a detailed simulation analysis.

To demonstrate SPEAR's vertical jumping capability, two sets of leaping experiments are carried out, one with active knee flexion and one without. In both experiments, an initialization step is used, after which the controller (5.16) is engaged with $\bar{\tau}_{\text{knee}} = 12.4\text{Nm}$, the maximum torque the actuator can provide within the specified current limit (approximately 12A). The results are presented in Fig. 5.13, in which it is seen that without active knee flexion during flight the robot can jump with a toe clearance of 14cm, corresponding to 25% of the leg's rest length. With active knee flexion, on the other hand, the leg is shortened during flight and SPEAR reaches a 25cm toe clearance, corresponding to 45% of the leg's rest length with the vertical height of the hip joint virtually unchanged.

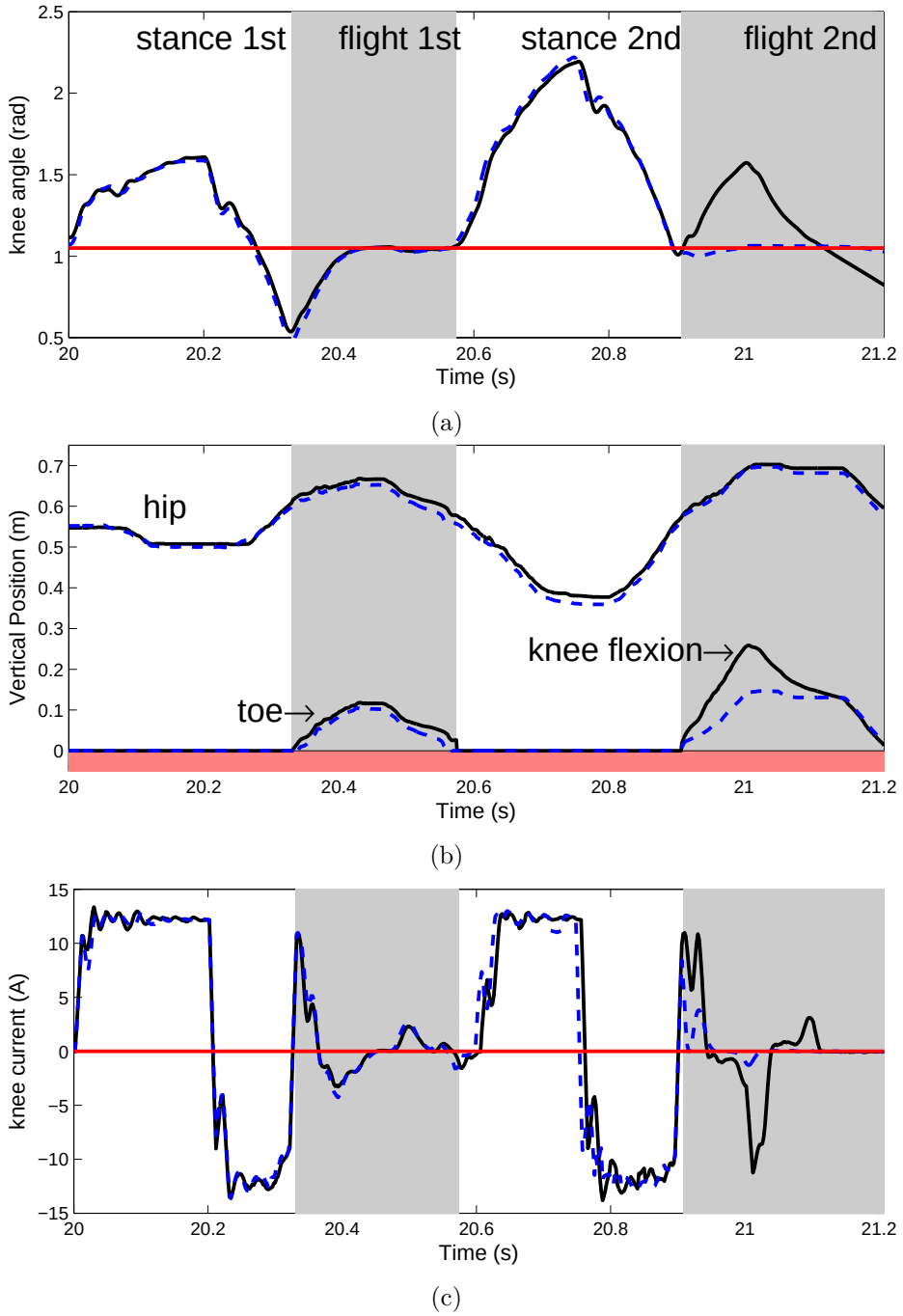

Figure 5.13: The gray area is the flight phase. At the second stride, the knee of one experiment actively flexed to increase toe clearance. (a) The knee angle. The red line is the touchdown angle (rest angle) of the knee spring. (b) Toe and COM vertical position. (c) Knee actuator input.

In both experiments, the contribution of the parallel spring during stance is significant. For example, in the initialization step, when the knee spring is deformed about 0.5rad the corresponding spring toque is 27Nm, about 2.3 times larger than the maximum torque 12.4Nm that can be delivered by the knee actuator given the current limit of 12A. This advantage is typical of PEA designs. However, in these designs the energy-storing spring is always engaged, causing the actuator to perform unnecessary work during flight to actively bend the knee. As was detailed in [52, Section VI], the additional energy cost associated with active knee flexion during flight in PEAs may render this strategy for ensuring sufficient toe clearance inefficient. By way of contrast, the proposed Sw-PEA combines the advantages of the parallel spring during stance with unobstructed knee joint control during flight to achieve sufficient toe clearance, thereby enhancing mobility without compromising efficiency.

5.3.3 Periodic Hopping in Place

Figure 5.14 presents the vertical displacement of the hip joint during a hopping in-place experiment. The initialization procedure is employed during the first hop, and then the controller of Section 5.3.1 is engaged. It can be seen that, after a short period, the controller is successful in stabilizing the leg to a periodic hopping motion.

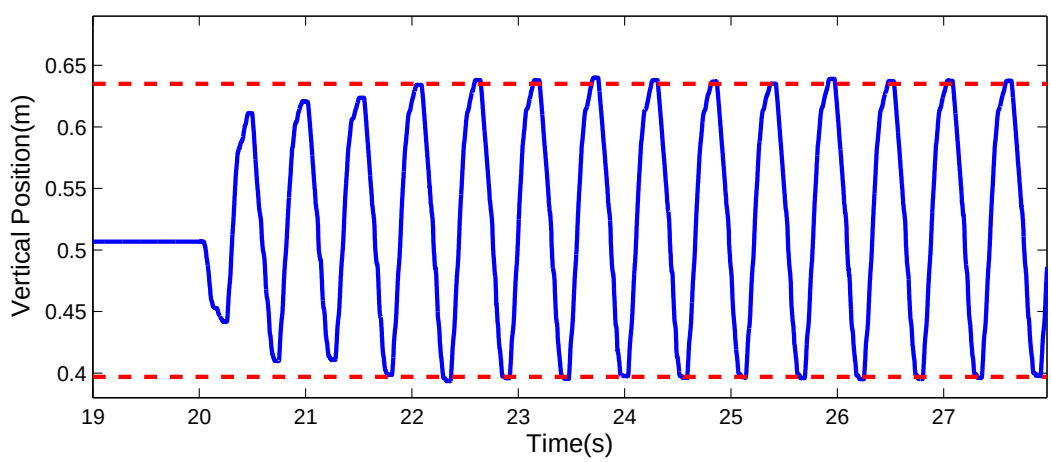

Figure 5.14: Vertical displacement of the hip for the hopping in place experiment.

The evolution of certain variables of interest in one hopping cycle is presented in Fig. 5.15. It can be seen from Fig. 5.15(a) that at the middle of the stance phase the knee spring achieves its maximum deformation of 0.8rad, corresponding to about 18J of mechanical energy. By integrating the sampled data, it can be found that the actuators inject only about 4.6J of mechanical energy during the first half of the stance phase, indicating that part of the gravitational potential energy and kinetic energy is stored in the spring S_1. To quantify the contribution of the spring, the hopping efficiency η_{hop} can be defined as

$$\eta_{\text{hop}} := 1 - \frac{W^+_{\text{motor}}}{W^+_{\text{motor}} + W^+_{\text{spring}}} \quad , \tag{5.21}$$

where W^+_{motor} and W^+_{spring} represent the positive work done by the motors and the spring, respectively, computed by

$$\begin{aligned} W^+_{\text{motor}} &= \sum_{i \in \{\text{knee,hip}\}} \int_0^T \max(\tau_{\text{m},i} \cdot \dot{\theta}_{\text{m},i}, 0) dt \\ W^+_{\text{spring}} &= \int_0^T \max(\tau_{\text{spring}} \cdot \dot{\theta}_{\text{knee}}, 0) dt \quad , \end{aligned} \tag{5.22}$$

where t is the duration of the stride, $\tau_{\text{m},i} = K_{\text{T}} \cdot I_i$ is the torque delivered at the shaft of the i-th motor, $i \in \{\text{knee}, \text{hip}\}$ when current I_i flows in its coil and $\dot{\theta}_{\text{m},i}$ the corresponding shaft velocity. In (5.22), τ_{spring} is the torque developed by the spring computed by (5.6) and $\dot{\theta}_{\text{knee}}$ the knee joint rotational velocity. The efficiency η_{hop} proposed in [41] measures how much of the positive mechanical work in one hopping stride is recycled. For this gait, (5.21) results in $\eta_{\text{hop}} = 0.642$, implying that 64% of the positive mechanical energy in one stride is generated by the spring.

Figures 5.15(c)–5.15(d) show that the parallel spring reduces both the torque and power requirements of the motor. During stance, the spring produces most of the torque required at the knee, equal to approximately 44Nm at its maximum deformation, while the motor only contributes approximately 5.7Nm corresponding to the applied current 5.5A. This confirms the prediction of the optimization in [52]. Furthermore, the power of the knee motor reaches its peak of 80W (mechanical), which is significantly lower than the power associated with the spring S_1, i.e., −200W in compression and

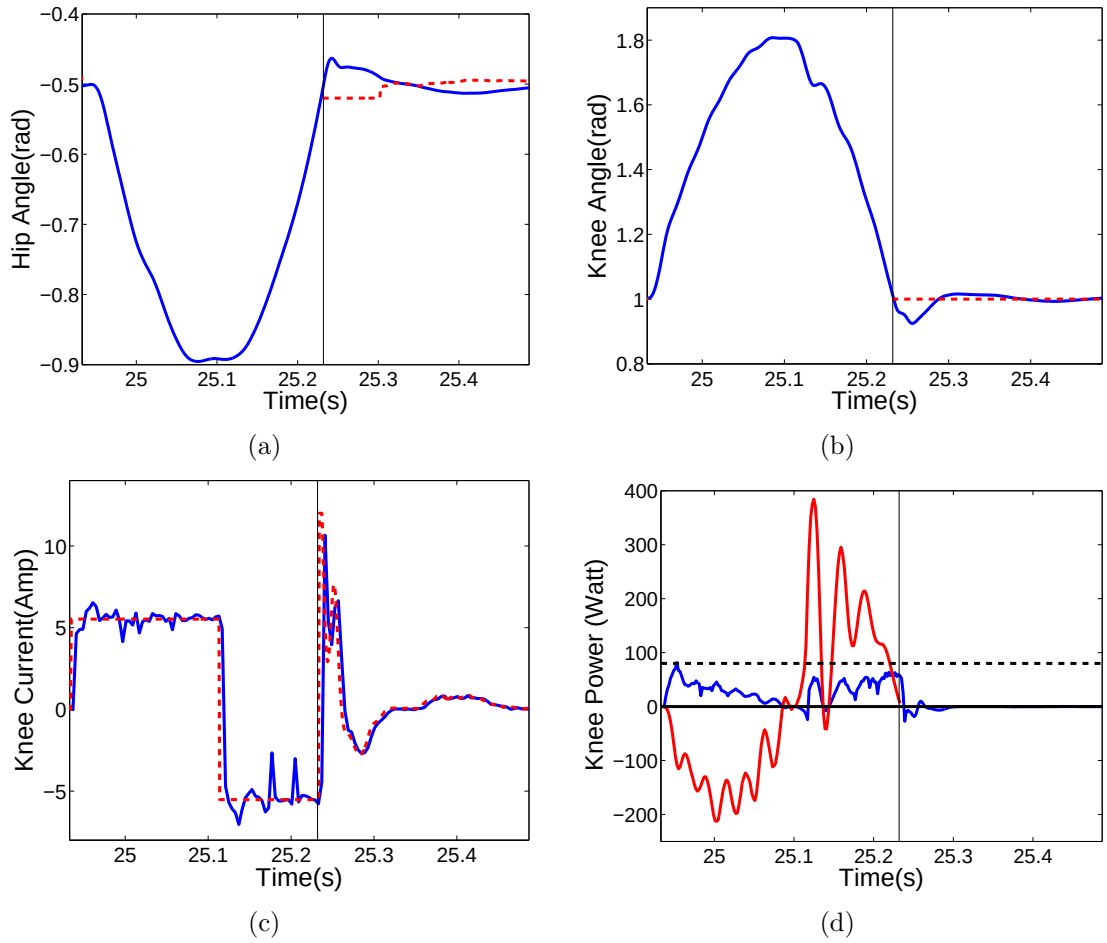

Figure 5.15: Experimental results of hopping in place. The red dotted line is the reference signal. The vertical lines stands for the liftoff event. (a) Hip angle. (b) Knee angle. (c) The current of the knee actuator. (d) The power of knee motor (blue line) and the spring (red line) at one stride.

400W in decompression. Finally, note that during stance the knee motor performs positive work due to the controller (5.18).

To investigate the effect of varying leg stiffness on the energy required to maintain the motion, three hopping experiments have been conducted, each corresponding to a different target value of the knee angle at touchdown. As was explained in Section 5.1.4, landing with different knee angles effectively changes the stiffness of the virtual leg connecting the foot with the hip. Figure 5.16 presents the results corresponding to the values 0.74rad, 1.07rad, and 1.4rad of the angle $\bar{\theta}_{\text{knee}}$, while keeping

the maximum toe clearance at 0.08m. It can be seen from Fig. 5.16(a) that the leg uses less energy during a stride when landing with more straight leg configurations, in which, as Fig. 5.16(b) shows, the virtual spring between the foot and the hip becomes stiffer. Note that this relationship between the stiffening of the leg and the decrease in energy consumption is due to the specific operating conditions considered here; in general, there is an optimal leg stiffness that results in minimum energy consumption, as discussed in [38].

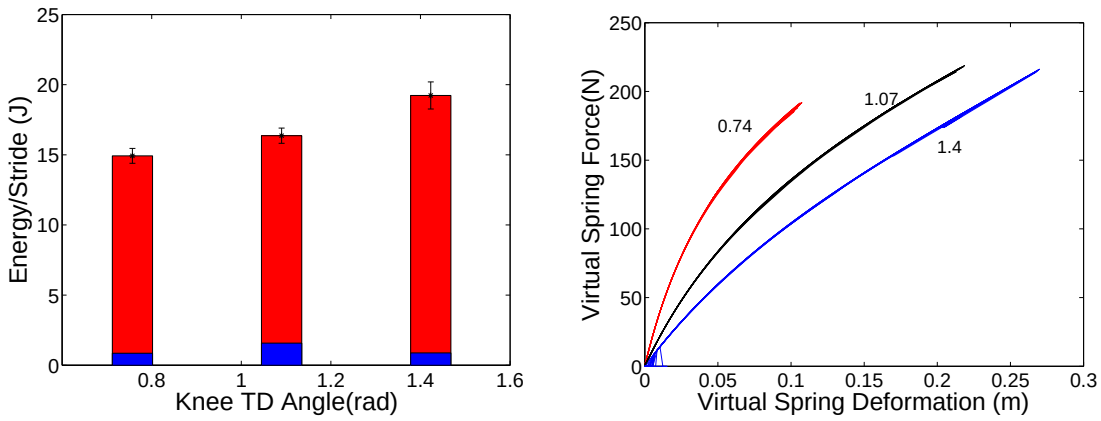

(a) (b)

Figure 5.16: (a) Electrical energy consumption for hopping-in-place with different touchdown angles. (b) Virtual leg stiffness for the knee touchdown angles in (a). Landing at more straight leg configurations results in stiffer springs which correspond to reduced energy consumption.

5.3.4 Periodic Running Forward

Modifying the value of $\bar{\dot{x}}_{\text{cm}}$ in (5.19) and the parameters associated with the controller, running motions with forward velocities ranging from 0.1m/s to 0.5m/s have been realized. Experimental results for one such experiment corresponding to speed 0.14m/s are presented in Fig. 5.17. Similarly to the hopping-in-place experiments of Section 5.3.3, the knee spring S_1 recycles part of the mechanical energy during the stance phase, keeping the power requirements of the knee motor small. This can

be seen in Fig. 5.17(d), which is similar to what was observed in the hopping-in-place experiments. Compared with hopping in place, running forward results in larger deformations of the knee spring and higher amplitude of the vertical oscillation.

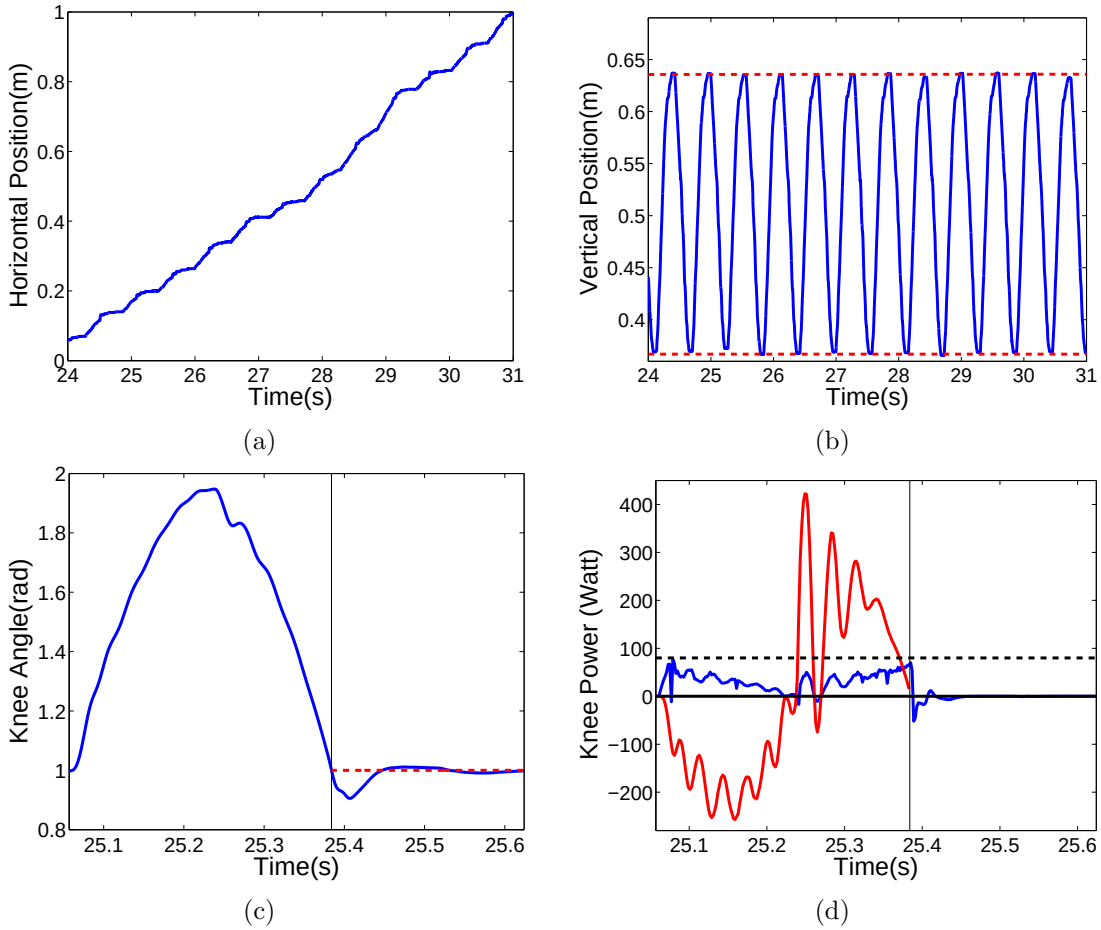

Figure 5.17: Experimental results of a forward hopping gait with average velocity of 0.14 m/s. (a) The horizontal displacement of the hip. (b) The vertical displacement of the hip. (c) Knee angle; the red dotted line is the reference position. (d) The power of knee motor (blue line) and the spring (red line) at one stride. The vertical lines in (c) and (d) represents the liftoff event.

To characterize the performance of SPEAR in terms of energy economy, the cost of transport (COT) at different velocities is computed on the basis of experimental data. The COT measures the amount of energy required to transport a unit weight over a

unit distance [48]; mathematically,

$$\mathrm{COT} = \frac{W}{Mg\Delta x_{\mathrm{cm}}} \ , \tag{5.23}$$

where M is the total mass of the robot, Δx_{cm} is the forward distance travelled, and W is the energy consumed for traveling that distance. Depending on how W is defined in (5.23), different energy costs can be computed, revealing different aspects of how energy is utilized by the system. In the case of positive mechanical cost of transport $\mathrm{COT}^{+}_{\mathrm{me}}$, W in (5.23) corresponds to the positive mechanical work of the motors,

$$W = W^{+}_{\mathrm{motor}} \ , \tag{5.24}$$

where W^{+}_{motor} has been defined in (5.22). To take into account both positive and negative mechanical work, $\mathrm{COT}_{\mathrm{me}}$ is also used, with W in (5.23) given by

$$W = \sum_{i \in \{\mathrm{knee,hip}\}} \int_0^T \mathrm{abs}(\tau_{\mathrm{m},i} \cdot \dot{\theta}_{\mathrm{m},i}) dt \ , \tag{5.25}$$

where T, $\tau_{\mathrm{m},i}$ and $\dot{\theta}_{\mathrm{m},i}$ have the meaning discussed in (5.22). Clearly, if the difference between (5.24) and (5.25) is small, the negative work performed by the motors is small, implying that the controller makes effective use of the mechanical system in sustaining the motion. This is the case for SPEAR, as can be seen from Fig. 5.18(a), which shows that the mechanical COTs computed based on (5.24) and (5.25) are close. Hence, the energy-storing spring S_1 does most of the negative work associated with locomotion—particularly during the compression part of the stance phase—and the motors contribute by providing mostly positive work to regulate the motion. According to Fig. 5.18(a), the mechanical cost of transport $\mathrm{COT}^{+}_{\mathrm{me}}$ of SPEAR decreases as the running speed increases, and

$$\mathrm{COT}^{+}_{\mathrm{me}} = 0.45 \tag{5.26}$$

is the lowest value achieved at the highest speed 0.54m/s.

The COT (5.23) defined on the basis of mechanical energy focuses on the locomotion task from an "output" perspective, without considering the actuation technology

used to input energy in a specific system. As such, the mechanical COT does not capture the total energy required to sustain locomotion. In the context of the electrically actuated SPEAR, the total cost of transport $\mathrm{COT}_{\mathrm{ele}}$ can be computed with W in (5.23) given as in [105] by the equation

$$\begin{aligned} W_{\mathrm{ele}} &= \sum_{i\in\{\mathrm{knee,hip}\}} \int_0^T \max\{(V_i I_i), 0\} dt \\ &= \sum_{i\in\{\mathrm{knee,hip}\}} \int_0^T \max\{(I_i^2 R_i + \tau_{\mathrm{m},i} \cdot \dot{\theta}_{\mathrm{m},i}), 0\} dt \ , \end{aligned} \tag{5.27}$$

where V_i and I_i are the supply voltage and current at the terminals of the i-th motor, R_i is the motor's terminal resistance, and $\tau_{\mathrm{m},i}$ and $\dot{\theta}_{\mathrm{m},i}$ have the meaning described above. The cost (5.27) captures the energy at the input of the motors[1], as shown in Fig. 5.3. As can be seen in Fig. 5.18(a), the performance is best when the robot runs at its highest speed 0.54m/s, where

$$\mathrm{COT}_{\mathrm{ele}} = 0.86 \ . \tag{5.28}$$

This value is smaller than the $\mathrm{COT}_{\mathrm{ele}}$ in [40], in which SEAs are employed, but still about 70% larger than the corresponding value for the MIT cheetah that uses customized high torque-density motors and regenerative braking [91].

Figure 5.18(a) also shows that the ratio $\mathrm{COT}_{\mathrm{me+}}/\mathrm{COT}_{\mathrm{ele}}$ over the range of speeds reported is about 50%, which is a rough indicator of the efficiency by which electrical energy is transformed to mechanical energy in SPEAR. This is evident from Fig. 5.18(b), which shows that nearly half of the electrical energy input to the motors, as computed by (5.27), is lost due to Joule heating; the hip motor does not contribute much to the energy lost due to the small torques developed at the hip. Regarding the knee joint, as was mentioned in Section 5.1.3, inserting the spring in parallel with the actuator decreases the torque required by the knee motor, thereby reducing the

[1] Note that $\mathrm{COT}_{\mathrm{ele}}$ does not include the energy consumption due to the CPU, the motor driver logic and the wireless router, which are powered separately, as shown in Fig.5.7.

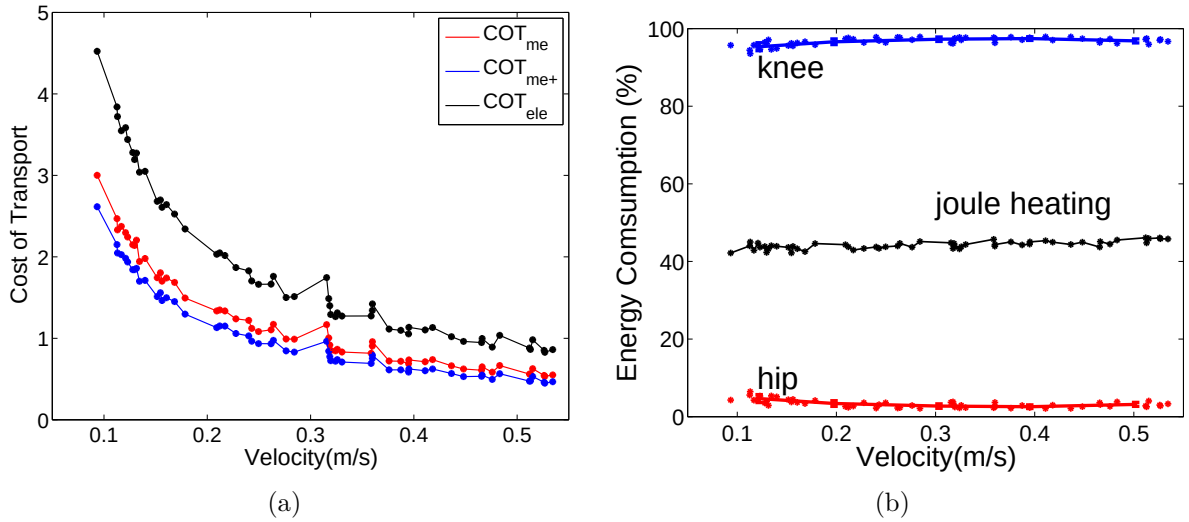

Figure 5.18: (a) The COT of SPEAR for forward speeds ranging from 0.1m/s to 0.54m/s. Each point corresponds to a running experiment at a commanded speed $\dot{\bar{x}}_{\mathrm{cm}}$, and represents the COT averaged over 10 steady-state strides. (b) The energy consumption of the knee and hip joints, as well as Joule heating of the two motors.

energy dissipated due to Joule heating at the coils of the knee motor. In the absence of springs, the energy lost due to Joule heating at the knee motor would have been much higher. Finally, Fig. 5.19 places SPEAR amongst alternative robotic designs in terms of $\mathrm{COT}_{\mathrm{ele}}$; it can also be seen that SPEAR's $\mathrm{COT}_{\mathrm{ele}}$ is on the line of land animals.

5.4 Conclusion

In this chapter, we present the working principle of the Switchable Parallel Elastic Actuator (Sw-PEA), as well as SPEAR, a monoped leg which is used to evaluate the concept in the field of legged locomotion. Using a passive mechanical switch at the foot, the spring at the knee joint is engaged at stance phase to support body weight and is disengaged at flight phase to allow precise motion control. The design is compact and reliable, and can be easily scaled for heavier robots. The proposed design improves the efficiency of legged locomotion both by recycling mechanical energy and by reducing the torque of the joint, which is demonstrated both by numerical simulations and experimental results. The proposed design allows a convenient way to adjust the

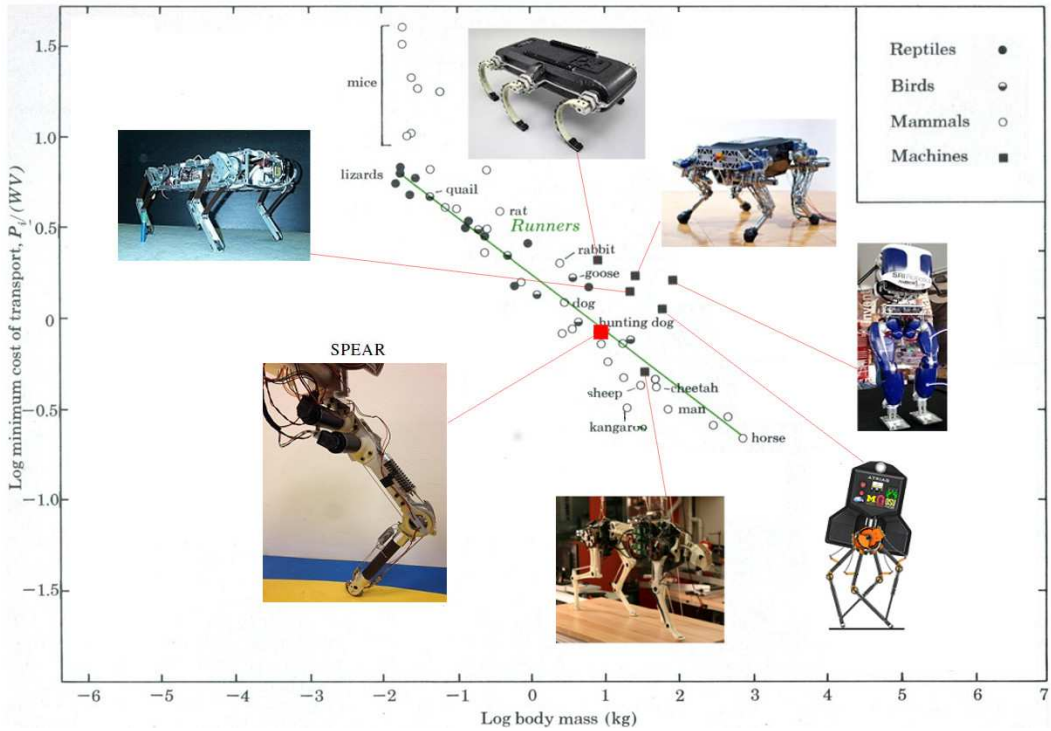

Figure 5.19: The cost of transport for a variety of robots and land animals. Figure adapted from [92] with additional robot values from [10, 36, 40, 72, 81].

stiffness property of the two-segment leg. This property of the leg is found to have important influence on the energy consumption of the leg. As demonstrated by the leaping experiment, this Sw-PEA design does not sacrifice the mobility of the robot.

Chapter 6

CONCLUSIONS AND FUTURE WORK

6.1 Conclusions

Compliant elements exist in the muscles and tendons of biological systems, and they play important roles in human and animal running gaits. The objective of this thesis is to develop running robots that combine mobility and efficiency through compliant elements, which can be introduced mechanically—passive compliance—or via the control system—active compliance. In this thesis, running controllers are developed for models of increasing complexity and their stability properties are analyzed. In addition, a novel actuation mechanism for running robots is proposed and evaluated in both simulations and experiments.

This thesis begins with reduced-order models for monopedal and quadrupedal running gaits. Albeit simple, these models are able to characterize the fundamental principles of human and animal running. Analytic conclusions on stability are obtained for these models by exploiting the reversing symmetries of the underlying vector field. For the monopedal running model, a hierarchical controller is proposed. By regulating the torso using a finite-time controller and by selecting appropriate touchdown angles, the controller leads to analytically provable neutrally stable periodic gait. For the quadrupedal bounding model, a necessary condition for gait stability is obtained, which is later used to facilitate the selection of control parameters. Numerical simulations demonstrate the analytic results and the performance of the controller.

Inspired by the existence of passively stable bounding gaits in compliant quadruped running models, this thesis proposed a bounding controller for a detailed sagittal plane model of the Hydraulic Quadruped (HyQ) robot, designed and constructed by the Italian Institute of Technology. The controller combines elements of hybrid zero dynamics

control with force planning to coordinate the joints of the robot to mimic the behavior of a passively compliant quadruped. By creating active compliance in the support leg, and by controlling the touchdown angle of the swing leg, stable periodic gaits emerge as the interaction between the low-order system with the environment. The controller is demonstrated to be robust to ground height variations and parameter inaccuracy.

In the last part of this thesis, based on our analysis of passive and active compliant systems, the concept of switchable parallel elastic actuation (Sw-PEA) is proposed as way to enhance mobility without sacrificing efficiency. A mechanical switch is introduced in a parallel elastic actuation configuration to engage the spring only when it is needed, that is, during stance. The switch is placed at the food of the robot, where the ground reaction force is used to automatically engage and disengage the spring. The performance of the mechanism is tested by the monopedal robot SPEAR, which incorporates a Sw-PEA for its knee joint. Experiments demonstrate that Sw-PEA reduce the energy consumption without impairing the mobility of the robot.

6.2 Future Work

6.2.1 Symmetry Controller for Biped Running

In Chapter 3, a symmetry based controller is proposed for the ASLIP model. This controller works on the Hamiltonian system, offering analytically tractable stability conclusions. However, due to impact and friction in physical systems, this controller is not expected to work for models with energy dissipation: the system energy will continuously decrease until the robot stops or falls. In addition, the controller would only make the system neutrally stable: disturbances would shift the system to different operating conditions without it begin able to attenuate them.

To apply this controller on physical robots, modifications are necessary. One possible modification would be to add extra layers to regulate the energy and velocity of the system, so that the energy lost due to impacts and/or due to disturbances are compensated. A similar approach has been proposed in [42] to stabilize a bipedal walker. The control design took three steps: first, the dissipativity of the system is

neglected and a controller is proposed for this reduced-order model; then, a energy controller is add on top to stabilize the periodic gait; last, an adaptive layer is added to reduce control effort. By using the inclination of the torso (which adds asymmetry), energy is injected into the biped to stabilize the walking velocity.

A similar strategy has also been used to stabilize bounding gaits for the quadrupedal model studied in Section 3.3. Two extra layers are added to make the periodic gait asymptotically stable. To regulate the system's energy, two actuators are introduced at the hip joints of the posterior and the anterior legs of the bounding model introduced in Section 3.1.2. Each actuator acts only when the corresponding leg is on the ground, and delivers torques computed according to the prescription

$$\tau = -K \, \frac{E - \bar{E}}{\Delta\bar{\varphi}}, \tag{6.1}$$

where $\Delta\bar{\varphi}$ is a constant, corresponding to the change of the stance leg angle φ relative to the torso at the fixed point; E is the total energy and $\bar{E}$ is the nominal value at the fixed point, and $K \in [0, 1]$, controls the converging rate. This energy-level controller can be considered as a transit action since its effect would be zero after the energy of the system is stabilized.

To prevent the system from converging to a nearby fixed point within the same energy level instead of the desired fixed point, the posterior leg touchdown angle controller (3.69) can be modified to include a "symmetry-breaking" term, as follows

$$\gamma_{\mathrm{p}}^{\mathrm{td}}[n] = -\gamma_{\mathrm{a}}^{\mathrm{lo}}[n] + K_{\mathrm{vel}}(\bar{\dot{x}}_{\mathrm{cm}} - \dot{x}_{\mathrm{cm}}). \tag{6.2}$$

where K_{vel} is a gain multiplying the error between the nominal (fixed point) $\bar{\dot{x}}_{\mathrm{cm}}$ and the current velocity $\dot{x}_{\mathrm{cm}}$.

Figure 6.1 presents the performance of the controller under control laws (3.78), (6.1) and (6.2). The control coefficients are chosen as $c = 0.1$, $K = 0.1$ and $K_{\mathrm{vel}} = 0.05$. Linearization of the Poincaré return map gives a dominant eigenvalue of 0.89, suggesting that the fixed point is locally exponentially stable.

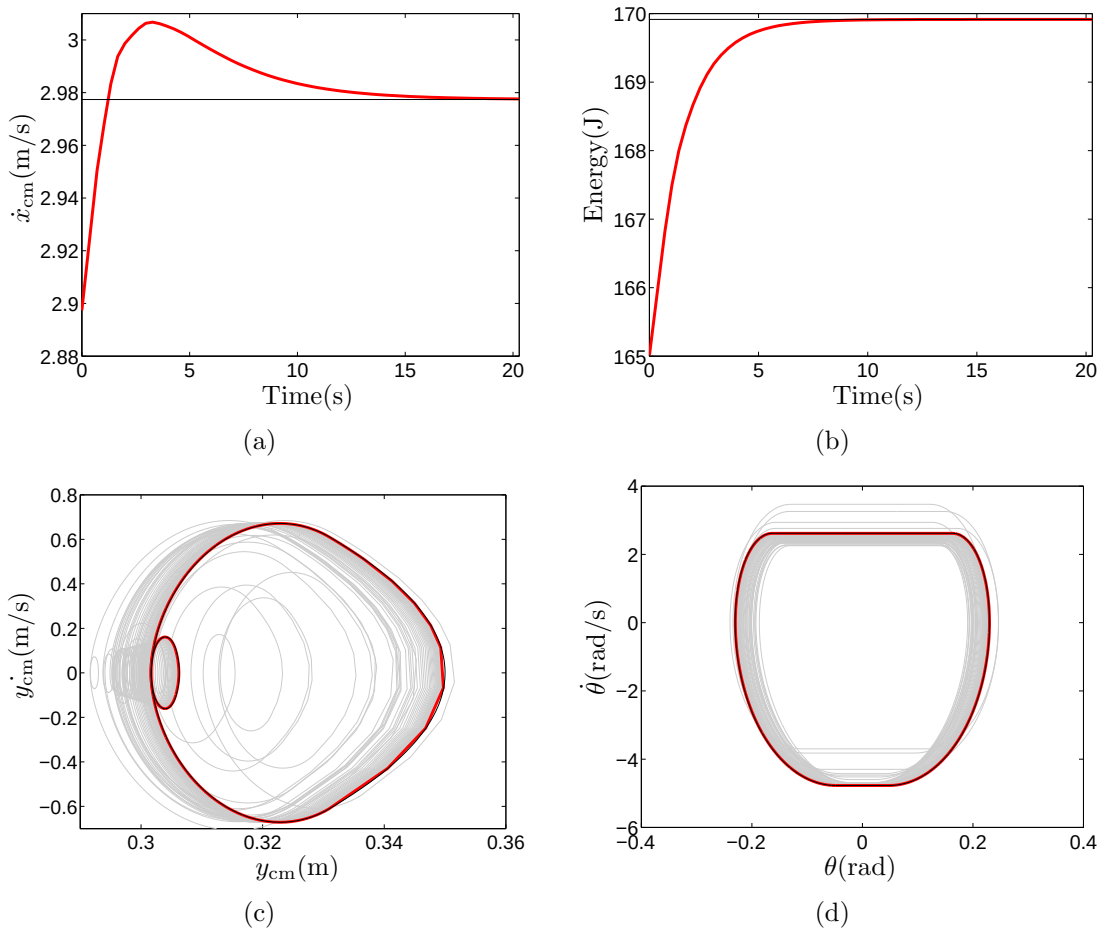

Figure 6.1: Response of the bounding model under a 0.08m/s disturbance in $\dot{x}_{\mathrm{cm}}$. The black lines corresponds to nominal values. Figure 6.1(a) and Fig. 6.1(b) are the horizontal velocity and total energy at the Poincaré section. Figure 6.1(c) and Fig. 6.1(d) are the phase plot of the state variables.

6.2.2 Quadruped Design and Evaluation

Another direction for future research concerns the use of the SPEAR leg as a building block toward the design of a quadrupedal robot. Compared with bipedal robot, robotic quadrupeds offer a good tradeoff among stability, load-carrying capacity and mechanical complexity; thus, they offer an attractive solution to applications that require enhanced mobility and versatility.

Figure 6.2 presents a 3D model of a quadrupedal robot, which is being developed at the Robotic Locomotion Laboratory of the University of Delaware. Using SPEAR as

a prototype, each leg has three degrees of freedom, namely, hip adduction/abduction, hip flexion/extension, and knee flexion/extension. The torque from the knee actuator is transferred to the joint using a timing belt. The flexion of the timing belt offers additional protection to the motor and gearbox. With one more joint on each leg, the robot can be used as a platform to test different algorithms. It should be mentioned that the controller proposed in Chapter 4 can be modified for this robot by removing the active compliance term in (4.7) and (4.8).

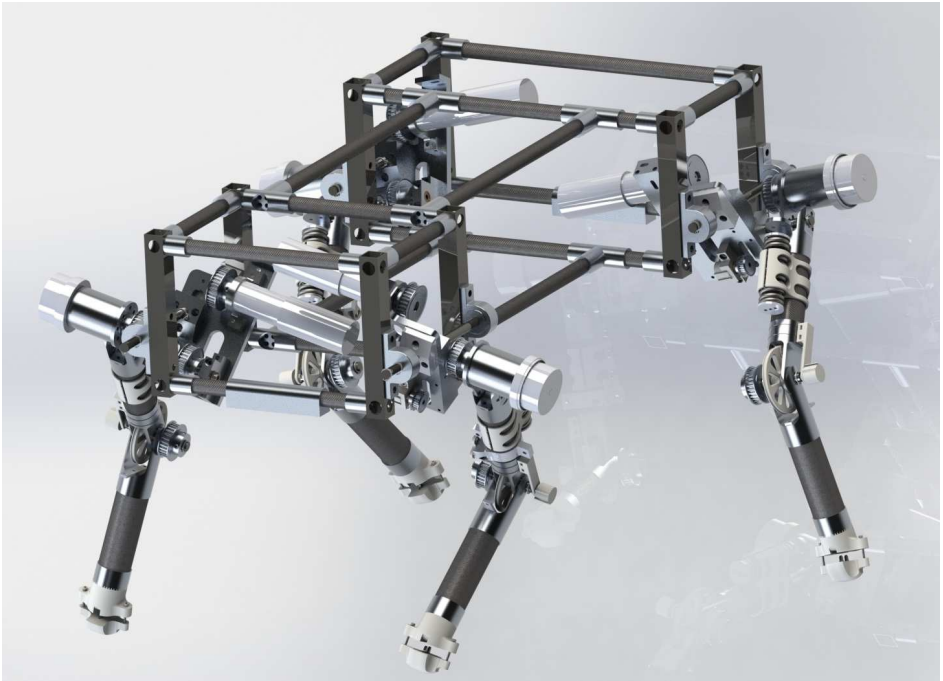

Figure 6.2: 3D Model of a quadruped. Each leg of the robot is similar to SPEAR, but with three DOFs per leg: hip adduction/abduction, hip flexion/extension, and knee flexion/extension. The additional hip adduction/abduction joint makes the robot more suitable for exploration tasks.

BIBLIOGRAPHY

[1] R. McN. Alexander. Three uses for springs in legged locomotion. *The International Journal of Robotics Research*, 9(2):53–61, 1990.

[2] R. Altendorfer, D. E. Koditschek, and P. Holmes. Stability analysis of legged locomotion models by symmetry-factored return maps. *The International Journal of Robotics Research*, 23(10-11):979–999, 2004.

[3] R. Altendorfer, D. E. Koditschek, and P. Holmes. Stability Analysis of a Clock-Driven Rigid-Body SLIP Model for RHex. *The International Journal of Robotics Research*, 25(4):343–358, 2006.

[4] A. Ananthanarayanan, M. Azadi, and S. Kim. Towards a bio-inspired leg design for high-speed running. *Bioinspiration & Biomimetics*, 7(4):1–12, 2012.

[5] S. P. Bhat and D. S. Bernstein. Finite-time stability of homogeneous systems. In *Proceedings of the American Control Conference*, pages 2513–2514, Albuquerque, New Mexico, Jun. 1997.

[6] S. P. Bhat and D. S. Bernstein. Finite-time stability of continuous autonomous systems. *SIAM Journal on Control and Optimization*, 38(3):751–766, 2000.

[7] R. Blickhan. The spring-mass model for running and hopping. *Journal of Biomechanics*, 22(11-12):1217–1227, 1989.

[8] T. Boaventura, C. Semini, J. Buchli, M. Frigerio, M. Focchi, and D. G. Caldwell. Dynamic torque control of a hydraulic quadruped robot. In *Proceedings of the IEEE International Conference on Robotics and Automation*, pages 1889–1894, St. Paul, Minnesota, May 2012.

[9] W. R. Brown and A. G. Ulsoy. A maneuver based design of a passive-assist device for augmenting active joints. *Journal of Mechanisms and Robotics*, 5(3):1–11, 2013.

[10] D. Campbell and M. Buehler. Preliminary bounding experiments in a dynamic hexapod. In *Experimental Robotics VIII*, pages 612–621. Springer, New York, NY, 2003.

[11] Q. Cao and I. Poulakakis. Quadrupedal bounding with a segmented flexible torso: passive stability and feedback control. *Bioinspiration & Biomimetics*, 8(4):046007, 2013.

[12] Q. Cao, A. T. Van Rijn, and I. Poulakakis. On the control of gait transitions in quadrupedal running. In *Proceedings of the IEEE/RSJ International Conference on Intelligent Robots and Systems*, pages 5136–5141, Hamburg, Germany, Sep. 2015.

[13] J. H. Choi and J. W. Grizzle. Feedback control of an underactuated planar bipedal robot with impulsive foot action. *Robotica*, 23:567–580, September 2005.

[14] S. Diller, C. Majidi, and S. H. Collins. A lightweight, low-power electroadhesive clutch and spring for exoskeleton actuation. In *Proceedings of the IEEE International Conference on Robotics and Automation*, pages 682–689, Stockholm, Sweden, May 2016.

[15] Boston Dynamics. Cheetah - fastest legged robot, 2012. [online]. Available at http://bostondynamics.com/robot_cheetah.html.

[16] Boston Dynamics. Ls3 - legged squad support systems, 2013. [online]. Available at http://bostondynamics.com/robot_ls3.html.

[17] G. Elliott, A. Marecki, and H. Herr. Design of a clutch–spring knee exoskeleton for running. *Journal of Medical Devices*, 8(3):031002, 2014.

[18] M. Eslamy, M. Grimmer, and A. Seyfarth. Effects of unidirectional parallel springs on required peak power and energy in powered prosthetic ankles: Comparison between different active actuation concepts. In *Proceedings of the International Conference on Robotics and Biomimetics*, pages 2406–2412, Guangzhou, China, Dec. 2012.

[19] J. Estremera and K.J. Waldron. Thrust control, stabilization and energetics of a quadruped running robots. *The International Journal of Robotics Research*, 27(10):1135, 2008.

[20] G. A. Folkertsma, S. Kim, and S. Stramigioli. Parallel stiffness in a bounding quadruped with flexible spine. In *Proceedings of the IEEE/RSJ International Conference on Intelligent Robots and Systems*, pages 2210–2215, Vilamoura, Algarve, Portugal, Oct. 2012.

[21] Y. Fukuoka, H. Kimura, and A. H. Cohen. Adaptive dynamic walking of a quadruped robot on irregular terrain based on biological concepts. *The International Journal of Robotics Research*, 23(10-11):1059–1073, 2004.

[22] R. Full and D. E. Koditschek. Templates and anchors: Neuromechanical hypotheses of legged locomotion on land. *Journal of Experimental Biology*, 202:3325–3332, 1999.

[23] R. Furnémont, G. Mathijssen, T. Verstraten, D. Lefeber, and B. Vanderborght. Bi-directional series-parallel elastic actuator and overlap of the actuation layers. *Bioinspiration & biomimetics*, 11(1):1–18, 2016.

[24] Z. Gan, T. Wiestner, M. A. Weishaupt, N. M. Waldern, and C. D. Remy. Passive dynamics explain quadrupedal walking, trotting, and tölting. *Journal of Computational and Nonlinear Dynamics*, 11(2):021008, 2016.

[25] C. Gehring, S. Coros, M. Hutter, M. Bloesch, P. Fankhauser, M. A. Hoepflinger, and R. Siegwart. Towards automatic discovery of agile gaits for quadrupedal robots. In *Proceedings of the IEEE International Conference on Robotics and Automation*, pages 4243–4248, Hong Kong, China, May 2014.

[26] C. Gehring, S. Coros, M. Hutter, M. Bloesch, M. A. Hoepflinger, and R. Siegwart. Control of dynamic gaits for a quadrupedal robot. In *Proceedings of the IEEE International Conference on Robotics and Automation*, pages 3287–3292, Karlsruhe, Germany, May 2013.

[27] H. Geyer, A. Seyfarth, and R. Blickhan. Spring-mass running: simple approximate solution and application to gait stability. *Journal of theoretical biology*, 232(3):315–328, 2005.

[28] H. Geyer, A. Seyfarth, and R. Blickhan. Compliant Leg Behaviour Explains Basic Dynamics of Walking and Running. *Proceedings of The Royal Society B*, 273:2861–2867, 2006.

[29] R. M. Ghigliazza, R. Altendorfer, P. Holmes, and D. E. Koditschek. A simply stabilized running model. *SIAM Review*, 47(3):519–549, 2005.

[30] M. Grimmer, M. Eslamy, S. Gliech, and A. Seyfarth. A comparison of parallel- and series elastic elements in an actuator for mimicking human ankle joint in walking and running. In *Proceedings of the IEEE International Conference on Robotics and Automation*, pages 2463–2470, May 2012.

[31] J. W. Grizzle, G. Abba, and F. Plestan. Asymptotically Stable Walking for Biped Robots: Analysis via Systems with Impulse Effects. *IEEE Transactions on Automatic Control*, 46(1):51–64, 2001.

[32] J. W. Grizzle, J. W. Hurst, B. Morris, Hae-Won Park, and K. Sreenath. MABEL, a new robotic bipedal walker and runner. In *Proceedings of the American Control Conference*, pages 2030–2036, St. Louis, Missouri, Jun. 2008.

[33] R. van Ham, T. G. Sugar, B. Vanderborght, K. W. Hollander, and D. Lefeber. Compliant actuator designs. *IEEE Robotics & Automation Magazine*, 16(3):81–94, Sep. 2009.

[34] D.F.B Häufle, M.D. Taylor, S. Schmitt, and H. Geyer. A clutched parallel elastic actuator concept: towards energy efficient powered legs in prosthetics and robotics. In *Proceedings of the IEEE RAS & EMBS International Conference on Biomedical Robotics and Biomechatronics*, pages 1614–1619, Roma, Italy, Jun. 2012.

[35] M. A. Holgate, J. K. Hitt, R. D. Bellman, T. G. Sugar, and K. W. Hollander. The sparky (spring ankle with regenerative kinetics) project: Choosing a dc motor based actuation method. In *Proceedings of the IEEE/RAS-EMBS International Conference on Biomedical Robotics and Biomechatronics*, pages 163–168, Scottsdale, Arizona, Oct. 2008.

[36] C. Hubicki, J. Grimes, M. Jones, D. Renjewski, A. Sprowitz, A. Abate, and J. W. Hurst. Atrias: Design and validation of a tether-free 3d-capable spring-mass bipedal robot. *The International Journal of Robotics Research*, 2016. To appear.

[37] J. W. Hurst. *The Role and Implementation of Compliance in Legged Locomotion*. PhD thesis, Carnegie Mellon Univ., Pittsburgh, PA, 2008.

[38] J. W. Hurst and A. Rizzi. Series Compliance for an Efficient Running Gait. *IEEE Robot. Autom. Mag.*, 15(3):42–51, Sep. 2008.

[39] M. Hutter. *StarlETH & Co-Design and Control of Legged Robots with Compliant Actuation*. PhD thesis, ETH Zurich, Zurich, Switzerland, 2013.

[40] M. Hutter, C. Gehring, M. A. Höpflinger, M. Blösch, and R. Siegwart. Toward combining speed, efficiency, versatility, and robustness in an autonomous quadruped. *IEEE Transactions on Robotics*, 30(6):1427–1440, Dec. 2014.

[41] M. Hutter, C. D. Remy, M. A. Höepflinger, and R. Siegwart. Efficient and versatile locomotion with highly compliant legs. *IEEE/ASME Transactions on Mechatronics*, 18(2):449–458, Apr. 2013.

[42] Sang-Ho Hyon and T. Emura. Symmetric Walking Control: Invariance and Global Stability. In *Proceedings of the IEEE International Conference on Robotics and Automation*, pages 1455–1462, Barcelona, Spain, Apr. 2005.

[43] A. J. Ijspeert. Central pattern generators for locomotion control in animals and robots: a review. *Neural Networks*, 21(4):642–653, 2008.

[44] A. Isidori. *Nonlinear Control Systems*. Berlin: Springer-Verlag, Berlin, third edition, 1995.

[45] K. Kaneko, F. Kanehiro, S. Kajita, H. Hirukawa, T. Kawasaki, M. Hirata, K. Akachi, and T. Isozumi. Humanoid Robot HRP-2. In *Proceedins of the IEEE International Conference on Robotics and Automation*, pages 1083–1090, New Orleans, USA, 2004.

[46] J.G.D Karssen. *Robotic Bipedal Running: Increasing disturbance rejection*. PhD thesis, Delft University of Technology, Delft, Netherlands, 2013.

[47] H. K. Khalil. *Nonlinear Systems - 2nd Edition*. Prentice Hall, Upper Saddle River, 1996.

[48] A. D. Kuo. Choosing your steps carefully: Trade-offs between economy and versatility in dynamic walking bipedal robots. *IEEE Robotics & Automation Magazine*, 14(2):18–29, Jun. 2007.

[49] J.S.W. Lamb and J.A.G. Roberts. Time-reversal Symmetry in Dynamical Systems: A Survey. *Physica D: Nonlinear Phenomena*, 112(1-2):1–39, 1998.

[50] D. Leach, F. Gunther, N. Maheshwari, and F. Iida. Linear multimodal actuation through discrete coupling. *IEEE/ASME Transactions on Mechatronics*, 19(3):827–839, 2014.

[51] Z. Li, N. G. Tsagarakis, and D. G. Caldwel. A passivity based admittance control for stabilizing the compliant humanoid COMAN. In *Proceedings of the IEEE-RAS International Conference on Humanoid Robots*, pages 43–49, Osaka, Japan, Nov. 2012.

[52] X. Liu and I. Poulakakis. On the energetics of a switchable parallel elastic actuator design for monopedal running. In *Proceedings of the IEEE International Conference on Robotics and Biomimetics*, pages 769–774, Zhuhai, China, Dec. 2015.

[53] X. Liu and I. Poulakakis. On the stability of symmetric quadrupedal bounding gaits via factored poincare maps. In *Proceedings of the American Control Conference*, pages 3898–3903, Boston, USA, Jul. 2016.

[54] X. Liu, A. Rossi, and I. Poulakakis. Spear: A monopedal robot with switchable parallel elastic actuator. In *Proceedings of the IEEE/RSJ International Conference on Intelligent Robots and Systems*, pages 5142 – 5147, Hamburg, Germany, Sep. 2015.

[55] X. Liu, C. Semini, and I. Poulakakis. Active compliance hybrid zero dynamics control of bounding on hyq. In *Proceedings of the IEEE International Conference on Robotics and Biomimetics*, pages 1047–1052, Zhuhai, China, Dec. 2015.

[56] D.W. Marhefka, D.E. Orin, J.P. Schmiedeler, and K.J. Waldron. Intelligent control of quadrupedal gallops. *IEEE/ASME Transactions on Mechatronics*, 8(4):446–456, 2003.

[57] G. Mathijssen, D. Lefeber, and B. Vanderborght. Variable recruitment of parallel elastic elements: Series–parallel elastic actuators (spea) with dephased mutilated gears. *IEEE/ASME Transactions on Mechatronics*, 20(2):594–602, Apr. 2015.

[58] Horst-Moritz Maus, S. Lipfert, M. Gross, J. Rummel, and A. Seyfarth. Upright human gait did not provide a major mechanical challenge for our ancestors. *Nature Communications*, 1(70), 2010.

[59] Horst-Moritz Maus, J. Rummel, and A. Seyfarth. Stable upright walking and running using a simple pendulum based control scheme. In *Proceedings of the International Conference on Climbing and Walking Robots*, pages 623–629, Coimbra, Portugal, Sep. 2008.

[60] T. A. McMahon and G. C. Cheng. The mechanics of running: How does stiffness couple with speed? *Journal of Biomechanics*, 23:65–78, 1990.

[61] U. Mettin, P. X. La Hera, L. B. Freidovich, and A. S. Shiriaev. Parallel elastic actuators as control tool for preplanned trajectories of underactuated mechanical systems. *The International Journal of Robotics Research*, 29(9):1186–1198, 2009.

[62] J.G. Nichol, S.P.N. Singh, K.J. Waldron, L.R. Palmer, and D.E. Orin. System Design of a Quadrupedal Galloping Machines. *The International Journal of Robotics Research*, 23(10-11):1013, 2004.

[63] N. Paine, S. Oh, and L. Sentis. Design and control considerations for high-performance series elastic actuators. *IEEE/ASME Transactions on Mechatronics*, 19(3):1080–1091, 2014.

[64] Hae-Won Park and S. Kim. Quadrupedal galloping control for a wide range of speed via vertical impulse scaling. *Bioinspiration & Biomimetics*, 10(2):025003, 2015.

[65] Hae-Won Park, S. Park, and S. Kim. Variable-speed quadrupedal bounding using impulse planning: Untethered high-speed 3d running of mit cheetah 2. In *Proceedings of the IEEE International Conference on Robotics and Automation*, pages 5163–5170, Seattle, Washington, May 2015.

[66] M. Plooij, G. Mathijssen, P. Cherelle, D. Lefeber, and B. Vanderborght. Lock your robot: A review of locking devices in robotics. *IEEE Robotics & Automation Magazine*, 22(1):106–117, 2015.

[67] M. Plooij, M. van Nunspeet, M. Wisse, and H. Vallery. Design and evaluation of the bi-directional clutched parallel elastic actuator (bic-pea). In *Proceedings of the IEEE International Conference on Robotics and Automation*, pages 1002–1009, Seattle, Washington, May 2015.

[68] C. M. Pollock and R. E. Shadwick. Relationship between body mass and biomechanical properties of limb tendons in adult mammals. *American Journal of Physiology-Regulatory, Integrative and Comparative Physiology*, 266(3):R1016–R1021, 1994.

[69] I. Poulakakis and J. W. Grizzle. Modeling and control of the monopedal robot Thumper. In *Proceedings of the IEEE International Conference on Robotics and Automation*, pages 3327–3334, Kobe, Japan, May 2009.

[70] I. Poulakakis and J. W. Grizzle. The spring loaded inverted pendulum as the hybrid zero dynamics of an asymmetric hopper. *IEEE Transactions on Automatic Control*, 54(8):1779–1793, 2009.

[71] I. Poulakakis, E. G. Papadopoulos, and M. Buehler. On the stability of the passive dynamics of quadrupedal running with a bounding gait. *The International Journal of Robotics Research*, 25(7):669–687, 2006.

[72] I. Poulakakis, J. A. Smith, and M. Buehler. Modeling and experiments of untethered quadrupedal running with a bounding gait: The scout ii robot. *The International Journal of Robotics Research*, 24(4):239–256, 2005.

[73] G. A. Pratt and M.M. Williamson. Series elastic actuators. In *Proceedings of the IEEE/RSJ International Conference on Intelligent Robots and Systems*, pages 399–406, Aug. 1995.

[74] M. H. Raibert. *Legged Robots that Balance*. MIT Press, Cambridge, MA, 1986.

[75] M. H. Raibert. Running with symmetry. *The International Journal of Robotics Research*, 5(4):3–19, 1986.

[76] M. H. Raibert. Symmetry in running. *Science*, 231(4743):1292–1294, 1986.

[77] M. H. Raibert, K. Blankespoor, G. Nelson, R. Playter, and the BigDog Team. BigDog, the Rough-Terrain Quadruped Robot. In *Proceedings of the 17th World Congress*, pages 10822–10825, Seoul, Korea, Jul. 2008.

[78] A. Ramezani, J. W. Hurst, K. A. Hamed, and J. W. Grizzle. Performance analysis and feedback control of atrias, a three-dimensional bipedal robot. *Journal of Dynamic Systems, Measurement, and Control*, 136(2):021012, 2014.

[79] H. Razavi, A. M. Bloch, C. Chevallereau, and J. W. Grizzle. Symmetry in legged locomotion: a new method for designing stable periodic gaits. *Autonomous Robots*, 2016. To appear.

[80] H. Razavi, X. Da, and A. M. Bloch. Symmetric virtual constraints for periodic walking of legged robots. In *Proceedings of the IEEE Conference on Decision and Control*, 2016. To appear.

[81] J. Reher, E. A. Cousineau, A. Hereid, C. M. Hubicki, and A. D. Ames. Realizing dynamic and efficient bipedal locomotion on the humanoid robot DURUS. In *Proceedings of the IEEE International Conference on Robotics and Automation*, pages 1794–1801, StockholmStockholm, Sweden, May 2016.

[82] T. J. Roberts and E. Azizi. Flexible mechanisms: the diverse roles of biological springs in vertebrate movement. *Journal of Experimental Biology*, 214(3):353–361, 2011.

[83] E. J. Rouse, L. M. Mooney, and H. M. Herr. Clutchable series-elastic actuator: Implications for prosthetic knee design. *The International Journal of Robotics Research*, 33(13):1611–1625, 2014.

[84] J. Rummel and A. Seyfarth. Stable running with segmented legs. *The International Journal of Robotics Research*, 27(8):919–934, 2008.

[85] Y. Sakagami, R. Watanabe, C. Aoyama, S. Matsunaga, N. Higaki, and K. Fujimura. The intelligent asimo: system overview and integration. In *Proceeding of the IEEE/RSJ International Conference on Intelligent Robots and Systems*, volume 3, pages 2478–2483, Lausanne, Switzerland, Oct. 2002.

[86] J. Schmitt. Simple feedback control of cockroach running. In *Fast Motions in Biomechanics and Robotics*, pages 361–381. Springer Berlin Heidelberg, 2006.

[87] W. J. Schwind. *Spring Loaded Inverted Pendulum Running: A Plant Model*. PhD thesis, The University of Michigan, 1998.

[88] W. J. Schwind and D. E. Koditschek. Approximating the stance map of a 2-DOF monoped runner. *Journal of Nonlinear Science*, 10:533–568, 2000.

[89] C. Semini, V. Barasuol, T. Boaventura, M. Frigerio, M. Focchi, D. G. Caldwell, and J. Buchli. Towards versatile legged robots through active impedance control. *The International Journal of Robotics Research*, 34(7):1003–1020, 2015.

[90] C. Semini, N. G. Tsagarakis, E. Guglielmino, M. Focchi, F. Cannella, and D. G. Caldwell. Design of HyQ - a hydraulically and electrically actuated quadruped robot. *Proceedings of the IMechE Part I: Journal Systems and Control Engineering*, 225(6):831–849, 2011.

[91] S. Seok, A. Wang, M. Y. Chuah, D. Otten, J. Lang, and S. Kim. Design principles for highly efficient quadrupeds and implementation on the MIT cheetah robot. In *Proceedings of the IEEE International Conference on Robotics and Automation*, pages 3307–3312, Karlsruhe, Germany, May 2013.

[92] S. Seok, A. Wang, M. Y. Michael Chuah, D. J. Hyun, J. Lee, D. M. Otten, J. H. Lang, and S. Kim. Design principles for energy-efficient legged locomotion and implementation on the MIT cheetah robot. *IEEE/ASME Transactions on Mechatronics*, 20(3):1117–1129, Jun. 2015.

[93] S. Seok, A. Wang, D. Otten, and S. Kim. Actuator design for high force proprioceptive control in fast legged locomotion. In *Proceedings of the IEEE/RSJ International Conference on Intelligent Robots and Systems*, pages 1970–1975, Vilamoura, Algarve, Portugal, Oct. 2012.

[94] A. Seyfarth, H. Geyer, M. Gunther, and R. Blickhan. A movement criterion for running. *Journal of Biomechanics*, 35(5):649–55, 2002.

[95] A. Seyfarth, H. Geyer, and H. Herr. Swing leg retraction: A simple control model for stable running. *Journal of Experimental Biology*, 206:2547–2555, 2003.

[96] A. Sprowitz, A. Tuleu, M. Vespignani, M. Ajallooeian, E. Badri, and A. J. Ijspeert. Towards dynamic trot gait locomotion: Design, control, and experiments with cheetah-cub, a compliant quadruped robot. *The International Journal of Robotics Research*, 2013.

[97] K. Sreenath. *Feedback control of a bipedal walker and runner with compliance*. PhD thesis, The University of Michigan, 2011.

[98] K. Sreenath, Hae-Won Park, I. Poulakakis, and J. Grizzle. A compliant hybrid zero dynamics controller for stable, efficient and fast bipedal walking on MABEL. *The International Journal of Robotics Research*, 30(9):1170–1193, 2011.

[99] K. Sreenath, Hae-Won Park, I. Poulakakis, and J. Grizzle. Embedding active force control within the compliant hybrid zero dynamics to achieve stable, fast running on MABEL. *The International Journal of Robotics Research*, 32(3):324–345, 2013.

[100] A. K. Valenzuela and S. Kim. Optimally scaled hip-force planning: A control approach for quadrupedal running. In *Proceedings of the IEEE International Conference on Robotics and Automation*, pages 1901–1907, Saint Paul, Minnesota, May 2012.

[101] M. Vukobratovic and B. Borovac. Zero moment point – thirty-five years of its life. *International Journal of Humanoid Robotics*, 1(1):157–173, 2004.

[102] E. R. Westervelt, J. W. Grizzle, C. Chevallereau, J. H. Choi, and B. Morris. *Feedback Control of Dynamic Bipedal Robot Locomotion*. Taylor & Francis/CRC Press, 2007.

[103] T. Yang, E. R. Westervelt, J. P. Schmiedeler, and R. A. Bockbrader. Design and control of a planar bipedal robot ERNIE with parallel knee compliance. *Autonomous Robots*, 25(4):317–330, Nov. 2008.

[104] Y. Yesilevskiy, Z. Gan, and C.D. Remy. Optimal configuration of series and parallel elasticity in a 2D monoped. In *Proceedings of the IEEE International Conference on Robotics and Automation*, pages 1360–1365, Stockholm, Sweden, May 2016.

[105] Y. Yesilevskiy, W. Xi, and C.D. Remy. A comparison of series and parallel elasticity in a monoped hopper. In *Proceedings of the IEEE International Conference on Robotics and Automation*, pages 1036 – 1041, Seattle, Washington, May 2015.

Appendix A

INTERMEDIATE PROOF OF BOUNDING CONTROLLER

A.1 Time-to-Switch of Flight Phase

For the flight phase that follows the posterior stance phase, the corresponding flow can be obtain by integrating the flow as

$$\phi_{\mathrm{f}}(t, x_0) = \begin{pmatrix} x_{\mathrm{cm},0} + \dot{x}_{\mathrm{cm},0} t \\ y_{\mathrm{cm},0} + \dot{y}_{\mathrm{cm},0} t - \dfrac{gt^2}{2} \\ \theta_0 + \dot{\theta}_0 t \\ \dot{x}_{\mathrm{cm},0} \\ \dot{y}_{\mathrm{cm},0} - gt \\ \dot{\theta}_0 \end{pmatrix}, \tag{A.1}$$

where $x_0 = [x_{\mathrm{cm},0}, y_{\mathrm{cm},0}, \theta_0, \dot{x}_{\mathrm{cm},0}, \dot{y}_{\mathrm{cm},0}, \dot{\theta}_0]$ is the initial state of the flight phase. The flow map F_{f} (without the x_{cm} part) can defined as following:

$$F_{\mathrm{f}} = \phi_{\mathrm{f}}^{t_{\mathrm{f}}(z_0)}(z_0), \tag{A.2}$$

where $z_0 = [y_{\mathrm{cm},0}, \theta_0, \dot{x}_{\mathrm{cm},0}, \dot{y}_{\mathrm{cm},0}, \dot{\theta}_0]$. $t_{\mathrm{f}}(z_0)$ is the time-to-switch function which gives the duration the system evolves in this vector field. $t_{\mathrm{f}}(z_0)$ is defined as following

$$t_{\mathrm{f}}(z_0) = \inf\{t > 0 | H_{\mathrm{f}\to\mathrm{sa}}(\phi_{\mathrm{f}}^{t}(z_0), \gamma_{\mathrm{a}}(z_0)) = 0\}, \tag{A.3}$$

where $H_{\mathrm{f}\to\mathrm{sa}}$ is the height of the anterior toe:

$$H_{\mathrm{f}\to\mathrm{sa}} = y_{\mathrm{cm},0} + \dot{y}_{\mathrm{cm},0} t - \frac{gt^2}{2} + L\sin(\theta_0 + \dot{\theta}_0 t) - l_0 \cos\gamma_{\mathrm{a}}(z_0) \ . \tag{A.4}$$

and $\gamma_{\mathrm{a}}(z_0)$ is the anterior leg angle given by a state-based leg control policy.

Remark 3. *Notice that $t_{\mathrm{f}} = t_{\mathrm{f}}(z_0)$ is an implicit function of initial state z_0 defined by $H_{\mathrm{f}\to\mathrm{sa}} = 0$. This fact will be used during the following proof. Also notice that $H_{\mathrm{f}\to\mathrm{sa}}$ is only zero at the initial liftoff and final touchdown event.*

A.2 Determinant of the Jacobian of F_{f}

The Jacobian of the flow map $F_{\mathrm{f}}(z_0)$ (restriction on z without the x_{cm} component) is

$$D_{z_0}F_{\mathrm{f}} =$$

$$\left(\begin{array}{c|c|c|c|c}
1 + \frac{\dot{y}_{\mathrm{cm},0}\cdot\partial t_{\mathrm{f}}}{\partial y_{\mathrm{cm},0}} - \frac{g t_{\mathrm{f}}\cdot\partial t_{\mathrm{f}}}{\partial y_{\mathrm{cm},0}} & \frac{\dot{y}_{\mathrm{cm},0}\cdot\partial t_{\mathrm{f}}}{\partial \theta_0} - \frac{g t_{\mathrm{f}}\cdot\partial t_{\mathrm{f}}}{\partial \theta_0} & * & t_{\mathrm{f}} + \frac{\dot{y}_{\mathrm{cm},0}\cdot\partial t_{\mathrm{f}}}{\partial \dot{y}_{\mathrm{cm},0}} - \frac{g t_{\mathrm{f}}\cdot\partial t_{\mathrm{f}}}{\partial \dot{y}_{\mathrm{cm},0}} & * \\
\dot{\theta}_0 \frac{\partial t_{\mathrm{f}}}{\partial y_{\mathrm{cm},0}} & 1 + \dot{\theta}_0 \frac{\partial t_{\mathrm{f}}}{\partial \theta_0} & * & \dot{\theta}_0 \frac{\partial t_{\mathrm{f}}}{\partial \dot{y}_{\mathrm{cm},0}} & * \\
0 & 0 & \boxed{1} & 0 & 0 \\
-g \frac{\partial t_{\mathrm{f}}}{\partial y_{\mathrm{cm},0}} & -g \frac{\partial t_{\mathrm{f}}}{\partial \theta_0} & * & 1 - g \frac{\partial t_{\mathrm{f}}}{\partial \dot{y}_{\mathrm{cm},0}} & * \\
0 & 0 & 0 & 0 & \boxed{1}
\end{array}\right). \tag{A.5}$$

The determinant of the Jacobian is

$$det(D_{z_0}F_{\mathrm{f}}) = 1 - g\frac{\partial t_{\mathrm{f}}}{\partial \dot{y}_{\mathrm{cm},0}} + \dot{y}_{\mathrm{cm},0}\frac{\partial t_{\mathrm{f}}}{\partial y_{\mathrm{cm},0}} + \dot{\theta}_0\frac{\partial t_{\mathrm{f}}}{\partial \theta_0}. \tag{A.6}$$

Noticing that t_{f} is an **implicit function of initial state** and satisfy the following equation,i.e., the threshold function (A.4) equals to zero:

$$H_{\mathrm{f}\to\mathrm{sa}} = y_{\mathrm{cm},0} + \dot{y}_{\mathrm{cm},0}t_{\mathrm{f}} - \frac{g t_{\mathrm{f}}^2}{2} + L\sin(\theta_0 + \dot{\theta}_0 t_{\mathrm{f}}) - l_0\cos\gamma_{\mathrm{a}}^{td}(z_0) = 0, \tag{A.7}$$

where $\gamma_{\mathrm{a}}^{TD} = \gamma_{\mathrm{a}}(z_0)|_{t=t_{\mathrm{f}}}$ is the leg angle at the instance of touchdown angle.

Took partial derivative of (A.7) with respect to $y_{\mathrm{cm},0}$ we get the following:

$$\frac{\partial H}{\partial y_{\mathrm{cm},0}} + \frac{\partial H}{\partial t_{\mathrm{f}}}\frac{\partial t_{\mathrm{f}}}{\partial y_{\mathrm{cm},0}} = 0, \tag{A.8}$$

where

$$\frac{\partial H}{\partial y_{\mathrm{cm},0}} = 1 + l_0\sin\gamma_{\mathrm{a}}^{td}\frac{\partial \gamma_{\mathrm{a}}^{td}}{\partial y_{\mathrm{cm},0}}, \tag{A.9}$$

$$\frac{\partial H}{\partial t_{\mathrm{f}}} := \Delta_2 = \dot{y}_{\mathrm{cm},0} - g t_{\mathrm{f}} + \dot{\theta}_0 L\cos(\theta_0 + \dot{\theta}_0 t_{\mathrm{f}}). \tag{A.10}$$

Hence

$$\frac{\partial t_{\mathrm{f}}}{\partial y_{\mathrm{cm},0}} = \frac{1 + l_0 \sin \gamma_{\mathrm{a}}^{td} \frac{\partial \gamma_{\mathrm{a}}^{td}}{\partial y_{\mathrm{cm},0}}}{-\Delta_2}. \tag{A.11}$$

Similarly, we get the following:

$$\frac{\partial t_{\mathrm{f}}}{\partial \theta_0} = \frac{L \cos(\theta_0 + \dot{\theta}_0 t_{\mathrm{f}}) + l_0 \sin \gamma_{\mathrm{a}}^{td} \frac{\partial \gamma_{\mathrm{a}}^{td}}{\partial \theta_0}}{-\Delta_2}, \tag{A.12}$$

$$\frac{\partial t_{\mathrm{f}}}{\partial \dot{y}_{\mathrm{cm},0}} = \frac{t_{\mathrm{f}} + l_0 \sin \gamma_{\mathrm{a}}^{td} \frac{\partial \gamma_{\mathrm{a}}^{td}}{\partial \dot{y}_{\mathrm{cm},0}}}{-\Delta_2}, \tag{A.13}$$

Plug in these three partial derivatives to the expression (A.6), we get the following:

$$\boxed{det(D_{z_0} F_{\mathrm{f}}) = \frac{\Delta_1}{-\Delta_2}} \ , \tag{A.14}$$

where

$$\Delta_1 = \sin \gamma_{\mathrm{a}} l_0 (\dot{y}_{\mathrm{cm},0} \frac{\partial \gamma_{\mathrm{a}}^{td}}{\partial y_{\mathrm{cm},0}} + \dot{\theta}_0 \frac{\partial \gamma_{\mathrm{a}}^{td}}{\partial \theta_0} - g \frac{\partial \gamma_{\mathrm{a}}^{td}}{\partial \dot{y}_{\mathrm{cm},0}}) \ . \tag{A.15}$$

A.3 Determinant of the Proposed Control Strategy

In the control strategy (3.78), the leg angle is kept constant during the flight phase, and it is a function of initial state of the flight phase only:

$$\gamma_{\mathrm{a}}^{td}[n] = \gamma_{\mathrm{a}}[n] = \bar{\gamma}_{\mathrm{a}}^{td} + c(\bar{\gamma}_{\mathrm{p}}^{lo} - \gamma_{\mathrm{p}}^{lo}[n]) = \bar{\gamma}_{\mathrm{a}}^{td} + c(\bar{\gamma}_{\mathrm{p}}^{lo} + \mathrm{acos}(\frac{y_{\mathrm{cm},0} - L \sin \theta_0}{l_0})) \ , \tag{A.16}$$

where $\bar{\gamma}_{\mathrm{a}}^{td}$ and $\bar{\gamma}_{\mathrm{p}}^{lo}$ are constant (nominal value of the fixed point), and the last equation is obtained by noticing that the posterior leg liftoff at the same instance of the beginning of the flight phase. As a result,

$$\Delta_2 = \dot{y}_{\mathrm{cm},0} - g t_{\mathrm{f}} + \dot{\theta}_0 L \cos(\theta_0 + \dot{\theta}_0 t_{\mathrm{f}}) \ . \tag{A.17}$$

Notice that the touchdown angle is not a function of $\dot{y}_{\mathrm{cm},0}$, so

$$\Delta_1 = \sin \gamma_{\mathrm{a}} l_0 (\dot{y}_{\mathrm{cm},0} \frac{\partial \gamma_{\mathrm{a}}^{td}}{\partial y_{\mathrm{cm},0}} + \dot{\theta}_0 \frac{\partial \gamma_{\mathrm{a}}^{td}}{\partial \theta_0}) \ . \tag{A.18}$$

So now the determinate of a flight phase is

$$det(D_{z_0}F_{\mathrm{f}}) = \frac{\Delta_1}{-\Delta_2} = -\frac{\sin\gamma_{\mathrm{a}} l_0(\dot{y}_{\mathrm{cm},0}\frac{\partial\gamma_{\mathrm{a}}^{td}}{\partial y_{\mathrm{cm},0}} + \dot{\theta}_0\frac{\partial\gamma_{\mathrm{a}}^{td}}{\partial\theta_0})}{\dot{y}_{\mathrm{cm},0} - gt_{\mathrm{f}} + \dot{\theta}_0 L\cos(\theta_0 + \dot{\theta}_0 t_{\mathrm{f}})} \quad . \tag{A.19}$$

Using the expression of γ_{a}^{td}, we obtain

$$\frac{\partial\gamma_{\mathrm{a}}^{td}}{\partial\theta_0} = c\frac{(-1)(-L\cos\theta_0)}{l_0\sqrt{1-(\frac{y_{\mathrm{cm},0}-L\sin\theta_0}{l_0})^2}} \quad . \tag{A.20}$$

Since at the instance of liftoff the following holds:

$$(\frac{y_{\mathrm{cm},0} - L\sin\theta_0}{l_0}) = \cos\gamma_{\mathrm{p}}^{lo} \quad . \tag{A.21}$$

Hence

$$\frac{\partial\gamma_{\mathrm{a}}^{td}}{\partial\theta_0} = c\frac{(L\cos\theta_0)}{l_0|\sin\gamma_{\mathrm{p}}^{lo}|} \quad . \tag{A.22}$$

Using the same process, we can obtain the $\frac{\partial\gamma_{\mathrm{a}}^{td}}{\partial y_{\mathrm{cm},0}}$ as following:

$$\frac{\partial\gamma_{\mathrm{a}}^{td}}{\partial y_{\mathrm{cm},0}} = \frac{-c}{l_0|\sin\gamma_{\mathrm{p}}^{lo}|} \quad . \tag{A.23}$$

Hence, by plugging these two equations into (A.19), we obtain

$$det(D_{z_0}F_{\mathrm{f}}) = \frac{c\frac{\sin\gamma_{\mathrm{a}}^{td}}{|\sin\gamma_{\mathrm{p}}^{lo}|}(-\dot{y}_{\mathrm{cm},0} + L\dot{\theta}_0\cos\theta_0)}{\dot{y}_{\mathrm{cm},0} - gt_{\mathrm{f}} + \dot{\theta}_0 L\cos(\theta_0 + \dot{\theta}_0 t_{\mathrm{f}})} \quad . \tag{A.24}$$

Notice that until now, **we do not require that the initial state is a fixed point**. All we assume is that z_0 is the state at the event of posterior leg liftoff, which is also the beginning of a flight phase. Now, the determinate is evaluated at the fixed point $\bar{z}_0$. Notice that at fixed point,

$$\bar{\dot{y}}_{\mathrm{cm},0} - gt_{\mathrm{f}} = -\bar{\dot{y}}_{\mathrm{cm},0} \quad , \tag{A.25}$$

which means that for a fixed point, the vertical velocity at the end of the flight phase has the same magnitude with the initial value, only the sign is changed.

$$\bar{\theta}_0 + \bar{\dot{\theta}}_0 t_{\mathrm{f}} = -\bar{\theta}_0 \quad , \tag{A.26}$$

which means that for a fixed point, the pitch angle at the end of the flight phase has the same magnitude with the initial value, only the sign is changed. What is more, at the fixed point, we have the touchdown angle of anterior leg equals the negative of the liftoff angle of the posterior leg, i.e., $\bar{\gamma}_{\mathrm{a}}^{td} = -\bar{\gamma}_{\mathrm{p}}^{lo}$.

As a result,

$$|det(D_{z_0}F_{\mathrm{f}})|_{z_0=\bar{z}_0}| = |\frac{c\frac{\sin\bar{\gamma}_{\mathrm{a}}^{td}}{|\sin\bar{\gamma}_{\mathrm{p}}^{lo}|}(-\bar{\dot{y}}_{\mathrm{cm},0} + L\bar{\dot{\theta}}_0\cos\bar{\theta}_0)}{\bar{\dot{y}}_{\mathrm{cm},0} - gt_{\mathrm{f}} + \bar{\dot{\theta}}_0 L\cos(\bar{\theta}_0 + \bar{\dot{\theta}}_0 t_{\mathrm{f}})}| = |c| \ . \tag{A.27}$$

Appendix B

HOLONOMIC CONSTRAINTS

This appendix provides more details on the design of the polynomials that characterize the desired evolution of the controlled variables. To simplify the presentation, we focus on a single controlled variable θ with desired evolution h_θ^{d}.

B.1 Polynomial Design

We consider the output

$$y = \theta - h_\theta^{\mathrm{d}}(s(q), \alpha), \tag{B.1}$$

where s is a monotonic function of configuration q, defined though $s(q) = \frac{\phi(q)-\phi_0}{\Delta}$ with ϕ_0 and Δ suitably selected constants that have the meaning of the constants participating in (4.13) for the stance and in (4.23) for the flight phases. For example, in the stance-posterior phase, ϕ is γ_{p}, ϕ_0 is $\gamma_{\mathrm{p}}^{\mathrm{td}}$ and Δ corresponds to Δ_{sp}. Then, h_θ^{d} is selected as

$$h_\theta^{\mathrm{d}}(s(q)) := \begin{cases} \sum_{k=0}^{4} a_k s(q)^k, & \text{if } s < \sigma \\ a_5, & \text{if } s \geq \sigma. \end{cases} \tag{B.2}$$

The first part of (B.2) transfers the corresponding controlled variable θ over the interval $[0, \sigma)$ to its target position with zero final velocity and acceleration. The second part of (B.2) keeps the controlled variable equal to constant a_5 until the phase terminates. Lastly, to ensure continuity up to the second derivative, we impose the following constraints

$$\begin{aligned} a_4\sigma^4 + \ a_3\sigma^3 + \ a_2\sigma^2 + \ a_1\sigma + \ a_0 &= a_5 \\ 4a_4\sigma^3 + 3a_3\sigma^2 + 2a_2\sigma + \ a_1 &= 0 \\ 12a_4\sigma^2 + 6a_3\sigma + 2a_2 &= 0. \end{aligned} \tag{B.3}$$

For each output (two for the stance phase and four for the flight phases), this procedures introduces a number of parameters – namely, $\{a_0, ..., a_5, \sigma, \Delta, \phi_0\}$ – which participate in the definition of α in (B.1).

B.2 Coefficient Updates for Invariance

To extend invariance in the hybrid setting we need to ensure that the initial condition x_i^+ for each phase belongs on the corresponding zero dynamics surface $\mathcal{Z}_{\alpha_i}$. To satisfy this condition, the surface $\mathcal{Z}_{\alpha_i}$ can be "deformed" by updating α_i so that $x_i^+ \in \mathcal{Z}_{\alpha_i}$. Consider again the controlled variable θ, and let θ^+ be its initial value. Then, updating the coefficients in (B.2) through

$$a_0 = \theta^+ \quad \text{and} \quad a_1 = (1/\dot{s})\dot{\theta}^+, \tag{B.4}$$

for all the controlled variables ensures invariance under transitions. Note that (B.3) and (B.4) define a system of five equations with five unknowns, the solution of which provides the polynomial coefficients.

Appendix C

COPYRIGHT PERMISSIONS

This thesis includes materials reused from papers including [52], [53], [54] and [55]. The reuse permissions from IEEE are attached in the following pages.

Title:	On the energetics of a switchable parallel elastic actuator design for monopedal running
Conference Proceedings:	Robotics and Biomimetics (ROBIO), 2015 IEEE International Conference on
Author:	Xin Liu
Publisher:	IEEE
Date:	Dec. 2015

Title:	On the stability of symmetric quadrupedal bounding gaits via factored Poincaré maps
Conference Proceedings:	American Control Conference (ACC), 2016
Author:	Xin Liu
Publisher:	IEEE
Date:	July 2016

Thesis / Dissertation Reuse

The IEEE does not require individuals working on a thesis to obtain a formal reuse license, however, you may print out this statement to be used as a permission grant:

Requirements to be followed when using any portion (e.g., figure, graph, table, or textual material) of an IEEE copyrighted paper in a thesis:

1) In the case of textual material (e.g., using short quotes or referring to the work within these papers) users must give full credit to the original source (author, paper, publication) followed by the IEEE copyright line © 2011 IEEE.
2) In the case of illustrations or tabular material, we require that the copyright line © [Year of original publication] IEEE appear prominently with each reprinted figure and/or table.
3) If a substantial portion of the original paper is to be used, and if you are not the senior author, also obtain the senior author's approval.

Requirements to be followed when using an entire IEEE copyrighted paper in a thesis:

1) The following IEEE copyright/ credit notice should be placed prominently in the references: © [year of original publication] IEEE. Reprinted, with permission, from [author names, paper title, IEEE publication title, and month/year of publication]
2) Only the accepted version of an IEEE copyrighted paper can be used when posting the paper or your thesis on line.
3) In placing the thesis on the author's university website, please display the following message in a prominent place on the website: In reference to IEEE copyrighted material which is used with permission in this thesis, the IEEE does not endorse any of [university/educational entity's name goes here]'s products or services. Internal or personal use of this material is permitted. If interested in reprinting/republishing IEEE copyrighted material for advertising or promotional purposes or for creating new collective works for resale or redistribution, please go to http://www.ieee.org/publications_standards/publications/rights/rights_link.html to learn how to obtain a License from RightsLink.

If applicable, University Microfilms and/or ProQuest Library, or the Archives of Canada may supply single copies of the dissertation.

Title:	SPEAR: A monopedal robot with Switchable Parallel Elastic actuation
Conference Proceedings:	Intelligent Robots and Systems (IROS), 2015 IEEE/RSJ International Conference on
Author:	Xin Liu
Publisher:	IEEE
Date:	September 2015

Thesis / Dissertation Reuse

The IEEE does not require individuals working on a thesis to obtain a formal reuse license, however, you may print out this statement to be used as a permission grant:

Requirements to be followed when using any portion (e.g., figure, graph, table, or textual material) of an IEEE copyrighted paper in a thesis:

1) In the case of textual material (e.g., using short quotes or referring to the work within these papers) users must give full credit to the original source (author, paper, publication) followed by the IEEE copyright line © 2011 IEEE.
2) In the case of illustrations or tabular material, we require that the copyright line © [Year of original publication] IEEE appear prominently with each reprinted figure and/or table.
3) If a substantial portion of the original paper is to be used, and if you are not the senior author, also obtain the senior author's approval.

Requirements to be followed when using an entire IEEE copyrighted paper in a thesis:

1) The following IEEE copyright/ credit notice should be placed prominently in the references: © [year of original publication] IEEE. Reprinted, with permission, from [author names, paper title, IEEE publication title, and month/year of publication]
2) Only the accepted version of an IEEE copyrighted paper can be used when posting the paper or your thesis on line.
3) In placing the thesis on the author's university website, please display the following message in a prominent place on the website: In reference to IEEE copyrighted material which is used with permission in this thesis, the IEEE does not endorse any of [university/educational entity's name goes here]'s products or services. Internal or personal use of this material is permitted. If interested in reprinting/republishing IEEE copyrighted material for advertising or promotional purposes or for creating new collective works for resale or redistribution, please go to http://www.ieee.org/publications_standards/publications/rights/rights_link.html to learn how to obtain a License from RightsLink.

If applicable, University Microfilms and/or ProQuest Library, or the Archives of Canada may supply single copies of the dissertation.

Title:	Active compliance hybrid zero dynamics control of bounding on HyQ
Conference Proceedings:	Robotics and Biomimetics (ROBIO), 2015 IEEE International Conference on
Author:	Xin Liu
Publisher:	IEEE
Date:	Dec. 2015